ANALYSIS OF SPHERICAL-RECTANGULAR PRINTED ANTENNAS AND ANTENNA ARRAYS USING CAVITY MODEL

A THESIS SUBMITTED TO
THE GRADUATE SCHOOL OF NATURAL AND APPLIED SCIENCES
OF
MIDDLE EAST TECHNICAL UNIVERSITY

BY

OĞUZ DEMİR

IN PARTIAL FULFILLMENT OF THE REQUIREMENTS
FOR
THE DEGREE OF MASTER OF SCIENCE
IN
ELECTRICAL AND ELECTRONICS ENGINEERING

FEBRUARY 2017

Approval of the thesis:

ANALYSIS OF SPHERICAL-RECTANGULAR PRINTED ANTENNAS AND ANTENNA ARRAYS USING CAVITY MODEL

submitted by **OĞUZ DEMİR** in partial fulfillment of the requirements for the degree of **Master of Science in Electrical and Electronics Engineering Department, Middle East Technical University** by,

Prof. Dr. Gülbin Dural _____
Dean, Graduate School of **Natural and Applied Sciences**

Prof. Dr. Tolga Çiloğlu _____
Head of Department, **Electrical and Electronics Engineering**

Prof. Dr. Gülbin Dural _____
Supervisor, **Electrical and Electronics Eng. Dept., METU**

Examining Committee Members:

Prof. Dr. Mustafa Kuzuoğlu _____
Electrical and Electronics Eng. Dept., METU

Prof. Dr. Gülbin Dural _____
Electrical and Electronics Eng. Dept., METU

Prof. Dr. Özlem Aydın Çivi _____
Electrical and Electronics Eng. Dept., METU

Assoc. Prof. Dr. Lale Alatan _____
Electrical and Electronics Eng. Dept., METU

Prof. Dr. Birsen Saka _____
Electrical and Electronics Eng. Dept., Hacettepe University

Date: 02.02.2017

I hereby declare that all information in this document has been obtained and presented in accordance with academic rules and ethical conduct. I also declare that, as required by these rules and conduct, I have fully cited and referenced all material and results that are not original to this work.

Name, Last name: OĞUZ DEMİR

Signature :

ABSTRACT

ANALYSIS OF SPHERICAL-RECTANGULAR PRINTED ANTENNAS AND ANTENNA ARRAYS USING CAVITY MODEL

Demir, Oğuz

M.S., Department of Electrical and Electronics Engineering

Supervisor : Prof. Dr. Gülbin Dural

February 2017, 108 pages

Printed antennas are commonly used since these antennas are preferred in many applications due to their advantageous properties. In order to employ these antennas in such applications, a thorough investigation and analysis are generally required. Although this can be implemented with fully numerical methods for the sake of high accuracy, the complex calculations required in the process lead to heavy computational load, hence generally demands high quality simulation software. In this thesis, the spherical-rectangular antennas mounted on a conducting sphere are analyzed by employing the cavity model as the basic analysis method, and the equivalent magnetic currents are derived. The radiation of equivalent currents in the presence of the conducting sphere is modeled by means of spherical wave harmonics, and their coefficients are obtained in the spectral domain. The approach is applied to both single element and array structures and resulting radiation patterns are examined and compared with commercial software simulations. In addition, vector rotation and coordinate mapping techniques are employed to extend the study to arrays consisting of elements with equal geometry and feeding.

Keywords: Spherical Antennas, Spherical Antenna Arrays, Cavity Method, Spherical Wave Harmonics, Vector-Legendre Transform

ÖZ

KÜRESEL-DİKDÖRTGENSEL BASKI ANTEN VE ANTEN DİZİLERİNİN KOVUK YÖNTEMİYLE ANALİZİ

Demir, Oğuz
Yüksek Lisans, Elektrik Elektronik Mühendisliği Bölümü
Tez Yöneticisi : Prof. Dr. Gülbin Dural

Şubat 2017, 108 sayfa

Çeşitli mikroşerit baskı antenlerin kullanımı, avantajlı özellikleri ve dolayısıyla birçok uygulamada kullanılıyor olmaları sebebiyle elektro-manyetik endüstrisinde farklı alanlarda sıklıkla karşılaşılan ihtiyaçlardan biridir. Antenlerin bu alanlarda kullanımını sağlamak için doğru şekilde incelenmeleri bir gereksinim olmaktadır. Bu inceleme, çok kesin sonuçlar veren tamamen numerik yöntemlerle yapılabilse de, bu süreçte gerekli olan karmaşık işlemler yüksek hesaplama yükü oluşturur; bu nedenle kaliteli bir benzetim yazılımına ihtiyaç duyulur. Bu tez çalışmasında, iletken bir kürenin üzerine oturtulmuş küresel-dikdörtgensel mikroşerit baskı anten ve anten dizilerinin temel olarak kovuk yöntemiyle analizi üzerine yoğunlaşılmış ve küre üzerinde meydana gelen eşdeğer manyetik akım yoğunlukları elde edilmiştir. Akımların kürenin varlığında yarattıkları yayılım, küresel dalga harmonikleri ile modellenmiş ve harmoniklerin katsayıları bulunmuştur. Aynı yaklaşım küresel anten dizisi için de uygulanmış, elde edilen radyasyon desenleri incelenmiş ve benzetim sonuçlarıyla karşılaştırılmıştır. Ek olarak, vektör çevirimi ve kordinat eşleme teknikleri ile eş elemanlı ve eş beslemeli anten dizilerinin analizi de mümkün kılınmıştır.

Keywords: Küresel Antenler, Küresel Anten Dizileri, Kovuk Yöntemi, Küresel Dalga Harmonikleri, Vektör-Legendre Dönüşümü

To my Family…

ACKNOWLEDGMENTS

First of all, I wish to express my deepest gratitude to my supervisor Prof. Dr. Gülbin Dural for her advice, criticism and encouragements throughout this research. Her insight and approach to problems definitely gave me an invaluable engineering experience. This work would be too difficult to accomplish without her continuous guidance.

I would like to thank all members of the examining committee, especially Mustafa Kuzuoğlu, for their inspiring comments and ideas which encouraged the further improvement of this research.

I would also like to express my sincere thanks to ASELSAN INC. and my colleagues there for their valuable support and understanding.

I would like to thank my friends for their encouragement and their efforts to keep my motivation as high as possible all the time.

Finally, this acknowledgment would be incomplete without expressing my gratitude and thanks to my family for their endless support and patience, for their love that kept me going in most stressful situations and for always believing in me in any case or circumstances. Without them, this work could never be successfully completed.

TABLE OF CONTENTS

LIST OF TABLES

TABLES

LIST OF FIGURES

FIGURES

CHAPTER 1

INTRODUCTION

1.1. Microstrip Printed Antennas

Microstrip device technology is employed on many microwave circuit elements such as transmission lines, resonators, filters and antennas. Among these devices, microstrip patch antennas are commonly used type of antennas in wide range of applications. Even though these antennas are poor radiators with low bandwidth and efficiency, they are usually preferred due to their attractive properties such as having light weight, conformable structure, low profile and low fabrication costs [1]. These unique properties clarify the reason why these antennas have more popularity among many other antenna types.

Some of the applications in which microstrip antennas have priority are spacecraft and aircraft applications [2]-[4] due to their low profile and conformable characteristics. Their mounting on the surface of airships does not deteriorate the special aerodynamic properties they must have in order to ensure the safety of flights. Biological implantation and telemetry [5], [6] are other application areas of microstrip antennas due to their compact, small and thin structures. Lately, microstrip antenna concept is also preferred in implementation of wearable antennas and embroidered antennas [7]. These applications require light weight, flexible and conformable antenna types which are a few of the unique properties of microstrip antennas.

The microstrip antennas can be utilized in various geometries because of their conformable structure. Planar, cylindrical and spherical antennas are the most common

printed antenna geometries that are implemented in the industry. Despite their geometrical diversity, the same analysis methods are applicable to each one of them. There are several methods to analyze these antennas. Some methods are immitance approach [8] and generalized transmission line method [9], [10] both of which are preferred mainly for stratified microstrip printed patch structures but are also applicable to ordinary printed patch antennas. Another one of them is a numerical approach, namely full wave (spectral domain or method of moments) analysis, which requires complex calculations and formulations [11], [12], [50] and it is usually implemented by commercial software programs designed for this particular solution approach. Another widely used method is the cavity model approach which also requires completely analytical solution process [13]-[15]. All of these methods provide solutions with different level of accuracy, insight and computation load, hence they should be chosen depending on the needs.

The radiation pattern characteristic of a printed patch antenna is an important concern for antenna engineers. Methods that give reliable, accurate and quick results for patterns are desired in such a case. Due to the high accuracy level of the solutions, full wave analysis is the most common approach, despite its requirement for heavy computation processes. Nevertheless, the cavity method can provide comparable accuracy levels to some extent for certain type of far-field pattern problems without complex algorithms or formulations, hence with faster results. Therefore, it remains as a similarly accurate and practical way of approaching applications regarding antenna radiation patterns.

1.2. Spherical Antenna Arrays

It is recognized that microstrip antennas have some disadvantageous properties such as narrow bandwidth, low efficiency and large beamwidth. There are a few methods to compensate for these drawbacks one of which is increasing dielectric thickness for narrower beamwidth [16], but this attempt results in a drop in the efficiency. As seen, the trade-off between these properties forces the degradation of some antenna fea-

tures while improving some others. Therefore, microstrip antennas are better utilized by means of various antenna array formations and phased array algorithms [17].

When the hemispherical or spherical radiation coverage is required, spherical microstrip antennas are primary choice in applications. The spherical arrays are preferred form of antenna systems for applications such as satellite communications [18]. The analysis of spherical antenna arrays are generally performed by full-wave analysis approach [19]-[21] since the process includes significant effects such as mutual coupling that may degrade the array performance completely once ignored. Nevertheless, the analytical methods like cavity model can also be applied on this type of array structures in many cases as long as aforementioned effects have minimal impact on the results. In literature, there are cavity method analyses on various antenna types [22]-[26], however, there are quite a few studies about the application of this method on spherical antennas in an array format. Although it is known that cavity method provides comparable results with respect to the full-wave analysis regarding the radiation pattern characteristics, the comparison of results for array structures still needs evaluation.

Direction finding and beam forming are other branches of antenna array applications. These implementations require many processes like detection, filtering, signal processing etc. When direction finding is considered, the detection part is realized by creating narrow beams that are able to span the space of interest around the antenna system. The methods to generate such patterns include mechanical rotation of antennas or the phased array structures where various antenna types can be utilized including microstrip printed antennas. There have been quite a lot of studies about these applications that cover geometries like planar [27] and cylindrical [28] arrays. On the other hand, the spherical antenna geometry usage for such studies is still in development stage; therefore, it seems necessary to make a mention of their possible implementation in the future studies.

1.3. Thesis Motivation

In this thesis, cavity model is employed to analyze the characteristics of a spherical-rectangular microstip antenna and antenna arrays. The outcome of this model is utilized by means of spherical wave harmonic expansions of field vectors and Vector-Legendre transformation. The aim of the study is to derive the far-field radiation patterns of a spherical-rectangular printed antenna, then extending the work to different spherical antenna geometries and array structures. Comparison of the outcomes with the computer simulated results is also intended.

1.4. Thesis Outline

In this thesis, a brief introduction to microstrip antenna and antenna arrays and possible analysis methods are given in Chapter 1. The methods to analyze a planar microstrip antenna are deeply described in Chapter 2 in which the main focus is the cavity model approach. Next, the application of cavity model on spherical-rectangular microstrip antennas and antenna arrays by utilizing both the spherical wave harmonic expansion method and Vector-Legendre transformation for forcing boundary conditions in the spectral domain is presented in Chapter 3. The analytical results of cavity model are demonstrated and compared with computer simulations in Chapter 4 for various types of antenna elements and array structures. Finally, the conclusions regarding the strength of the cavity method are made in Chapter 5 along with possible future work.

CHAPTER 2

THEORY AND ANALYSIS OF MICROSTRIP ANTENNAS

2.1. Introduction:

In this chapter, the theory behind the microstip antennas and main analysis methods are given. The section 2.2 covers some background on microstrip antennas. Sections 2.3 and 2.4 give general information about the feeding and analysis techniques respectively. In section 2.4, the detailed analysis of cavity model for planar microstrip antennas is also presented.

2.2. Microstrip Patch Antennas:

A patch antenna mainly consists of a ground plane and a metallic patch placed over the ground plane with a very thin dielectric slab between them as shown in Figure 2.1. Their simplicity is the main reason they are used in many antenna engineering applications. They are light and easy-to-fabricate structures which can be conformed on various types of surface. Despite such advantages, these antennas are naturally poor radiators. Their bandwidth is narrow and beamwidth is quite large. Furthermore, they have lower efficiency compared to many antenna types in this industry. Nevertheless, these negative properties do not prevent the widespread use of patch antennas.

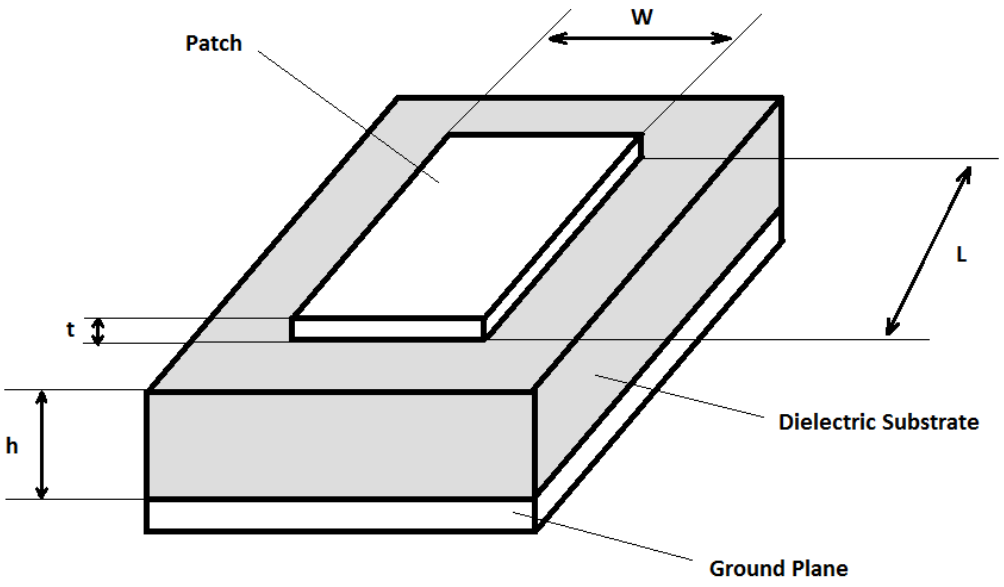

Figure 2.1: A typical rectangular microstrip antenna

The conducting patch is generally preferred to be copper. Its geometrical dimensions and shape determines the basic antenna parameters and its operation consequently. The dielectric material under the patch has significant importance also, considering its effects on loss tangent, operation bandwidth, resonance frequency and beamwitdh of the radiation. For example, the radiation efficiency of patch antenna drops as the loss of the dielectric increases. However, the bandwidth of the antenna widens at the same time. Therefore, application of such antennas requires a good comprehension of the effects caused by the dielectric substrate and patch geometries and materials they are made of.

The printed patches can be in various shapes such as rectangular, circular, triangular etc. as depending on the application requirements. Some typical shapes are indicated in Figure 2.2.

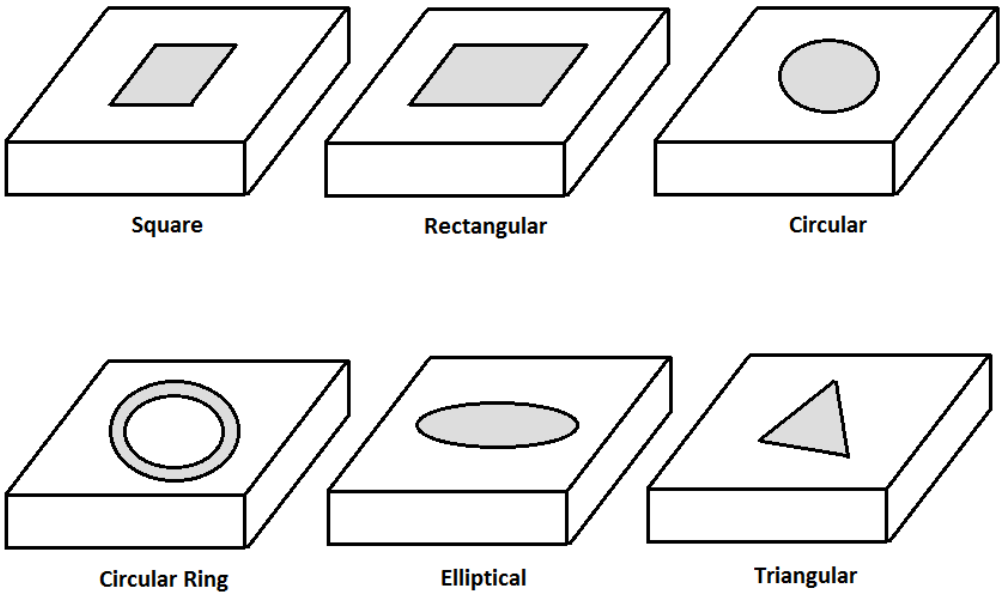

Figure 2.2: Various microstrip antenna shapes

The radiation of printed patch antennas is highly dependent on the shape of the patch element. The radiation essentially develops due to the fringing fields occurring between the patch edges and the ground plane. As the edges are in different geometries, the expected performances of these antennas are also different.

The patch thickness of these antennas is quite small compared to the total thickness of the element. Their low profile structure allows them to be used in areas where aerodynamics is a significant concern such as aircraft, spacecraft and missile applications. These antennas are also preferred in telemetry and communication applications such as cellular phones as embedded antennas due to their small size and robustness.

The physical structure of printed patch antennas can be modeled as a resonator with a very high quality factor (Q). This is problematic considering the effect of high Q-factor on the operation bandwidth. These antennas have considerably low operation bandwidth. Furthermore, their radiation efficiency is quite low due to losses caused by dielectric and conduction losses together with surface wave losses. The surface waves are developed on the patch surfaces and degrades the performance of the antenna by absorbing the power fed to the antenna element. However, there are some

precautions for this phenomenon such as keeping the dielectric thickness sufficiently small which improves the efficiency overall.

All patch antenna elements are passive structures and must be excited by an external power source. They need a feeding mechanism so that they radiate a specific amount of power delivered to them directly proportional to their radiation efficiency.

2.3. Feeding Structures of Patch Antennas:

The feed types that are commonly used for the excitation of patch antennas are microstrip line feed, coaxial probe, aperture coupling and proximity coupling. Depending on the patch geometry and application, appropriate one of these antenna feed types can be utilized. All the feeding techniques have the purpose of delivering the power to the patch antenna and forcing it to radiate. The feeding mechanism must be as efficient as possible or it may degrade the antenna performance due to losses. Therefore, it is necessary to note that feed of an antenna plays an essential role in its effective operation.

2.3.1. Microstrip Line Feed:

The conformable nature of printed patch antennas has significant advantage in many industrial applications. Microstrip line feeding does not affect the conformability in a negative way which can be considered as a beneficial aspect of this feeding type. In this structure, printed antenna is fed by a microstrip line from an appropriate side of the patch as in Figure 2.3. The line is at the same level as the printed patch, therefore, the fabrication is also quite simple and modeling is easy. Nevertheless, thickness of the substrate should be kept small and width of the line should be narrow enough to prevent unwanted emissions, bandwidth deterioration and surface waves.

The microstrip feeding line has the same properties as the patch. However, it is narrower in width and it has different impedance from the edge of the patch. Generally, the patch impedances are very high at the edges, because current flow at these regions is almost non-existent. Consequently, the impedance values at the side-edges of the patch antennas are quite high. The impedance of feeding line and the patch can be matched only if the feed is set further into the patch where voltages and currents provide lower impedance. The technique is called inset feeding and the inset cuts are employed to enable feeding at a more suitable location in the patch. Such a structure is also observed in Figure 2.3. The inset cut length and width changes depending on the impedance to be matched, frequency of operation and patch geometry and calculations steps are given in [29].

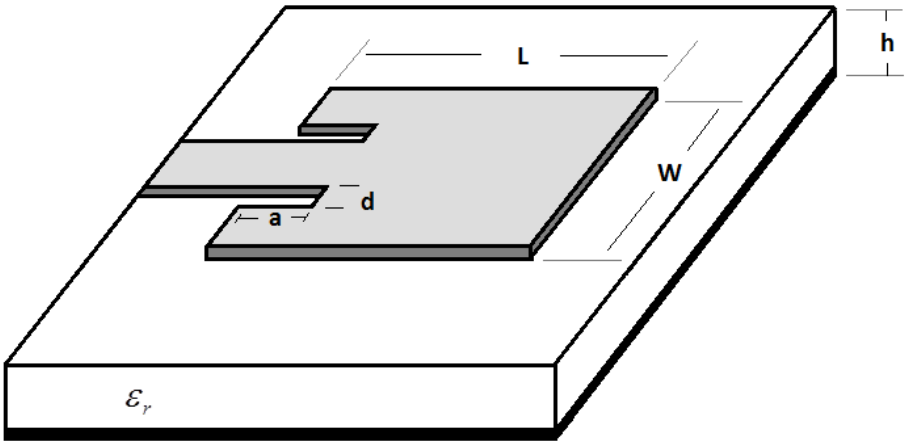

Figure 2.3: A microstrip patch antenna with line feed

The inset cut structures do not weaken the radiation if the cut is placed with necessary caution. The currents fed to the antenna flow in the same direction as the feeding direction throughout the patch area if the fundamental mode operation is considered and feeding is applied from the short edge of the patch. The electric fields generated at the edges also follow the same direction as depicted in Figure 2.4. Therefore, the inset cuts do not prevent the flow of energy through the antenna as long as they are not badly scaled. Otherwise, current directions are distorted and unwanted radiations are possibly exist which degrades the performance.

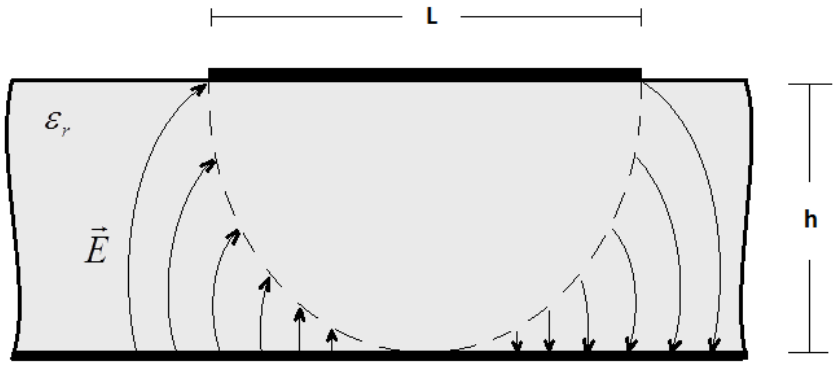

Figure 2.4: Cross-section view of a microstrip antenna demonstrating the fundamental mode (TM_{01}) E-field distribution

Although microstrip line feeding is preferable due to its simplicity, its use is restricted to rectangle shaped patch antennas. There are various types of shapes such as circular, ring, triangular and sector etc. to implement microstrip antennas. Therefore, impedance matching becomes more difficult with line feeding option. Application of other feeding techniques can be more practical and accurate in such cases.

2.3.2. Coaxial Line Feed:

The feeding of patch antennas can be difficult if microstrip line feed is implemented in various circumstances. Coaxial line feeding is an applicable alternative and a common technique for microstrip antennas. The coaxial line feeds patch antennas in the configuration depicted in Figure 2.5. The outer conductor of the coaxial cable is soldered directly to the ground plane of the antenna. The inner conductor on the other hand penetrates the dielectric substrate all the way up to the patch element and feeds the antenna. Although the fabrication is slightly more complex compared to the microstrip line feeding, it is a preferable technique in the antenna industry for its simple fabrication process.

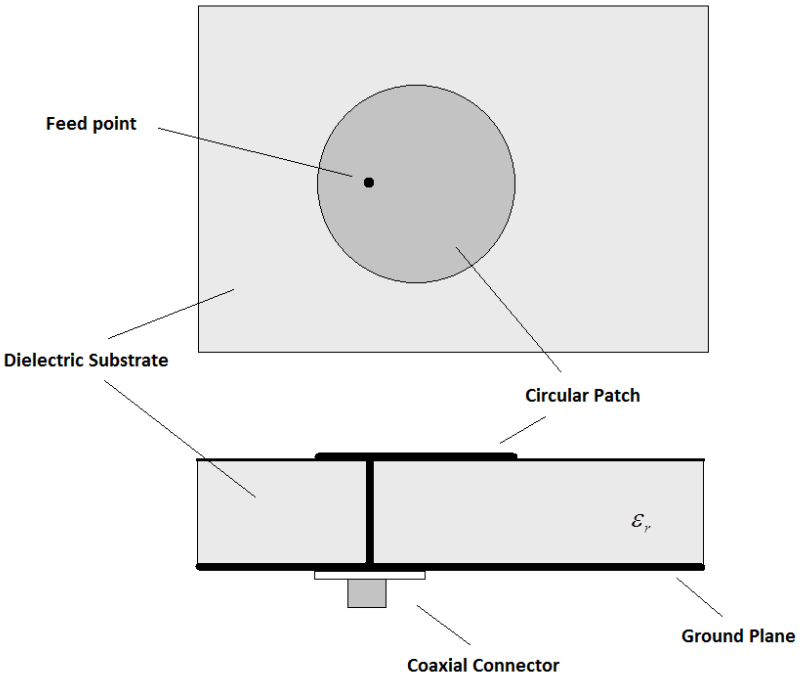

Figure 2.5: Circular patch antenna with a coaxial feed

The matching in this structure is implemented by connecting the line to an optimal location on the patch. The process does not require inset cuts placements on antenna which is an advantageous property. Furthermore, this feeding technique can be applied to rectangular patches as well as many other patch shapes. The accurate position for the feeding point is calculated by impedance formulations.

One of the problematic aspects of the coaxial feeding is its interaction with the dielectric substrate of the patch antenna. The connection line produces additional inductance for thick substrates generally making the matching a more complicated process. Another one is that the soldering requirement of the coaxial cable reduces the structure reliability. In addition, the modeling of a coaxial line feed is more difficult compared to the microstrip line feeding.

2.3.3. Aperture Coupled Feed:

The microstrip line and coaxial line feed techniques require that the feeding element makes a connection with the patch antenna directly. However, this structure usually ends up with spurious radiations to some extent. These unwanted emissions can be avoided with coupling concept introduced in this method. As the Figure 2.6 exhibits, the feeding microstrip line and the radiating patch are separated by a ground plane. The only interaction between the patch and the feed is maintained by the slot on the ground plane. Two dielectric layers exist with different dielectric constant and thickness. Energy flowing on the feed is coupled to the patch through the ground slot.

The matching of the feeding element depends on the aperture geometry and scale. Furthermore, the substrate dielectric constant and thickness can be adjusted to achieve better radiation.

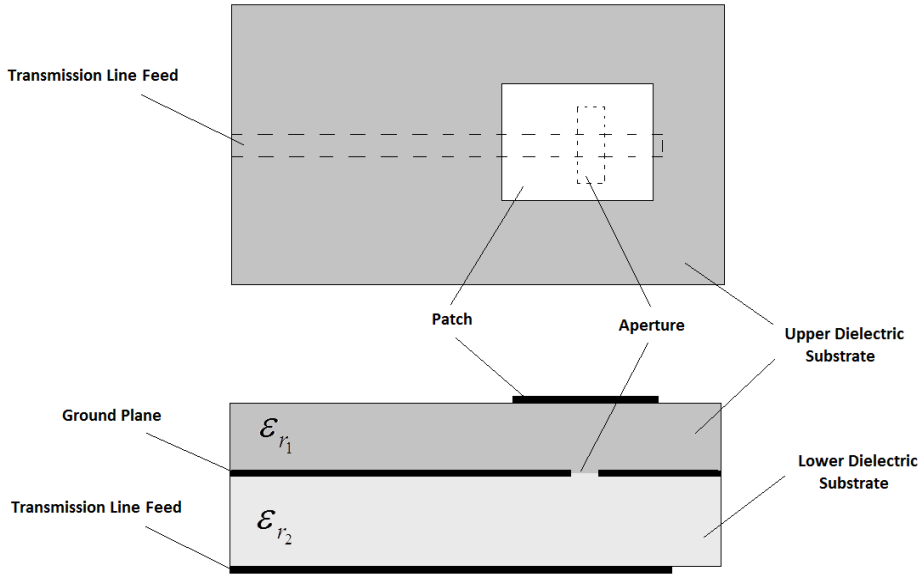

Figure 2.6: Aperture coupled feed structure

The fabrication of this feeding is quite difficult due to the large dielectric thickness. The bandwidth of such antennas is also narrow due to the natural behavior of the feeding aperture.

2.4. Analysis Methods:

Microstrip printed antennas can be analyzed by applying one of three most common techniques depending on the requirement of precision, accuracy and insight. These methods are the transmission line model, full wave analysis and the cavity method. Each one have their advantages and disadvantages making them quite useful for different cases.

The simplest of the aforementioned methods is the transmission line model. The patch antenna is modeled as a transmission line and its radiation behavior is derived analytically. It is easy to apply and gives a lot of insight; however, the solution has low accuracy. Full wave analysis is the most complex and strongest method based on the solution of field integral equations by means of moment method. Its high versatility and accuracy are compensated by the computation weight and low insight. The last approach is the cavity method which models the patch antenna as a dielectric loaded cavity. It is also an analytical approach with raised accuracy and insight with low versatility.

2.4.1. Transmission Line Model:

Transmission line model approach represents the microstrip antenna as a transmission line of width *W* and length *L* as depicted in Figure 2.7. The main idea is that the radiation is assumed to be emitted from two thin slots of height h with a separation of *L* forming a two element aperture array.

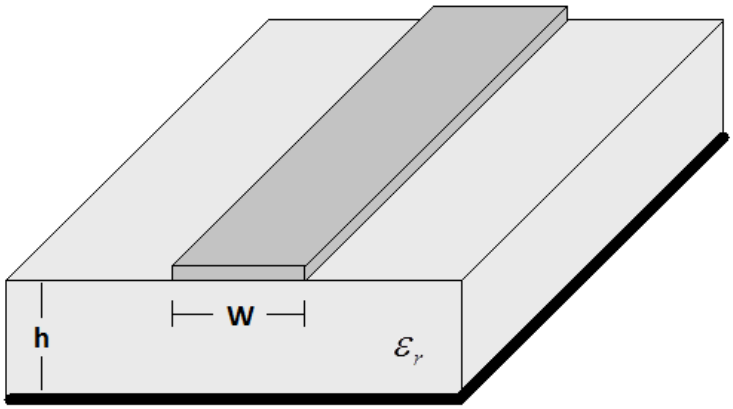

Figure 2.7: Modeling of a rectangular patch antenna as a microstrip line

A significant phenomenon in this model is the behavior of fringing effects taking place at the edges of the antenna patch. Naturally, the fields at the edge tend to follow an indirect route to the ground because of the discontinuity of the patch conductor. This effect is called the fringing effect which is actually the main cause of the radiation from microstrip printed antennas. The electric field lines that emerge from the patch do not follow a smooth path to the ground though, due to the substrate material placed between the patch and ground conductors as indicated in Figure 2.8. As the waves travel on the path, they are exposed to two different materials that have different dielectric constants. Consequently, refraction takes place when the fields travel from one dielectric to the other.

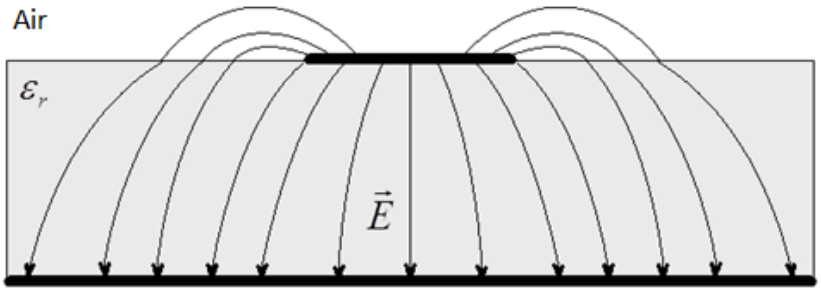

Figure 2.8: Behavior of the E-field lines at the air-dielectric boundary

The aforementioned behavior of fields prevents the total confinement of electric fields inside the dielectric substrate. The fields in these two different layers have dif-

ferent phase velocities as a result. This causes the waves travelling on the transmission line to be qTEM (quasi transverse electric magnetic) waves instead of pure TEM waves. For the sake of simplicity, this effect can be accounted for using an equivalent parameter called effective dielectric constant (ϵ_{eff}). Its value is lower than the dielectric constant of the substrate because some of the fields are exposed to the dielectric constant of air. This parameter can be calculated by [30]:

$$\varepsilon_{r_{eff}} = \frac{\varepsilon_r + 1}{2} + \frac{\varepsilon_r - 1}{2}\left[1 + 12\frac{h}{W}\right]^{-\frac{1}{2}} \tag{2.1}$$

where ϵ_r is the dielectric constant of the substrate, W and h are the geometrical parameters as given in Figure 2.7 and ϵ_{eff} is the effective dielectric constant when the second layer is air. The final equivalent view of the patch antenna is depicted in Figure 2.9.

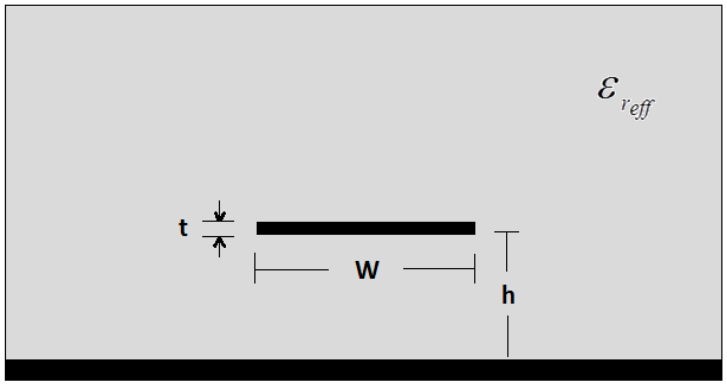

Figure 2.9: The equivalent microstrip line structure immersed in a substrate with ϵeff

Another important aspect of the fringing fields is that they follow a route a little longer than they normally would as in the case of uniform dielectric environment. The refraction of fields at the dielectric boundary causes them to reach further locations on the ground as indicated in Figure 2.8. Since the radiation of the patch antennas stem from this curvy locus, the electrical length of the antenna becomes larger than its physical length. As mentioned before, the sources of radiation are modeled to be the two opposite slots of the microstrip antenna. The fringing effects can be assumed to add a particular distance ($2.\Delta L$) to the length of the patch as in Figure 2.10.

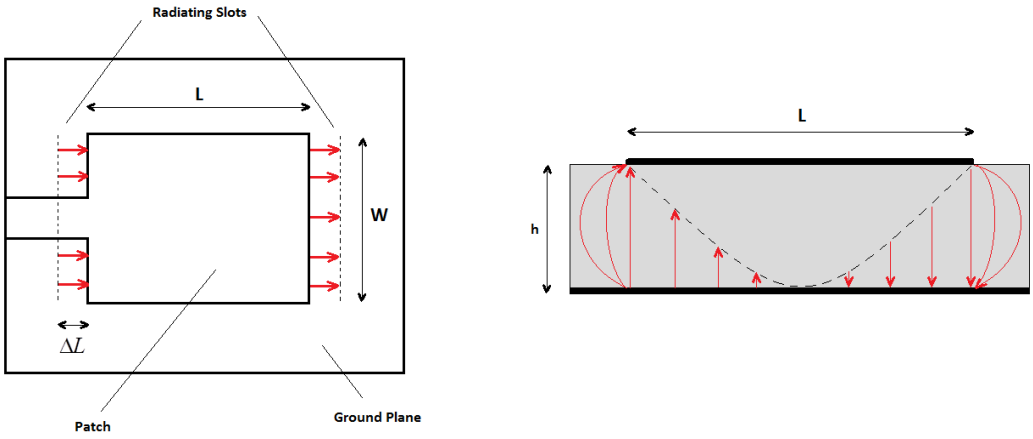

Figure 2.10: Top and side views of a microstrip patch antenna

The electrical length of antennas gives essential information on the radiation characteristics such as radiation frequency. Therefore, difference in the length must be calculated to obtain an effective length L_{eff} to continue the analysis [31], [32].

As the fundamental mode operation is excited at the wavelength of twice the electrical length of antenna, its electrical expansion must be taken into account to obtain the resonant frequency. The same expansion is applicable to all modes of operations affecting their frequencies as well. The operation frequencies for all modes can be derived using the formulation in [33] and the further improvement of the efficiency of microstrip antennas by adjusting the width of the patch area is exemplified in [34].

To sum up, the characteristics of microstrip antennas can be modeled as a transmission line which requires the calculation of significant parameters such as effective dielectric constant and effective antenna length to account for the effects of fringing fields. Furthermore, the model has a strong physical insight along with moderate accuracy. Even though it is a straightforward and easy method to follow, its area of application is restricted to the rectangular microstrip antennas. Therefore, the model is insufficient in analyzing printed antennas with any other shape.

2.4.2. Full Wave Analysis:

Full wave solution is a numerical approach that can be applied for the analysis of microstrip antennas. In this method, the planar surface of the patch and the volume inside the dielectric substrate are modeled with meshes. The aim of the method is to make use of the field-current relationships to approximate the fields and currents at every mesh point. The approximation precision is dependent on the choice of functions that are used to imitate the distribution of fields and currents.

The relationship between source and radiated fields are generally represented by integral equations called EFIE (Electric Field Integral Equation) or MFIE (Magnetic Field Integral Equation) which can have different forms depending on the problem [35]. These equations are quite difficult to solve using analytical formulations. Therefore, a numerical procedure is applied using the method of moments approach [36]. This approach is strong in problems where the complex interaction between source and load cannot be clearly defined.

The main purpose in the method of moments is to develop a formulation to solve the equation given below:

$$Lf(x) = g(x) \tag{2.2}$$

where L is a known linear operator applied on an unknown function resulting in the excitation function g which is also known since the source is explicit. The unknown function f represents the fields or currents to be obtained at the end of the formulation.

In order to find the unknown function, it is expanded so that it is represented as the linear combination of N known functions called basis functions as in (2.3):

$$f = \sum_{n=1}^{N} a_n f_n = a_1 f_1 + a_2 f_2 + \ldots\ldots\ldots + a_N f_N \tag{2.3}$$

where α_n is the unknown coefficient of each basis function f_n. The reason there are N basis functions is that it is assumed that there is a total of N meshes both on the conducting surface and in the dielectric volume together. The basis functions are applied on each of these meshes so that the problem is considered as a whole.

The number of meshes and the choice of basis functions to use are significant parameters affecting the accuracy of the method. There are various types of basis functions such as rectangular pulse, triangular, piecewise sinusoidal, truncated cosine etc. (Figure 2.11)

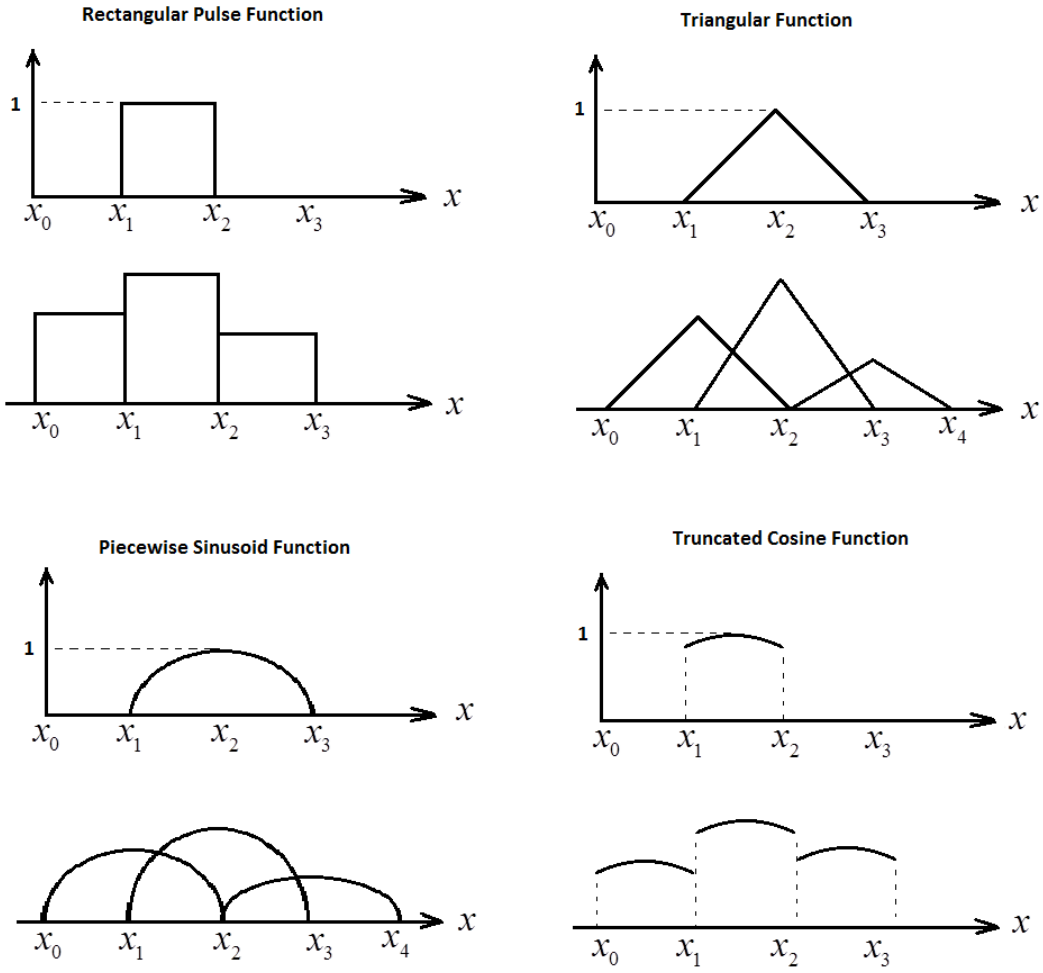

Figure 2.11: Common basis function types

The expanded version of unknown function is then substituted to (2.3) which yields:

$$L\left\{\sum_{n=1}^{N} a_n f_n(x)\right\} = g(x) \tag{2.4}$$

As it is known that L is a linear operator, the following equation is derived:

$$\sum_{n=1}^{N} a_n L f_n(x) = g(x) \tag{2.5}$$

(2.5) implies that the operator is now applied on known basis functions instead of an unknown function although the coefficients are still required to be found. The next step is to develop a residual error concept to derive an approximation to these coefficients. A residual error function is defined such that:

$$R(x) = \sum_{n=1}^{N} a_n L f_n(x) - g(x) \tag{2.6}$$

The minimization of (2.6) is necessary to ensure the high accuracy of the method. In order to achieve this, weighting (testing) functions are introduced. The generally preferred type of functions are impulse or pulse functions, however, types of functions can be the same as the chosen basis functions which is a procedure called Galerkin's method [37].

Weighting functions are chosen in a way that the main equation (2.2) is satisfied at every sample point. Furthermore, any singularities that rise due to the integral equation of interest are removed or reduced if a proper weighting function is applied.

The process requires that the inner products weighting functions with basis and source functions are calculated and the resulting residual error in (2.6) is equated to zero. This step yields:

$$\sum_{n=1}^{N} a_n \langle w_m, L f_n(x) \rangle = \langle w_m, g(x) \rangle \qquad \text{for} \quad m = 1,2,\ldots,N \tag{2.7}$$

where w_m denotes the weighting functions. The inner product operator can be defined as:

$$\langle u, v \rangle = \int_{\Omega} u v^{*} d\Omega \tag{2.8}$$

such that the integration of complex conjugate multiplication over the domain Ω is performed.

The implication of (2.7) is that each basis and source function is interacted with each weighting function so that the whole field current relationships of each mesh are considered and included in the formulation. In addition, the accuracy of this interaction model is quite high since the residual error function is minimized to zero.

The set of equations given in (2.7) can be transformed to matrix form as follows:

$$[I_{mn}][a_n] = [g_m] \tag{2.9}$$

such that

$$[I_{mn}] = \begin{bmatrix} \langle w_1, Lf_1 \rangle & \langle w_1, Lf_2 \rangle & ..... & \langle w_1, Lf_n \rangle \\ \langle w_2, Lf_1 \rangle & \langle w_2, Lf_2 \rangle & ..... & \langle w_2, Lf_n \rangle \\ ..... & ..... & ..... & ..... \\ \langle w_m, Lf_1 \rangle & \langle w_m, Lf_2 \rangle & ..... & \langle w_m, Lf_n \rangle \end{bmatrix} \tag{2.10}$$

$$[a_n] = \begin{bmatrix} a_1 \\ a_2 \\ \cdots \\ a_n \end{bmatrix} \quad \text{and} \quad [g_m] = \begin{bmatrix} \langle w_1, g \rangle \\ \langle w_2, g \rangle \\ \cdots \\ \langle w_m, g \rangle \end{bmatrix} \tag{2.11}$$

I, α and *g* are MoM (Method of Moments) matrix, coefficient matrix and source matrix respectively. Finally, the coefficients are obtained by means of the (2.12) if MoM matrix is non-singular.

$$[a_n] = [I_{mn}]^{-1}[g_m] \tag{2.12}$$

As a result, the unknown function of currents or fields in (2.3) can be explicitly written. As mentioned before, the choice of basis and testing functions depending on the geometry of the problem and the number of meshes created on the structure of interest are main parameters that affect the accuracy of this method. Carelessly chosen weighting functions may fail in handling the singularities and leads to high residual error values. Besides, a proper meshing of the elements which form the problem is a must if highly accurate solution is aimed.

To conclude, the full wave analysis is a numerical approach to analyze microstrip antennas. It has extreme accuracy compared to analytical methods in approximating the field and currents in the system. In addition, it is a versatile method which can be applied to printed antennas of arbitrary shapes. Nevertheless, it has a high computation load and low insight.

2.4.3. Cavity Model:

Cavity model approach is an analytical method which represents the microstrip antenna as a dielectric loaded cavity. In this section, theory and analysis of cavity model is presented.

2.4.3.1. Theory:

The main idea is that a microstrip antenna with very thin dielectric substrate can be assumed to be a cavity which is bounded by perfect electric and magnetic conductor walls. Also, the fields inside the thin dielectric layer are considered not to be changing much in value in the normal direction to the patch ground. The equivalent cur-

rents developed by this cavity space confining fields in itself are utilized to derive the radiation behavior of the microstrip antenna.

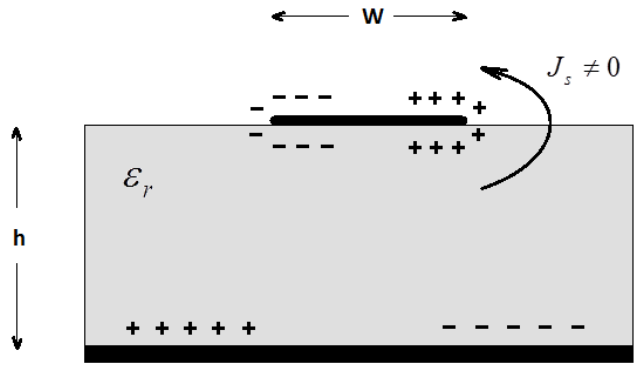

Figure 2.12: Charge distribution and movements on a microstrip patch

The charge distribution of an arbitrary rectangular microstrip antenna in operation can be observed in Figure 2.12. The positive and negative charges on the patch tend to flow in the direction depicted while the antenna is fed with power if the dielectric layer height *h* is large enough. The reason is that the similar charges on the ground and patch surfaces repel each other. Likewise, opposite charges cause attractive forces at the other end of the patch. As a result, a surface current flow J_s is supported on the antenna from the bottom surface of the patch to the top surface as discussed in [38].

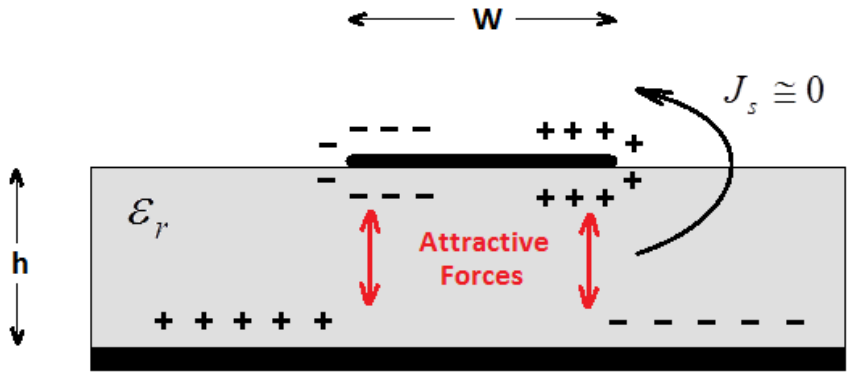

Figure 2.13: Charge distribution of a microstrip patch with thin dielectric substrate

If the dielectric substrate height is reduced to a much lower size keeping the printed patch electrically very close to the ground plane while keeping the patch width *W* constant, the charge behaviors start to change. The attractive forces between the opposite charges on the patch and ground become overwhelming. The electrical forces that cause the surface current flow on the patch are dominated by this attraction and cannot effectively support the flow any more as indicated in Figure 2.13. Therefore, the current on the surface of patch greatly drops. The boundary conditions at the edge of the patch demands that magnetic fields cannot emerge at the sides of antenna due to this minimized value of current flow. Finally, knowing that the sides of the antenna cannot support magnetic fields, these side planes can be assumed to be PMC (Perfect Magnetic Conductor) walls. Considering the PEC (Perfect Electric Conductor) top and bottom walls of the microstrip antenna and its four PMC side walls, a dielectric loaded cavity is assumed to be formed as in Figure 2.14 by the effects explained in this part.

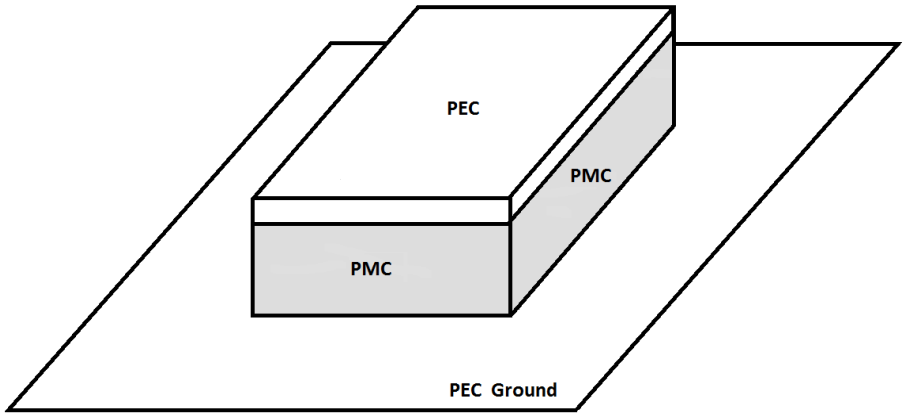

Figure 2.14: Equivalent structure of the sides of a dielectric loaded microstrip cavity

A cavity modeled with perfect elements such as lossless conductors and dielectric substrate cannot radiate energy, instead, it behaves more like a resonator. Its input impedance becomes purely reactive and the energy delivered to the antenna is totally reflected back to the source. Therefore, the losses must be considered and included in the models as a resistance as depicted in Figure 2.15. The resistance represents conductor losses, dielectric losses and radiation losses of the antenna system.

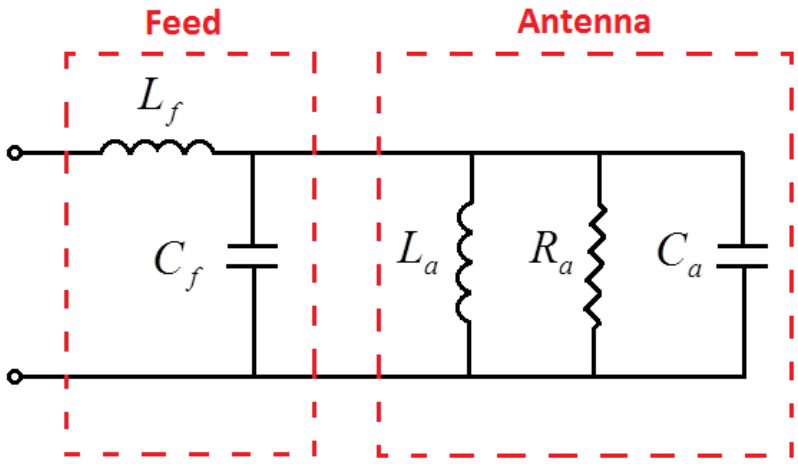

Figure 2.15: The equivalent circuit model of a microstrip antenna

The antenna properties of the lossy cavity are described by the effective loss tangent, δ_{eff}. As mentioned in [39], the effective loss tangent can be calculated from following equation:

$$\delta_{eff} = \frac{1}{Q_T} = \frac{1}{Q_d} + \frac{1}{Q_c} + \frac{1}{Q_r} \tag{2.13}$$

where Q_d, Q_c, Q_r and Q_T are quality factors for the dielectric substrate, the conductors, radiation and the total system respectively.

To sum up, cavity model is a straightforward, simple analytical approach with high level of insight where the microstrip antenna is modeled as a dielectric loaded cavity. The effective loss tangent is also considered in the method to ensure the radiation behavior of the antenna is included in the analysis. The following section explains the procedure for the utilization of boundary conditions on the side walls to derive the fields inside cavity and the equivalent current densities to obtain the properties of the antenna such as radiation pattern and input impedance.

2.4.3.2. Analysis:

As mentioned in the previous section, the microstrip antenna can be represented as a dielectric loaded cavity with PMC side walls and PEC top and bottom walls. The fields that are confined in the dielectric inside this structure can be obtained by solving Helmholtz equation. It is important to note at this point that TE_z (transverse electric to *z*) modes cannot be supported in the structure given in Figure 2.16.

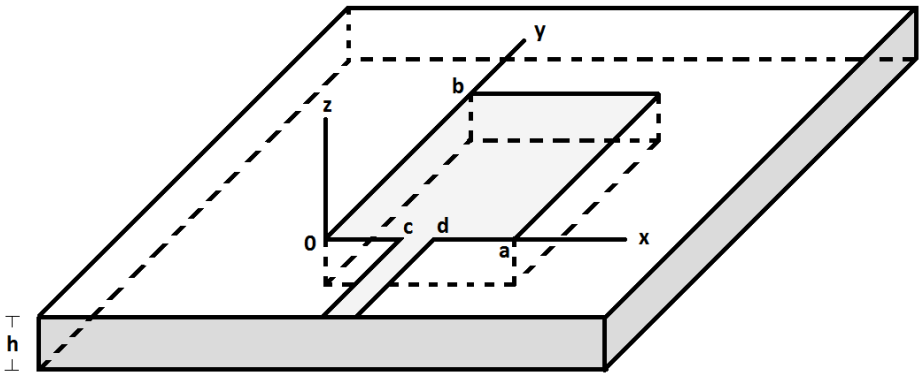

Figure 2.16: Dimensions of a rectangular microstip antenna with line feed

The patch of the antenna is in close proximity with the ground plane and both are PEC walls. TE_z mode has *z* directed magnetic field components, that is, normal to the PEC ground. According to the image theory, magnetic fields normal to PEC walls are negated by their image [29] and become non-effective as Figure 2.17 points out.

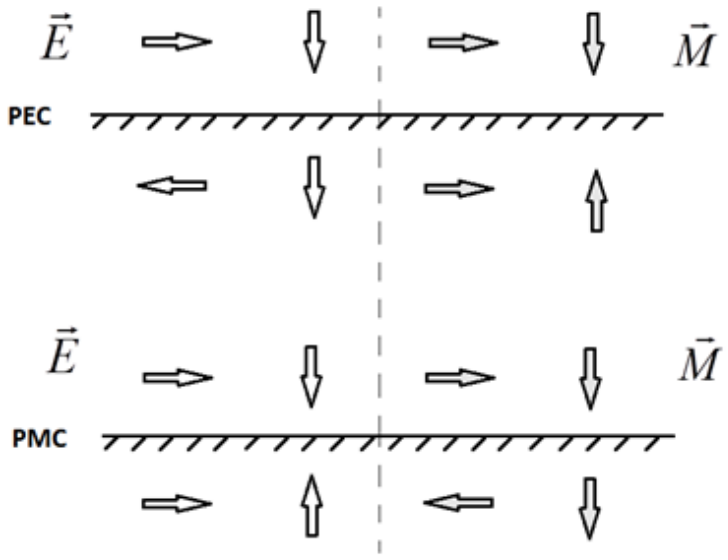

Figure 2.17: Summary of the image theory for PEC and PMC boundaries

The supported modes in the dielectric region are therefore TM_z (transverse magnetic to *z*) modes. The modes must satisfy the Helmholtz equation for planar structures [40]:

$$\left(\nabla^2 + k^2\right)E_z = j\omega\mu J\vec{z} \tag{2.14}$$

By neglecting their *z* components due to thin dielectric layer, wave functions and wave numbers for each resonant mode can be represented as:

$$\psi_{mn} = \cos\frac{m\pi}{a}x\cos\frac{n\pi}{b}y \tag{2.15}$$

$$k_{mn} = \sqrt{\left(\frac{m\pi}{a}\right)^2 + \left(\frac{n\pi}{b}\right)^2} \tag{2.16}$$

where (2.15) is the solution for homogeneous part of Helmholtz equation in (2.14). The solution procedure that makes use of only the homogeneous part does neglect the feed concept. Therefore, effect of the excitation is added to the solution by calculating its effect on each orthogonal resonant mode and summing them up for the final wave function as in the equations (2.17) and (2.18) respectively [14]:

$$M_d = j\omega\mu\sum_m \frac{1}{k^2 - k_m^2}\frac{\langle J\psi_m \rangle}{\langle \psi_m \psi_m \rangle} \tag{2.17}$$

$$\psi = \sum_d M_d \psi_d \tag{2.18}$$

such that

$$\langle J\psi_m \rangle = \int J\psi_m^* ds \tag{2.19}$$

$$\langle \psi_m \psi_m \rangle = \int \psi_m \psi_m^* dv \tag{2.20}$$

where * denotes the complex conjugate. There seems to be a problematic part in (2.17) at first glance considering that the denominator of the expression blows when the contribution of the operation mode is evaluated. Because, wave function parameters becomes equal at resonance frequency maintaining the equality $k^2 - k_m^2 = 0$. This would be the case if the cavity were a lossless structure and due to its resonance, energy would be infinite for that mode of operation where any other mode would be negligible. However, the antenna has lossy elements such as the dielectric substrate; thus, the dielectric loss tangent parameter must be taken into account [40]. As the most effective loss contribution comes from the dielectric, considering only its effect is sufficient:

$$\varepsilon = \varepsilon_0 \varepsilon_r (1 - j\delta) \tag{2.21}$$

$$k_d^2 = \omega^2 \mu_0 \varepsilon = k_0^2 \varepsilon_r (1 - j\delta) \tag{2.22}$$

then (2.18) turns out to be,

$$E_z = j\omega\mu_0 \sum_m \sum_n \frac{1}{k_d^2 - k_{mn}^2}\frac{\langle J_z \psi_{mn}^* \rangle}{\langle \psi_{mn} \psi_{mn}^* \rangle}\psi_{mn} \tag{2.23}$$

If a more accurate solution is required, dielectric loss tangent parameter can be replaced by the effective loss tangent as suggested in [55] since field lines also travel in the air region:

$$k_{eff}^2 = \omega^2 \mu_0 \varepsilon_{eff} = k_0^2 \varepsilon_r \left(1 - j\delta_{eff}\right) \tag{2.24}$$

$$E_z = j\omega\mu_0 \sum_m \sum_n \frac{1}{k_{eff}^2 - k_{mn}^2} \frac{\left\langle J_z \psi_{mn}^* \right\rangle}{\left\langle \psi_{mn} \psi_{mn}^* \right\rangle} \psi_{mn} \tag{2.25}$$

The electric field confined inside the cavity is expressed in (2.25). Since the side walls are perfect magnetic conductors, boundary conditions can be utilized to derive equivalent magnetic currents that cause the radiation of energy:

$$\hat{n} \times \vec{E}_t = \vec{M}_s \Big|_{at\_each\_side\_wall} \tag{2.26}$$

An important point in (2.26) is that the currents are doubled due to the infinite ground approximation. The radiation analysis proceeds as if the antenna and its elements were removed and only the calculated magnetic current densities existed. The solution with this approximation is valid for the upper half space of the infinite ground.

There are four side walls; therefore, there are also four magnetic current elements around the structure. However, it should be noted that the field distribution in fundamental frequency is such that two of these currents cancel the far-field radiation effects of each other since they are in opposite directions and in very close proximity. The effective current elements, on the other hand, have additive far-field radiation effect due to their similarity in direction and magnitude. Depending on the mode of operation, the field distribution varies and so does the equivalent magnetic current distribution on the periphery of the patch. This phenomenon is depicted in Figure 2.18 and Figure 2.19.

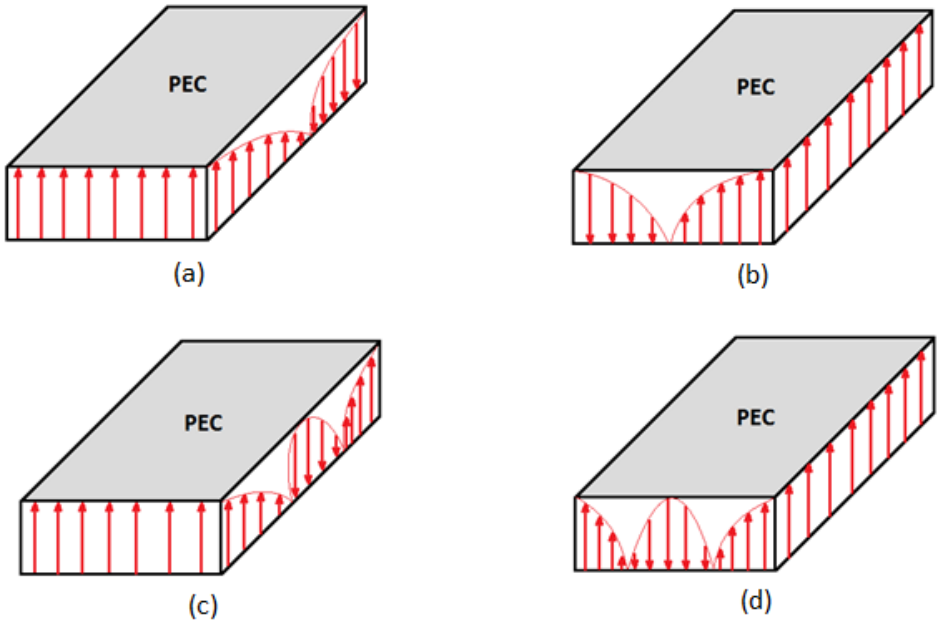

Figure 2.18: E-field distributions for different mode of operations: a) TM_{01} b) TM_{10} c) TM_{02} d) TM_{20}

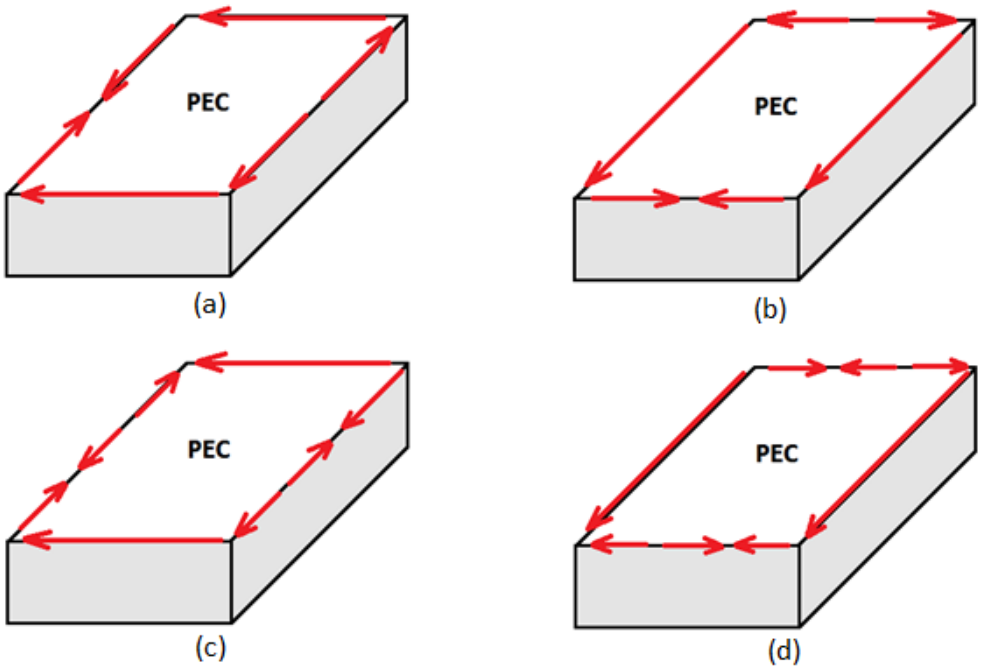

Figure 2.19: The equivalent magnetic current distributions for different mode of operations: a) TM_{01} b) TM_{10} c) TM_{02} d) TM_{20}

The radiation characteristic of the microstrip antenna can be derived by making use of the magnetic current distributions obtained in (2.26). The currents are assumed to be radiating in free-space without the presence of the antenna. Continuing the formulation steps with (2.27) to (2.29) results in the far-field radiation expression which concludes the far-field analysis:

$$F(r) = \varepsilon_0 \int_c \frac{M(r')}{4\pi|r-r'|} e^{-jk_0|r-r'|} dl(r') \tag{2.27}$$

then,

$$E_\theta = \eta H_\phi = jk_0 F_\phi = jk_0\left(-F_x \sin\phi + F_y \cos\phi\right) \tag{2.28}$$

$$E_\phi = -\eta H_\theta = -jk_0 F_\theta = -jk_0\left(F_x \cos\theta\cos\phi + F_y \cos\theta \sin\phi\right) \tag{2.29}$$

In addition to far-field radiation characteristics, the input impedance of the antenna can be calculated by means of the analysis so far. It is known that the total power delivered to the antenna from the feed is either radiated to space or dissipated by the lossy dielectric and conductor elements. (2.30) and (2.31) calculates the radiated power and the dissipated power in the antenna respectively [14]:

$$P_r = \mathrm{Re}\left[\int_0^{\pi/2}\int_0^{2\pi}\left(E_\theta H_\phi^* - E_\phi H_\theta^*\right) r^2 \sin\theta \, d\phi \, d\theta\right] \tag{2.30}$$

$$P_d = h\int_s \sigma_d |E|^2 ds + 2\int_s R|H|^2 ds \tag{2.31}$$

where E_θ, E_ϕ are far region radiated fields, E, H are fields inside the cavity and,

$$\sigma_d = n^2 \omega \varepsilon_0 \delta_d \tag{2.32}$$

$$R = \sqrt{\frac{\omega\mu}{2\sigma_c}} \tag{2.33}$$

where R is the skin-effect surface resistance of the conductor with conductivity σ_c and σ_d is the conductivity of the dielectric with loss tangent δ_d . The voltage at the feed can also be obtained by integrating the electric field at the insertion point as in (2.34) with the parameters given in Figure 2.16:

$$V = h\,E_{z_{avg}} = \frac{h}{d-c}\int_{c}^{d} E_z\Big|_{at\ feed}\,dl \tag{2.34}$$

Finally, the input conductance and susceptance can be calculated from [14]:

$$G = \frac{P_r + P_d}{|V|^2} \tag{2.35}$$

$$jB = -\frac{I}{V} \tag{2.36}$$

where

$$I = J(d-c) \tag{2.37}$$

As observed in equations from (2.30) to (2.37), input impedance is affected by the position of the feed and the type of materials that form the antenna. Besides, it is a mode dependent parameter and must be calculated each time the operation mode is changed because of frequency variation.

The analysis discussed in this section can also be applied to microstrip antennas with various simple shapes such as a disk antenna. Only difference is the proposed expression for the solution of Helmholtz equation. The rest of the steps are quite similar and straightforward until the input impedance calculations. Since circular or disk type antennas are preferred to be fed by a coaxial line instead of a microstrip line due to ease of fabrication, careful adjustments must be made to the impedance calculation steps to take any difference into account.

CHAPTER 3

ANALYSIS OF SPHERICAL RECTANGULAR MICROSTRIP ANTENNAS

3.1. Introduction

In this chapter, a brief presentation of spherical microstrip antennas is given in section 3.2. The thorough cavity model analysis of spherical-rectangular patch antennas and the methods to derive radiation pattern characteristics are given in details in section 3.3 and its subsequent sections.

3.2. Spherical Rectangular Patch Antennas:

Printed antennas are conformable to spherical structures as mentioned in the previous section. There are quite a few types of spherical antenna geometries such as wrapa-round, annular ring, circular disk, triangular and rectangular antennas (Figure 3.1). As the symmetrical type antennas are easier to cope with using cavity method analysis, there is more literature work on these geometries [41]-[44]. Due to the finite structure of rectangular antennas, the required cavity analysis is more challenging, thus they attract much less attention. The focus of this section is centered on the analysis of spherical rectangular antennas.

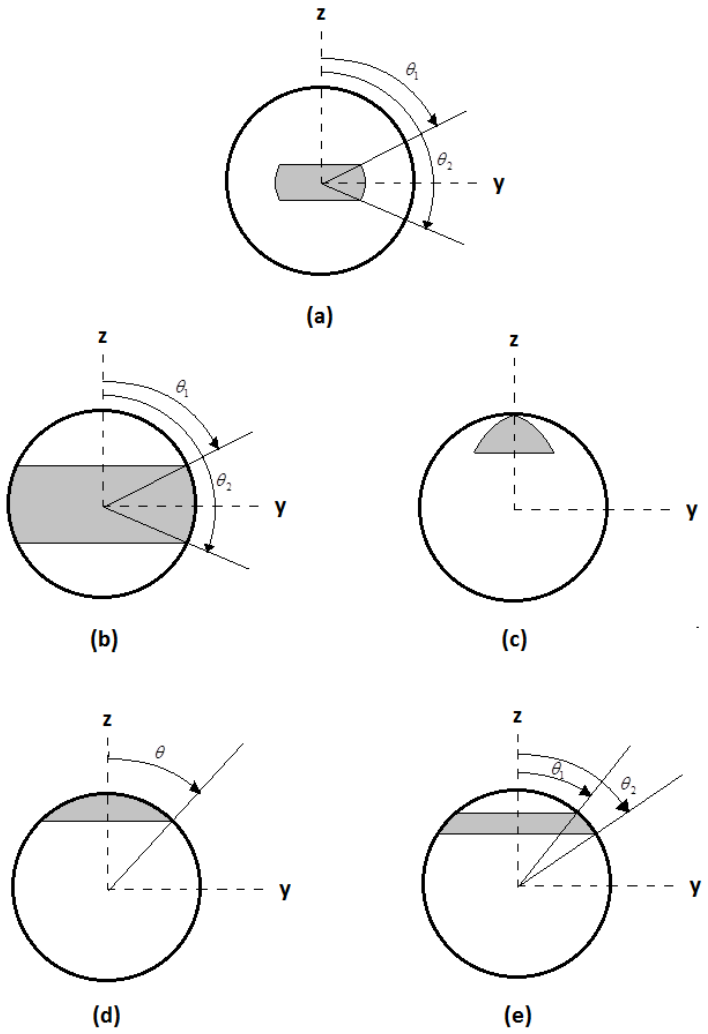

Figure 3.1: Different shapes of spherical microstrip antennas:
a) Rectangular, b) Wraparound, c) Triangular, d) Circular disk, e) Annular ring

The fields excited under the spherical rectangular patch are formulated by using cavity method approach and applying the boundary conditions accordingly. Later, the radiating current density elements are found by careful examination. Both the unbounded radiation and true radiation of these currents are calculated and compared. Furthermore, the input impedance of the rectangular antenna which depends on the excitation is observed.

3.3. Cavity Method Analysis:

The cavity field theory requires the field under the patch to be found so that equivalent current densities on the patch edges could be evaluated. These current densities will again be magnetic currents as in the planar patch case because radially directed magnetic currents cannot be supported by the system due to the perfect electric walls on the top and bottom of cavity. Consequently, the field generated inside cavity becomes dominantly TM_r mode while TE_r mode is highly attenuated.

The radial magnetic vector potential inside cavity must satisfy the scalar Helmholtz equation (3.1):

$$\left(\nabla^2 + k_d^2\right)\psi_r = 0 \tag{3.1}$$

where

$$k_d = \omega_0 \sqrt{\mu_0 \varepsilon_0 \varepsilon_r} \tag{3.2}$$

and

$$\nabla^2 \psi_r \neq \left(\nabla^2 \vec{\psi}\right)_r \tag{3.3}$$

In spherical case, Helmholtz equation is not satisfied by only Ψ_r because the laplacian of a scalar potential is not equal to the laplacian of a vector potential (3.3) as in [53]. Therefore, the expression A_r/r is proposed as the solution of spherical Helmholtz equation:

$$\left(\nabla^2 + k_d^2\right)\frac{A_r}{r} = 0 \tag{3.4}$$

such that

$$\left(\frac{A_r}{r}\right)_{mn} = (\psi_A)_{mn} = \left[a\hat{J}_n(k_d r) + b\hat{Y}_n(k_d r)\right]\left[cP_n^m(\cos\theta) + dQ_n^m(\cos\theta)\right] .\left[e\cos m\phi + f\sin m\phi\right] \quad (3.5)$$

The general expression for radial magnetic vector potential is (3.5), which needs to be forced by boundary conditions to eliminate the unknown coefficients [52]. This expression is formed by considering the volume under the antenna patch as a radially directed sectoral waveguide as depicted in Figure 3.2. The terms in the expression such as $\hat{J}_n$ and $\hat{Y}_n$ are Schelkunoff type Bessel functions of order *n*. Although, it was mentioned before that the thickness of the dielectric material under the patch should be quite thin for an accurate cavity model analysis, the corresponding radial Bessel functions are still considered for the sake of completeness. Also, P_n^m and Q_n^m are the associated Legendre functions [54] of first and second kind respectively, with order *m* and degree *n*. Bessel functions are chosen to be of Schelkunoff type [45] because they are more useful when the analysis is made on spherical structures.

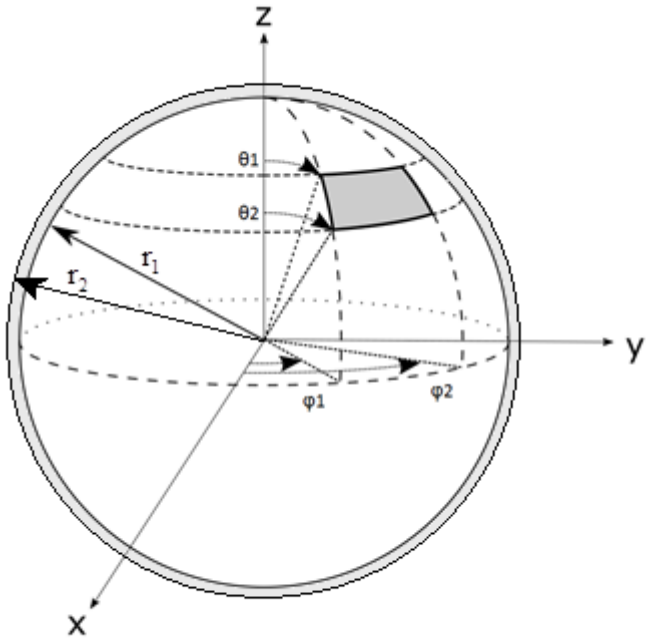

Figure 3.2: Dimensions of a spherical-rectangular microstrip antenna

Figure 3.2 depicts an arbitrarily positioned rectangular patch on the sphere of radius r_1. The patch antenna occupies a space between azimuthal angles of ϕ_1 and ϕ_2, and between elevation angles of θ_1 and θ_2. The thickness of the dielectric material is t and the distance of patch surface to the center of sphere is r_2. Similar to analysis of planar patch antennas, the dielectric volume between the patch and the sphere are considered as a cavity.

It is necessary to pinpoint that the Bessel and Legendre function types included in the solution (3.5) are chosen depending on position of the rectangular patch on the sphere. Both first and second kind associated Legendre functions are included since θ=0 and θ=180° are out of the solution region. Furthermore, both type-I and type-II Bessel functions are required for the center of the sphere is outside the solution space similarly.

After the determination of the magnetic vector potential expression, boundaries must be taken into account. There are six boundaries to be applied on the expression: the PEC walls at $r = r_1$ and $r = r_2$, the PMC walls at $\phi = \phi_1$ and $\phi = \phi_2$, and finally the other couple of PMC walls located at $\theta = \theta_1$ and $\theta = \theta_2$. These boundaries, once applied

on the potential expression, eliminate the unknown coefficients. Furthermore, a series of equations for the solution of propagation constant and for the mode numbers of cavity will emerge.

$$E_r = \frac{1}{j\omega\varepsilon}\left(\frac{\partial^2}{\partial r^2} + k^2\right)\psi_A \tag{3.6}$$

$$E_\theta = -\frac{1}{r\sin\theta}\frac{\partial\psi_F}{\partial\phi} + \frac{1}{j\omega\varepsilon r}\frac{\partial^2\psi_A}{\partial r\partial\theta} \tag{3.7}$$

$$E_\phi = \frac{1}{r}\frac{\partial\psi_F}{\partial\theta} + \frac{1}{j\omega\varepsilon r\sin\theta}\frac{\partial^2\psi_A}{\partial r\partial\phi} \tag{3.8}$$

$$H_r = \frac{1}{j\omega\mu}\left(\frac{\partial^2}{\partial r^2} + k^2\right)\psi_F \tag{3.9}$$

$$H_\theta = \frac{1}{r\sin\theta}\frac{\partial\psi_A}{\partial\phi} + \frac{1}{j\omega\mu r}\frac{\partial^2\psi_F}{\partial r\partial\theta} \tag{3.10}$$

$$H_\phi = -\frac{1}{r}\frac{\partial\psi_A}{\partial\theta} + \frac{1}{j\omega\mu r\sin\theta}\frac{\partial^2\psi_F}{\partial r\partial\phi} \tag{3.11}$$

The boundary conditions are not forced on the electric vector potential expression. Spherical electric and magnetic field modes generated by the magnetic vector potential Ψ_A must be considered since it is the dominant potential and Ψ_F is negligible. In other words, only TM_r modes exist inside the cavity as mentioned in the previous chapter. Therefore, substituting (3.5) in the spherical mode equations (3.6) to (3.11) and neglecting Ψ_F yields the expressions (3.12) to (3.17) which will have to satisfy boundary conditions on the cavity geometry.

$$E_r = \frac{1}{j\omega\varepsilon}\left(k_d^2\left[aJ_n'' + bY_n''\right] + k^2\left[aJ_n + bY_n\right]\right)\left[cP_n^m + dQ_n^m\right]\left[e\cos m\phi + f\sin m\phi\right] \tag{3.12}$$

$$E_\theta = -\frac{1}{j\omega\varepsilon r}k_d\sin\theta\left[aJ_n' + bY_n'\right]\left[cP_n^{m\prime} + dQ_n^{m\prime}\right]\left[e\cos m\phi + f\sin m\phi\right] \tag{3.13}$$

$$E_\phi = \frac{1}{j\omega\varepsilon r\sin\theta}k_d m\left[aJ_n' + bY_n'\right]\left[cP_n^m + dQ_n^m\right]\left[-e\sin m\phi + f\cos m\phi\right] \tag{3.14}$$

$$H_r = 0 \tag{3.15}$$

$$H_\theta = \frac{1}{r\sin\theta} m\left[aJ_n + bY_n\right]\left[cP_n^m + dQ_n^m\right]\left[-e\sin m\phi + f\cos m\phi\right] \tag{3.16}$$

$$H_\phi = \frac{1}{r}\sin\theta\left[aJ_n + bY_n\right]\left[cP_n^{m\prime} + dQ_n^{m\prime}\right]\left[e\cos m\phi + f\sin m\phi\right] \tag{3.17}$$

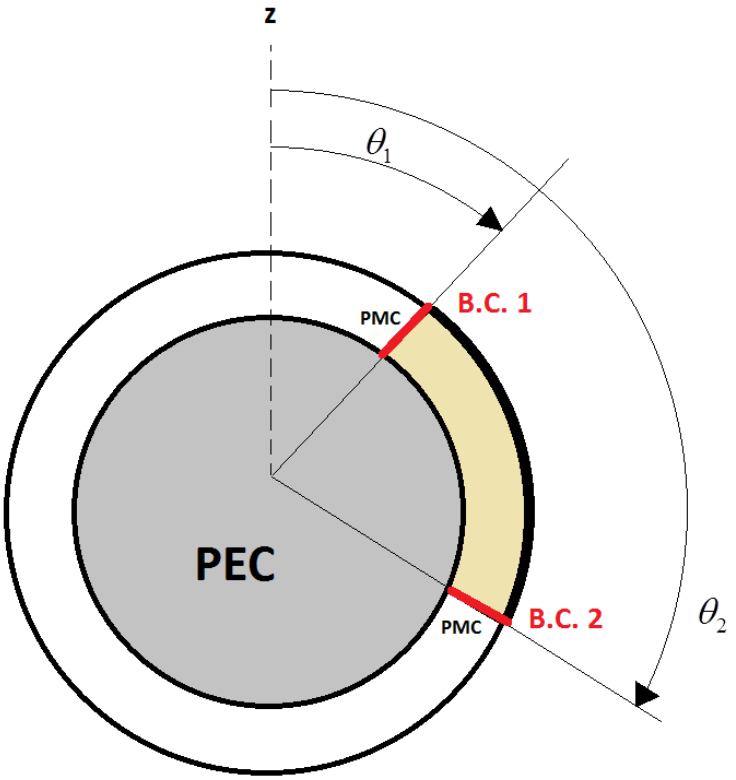

Figure 3.3: Boundary conditions for PMC side walls at $\theta=\theta_1$ and $\theta=\theta_2$

The coefficients of associated Legendre functions are determined by applying boundary conditions on H_ϕ at $\theta=\theta_1$ and $\theta=\theta_2$ as depicted in Figure 3.3.

Only the θ dependent part of (3.5) is considered to formulate the first part of solution for the sake of simplicity:

$$B(\theta) = cP_n^m(\cos\theta) + dQ_n^m(\cos\theta) \tag{3.18}$$

$$H_{\phi}\Big|_{\theta=\theta_1} = -\sin\theta_1\left[cP_n^{m\prime}(\cos\theta_1) + dQ_n^{m\prime}(\cos\theta_1)\right] = 0 \tag{3.19}$$

$$H_{\phi}\Big|_{\theta=\theta_2} = -\sin\theta_2\left[cP_n^{m\prime}(\cos\theta_2) + dQ_n^{m\prime}(\cos\theta_2)\right] = 0 \tag{3.20}$$

The resulting expressions can be reformed such that a matrix with trivial solution is obtained:

$$\begin{bmatrix} -P_n^{m\prime}(\cos\theta_1)\sin\theta_1 & -Q_n^{m\prime}(\cos\theta_1)\sin\theta_1 \\ -P_n^{m\prime}(\cos\theta_2)\sin\theta_2 & -Q_n^{m\prime}(\cos\theta_2)\sin\theta_2 \end{bmatrix} \cdot \begin{bmatrix} c \\ d \end{bmatrix} = \begin{bmatrix} 0 \\ 0 \end{bmatrix} \tag{3.21}$$

The solution of the matrix equation (3.21) is dependent on two dummy variables *c* and *d*, therefore, one of these can be chosen arbitrarily and the other one takes its value accordingly. For simplicity, they are chosen as follows:

$$c = -\sin\theta_1\, Q_n^{m\prime}(\cos\theta_1) \tag{3.22}$$

$$d = \sin\theta_1 P_n^{m\prime}(\cos\theta_1) \tag{3.23}$$

As a result, the θ dependent part of the magnetic potential expression is explicitly written:

$$B(\theta) = -\sin\theta_1\left[P_n^m(\cos\theta)Q_n^{m\prime}(\cos\theta_1) - P_n^{m\prime}(\cos\theta_1)Q_n^m(\cos\theta)\right] \tag{3.24}$$

There is another equation that can be extracted from this solution process as well. If (3.19) and (3.20) are solved simultaneously, the resulting equation is derived as:

$$P_n^{m\prime}(\cos\theta_1)Q_n^{m\prime}(\cos\theta_2) = P_n^{m\prime}(\cos\theta_2)Q_n^{m\prime}(\cos\theta_1) \tag{3.25}$$

(3.25) is implicit in nature and cannot be sold thoroughly without numerical approach. It includes the information about the mode parameters that will be used to find mode frequencies and wave functions. Solution of this equation will be dis-

cussed in the following sections. Furthermore, as mentioned before, the (3.24) gives the θ dependent part of the wave function. In order to obtain total expression, the other two orthogonal parts must be evaluated as well.

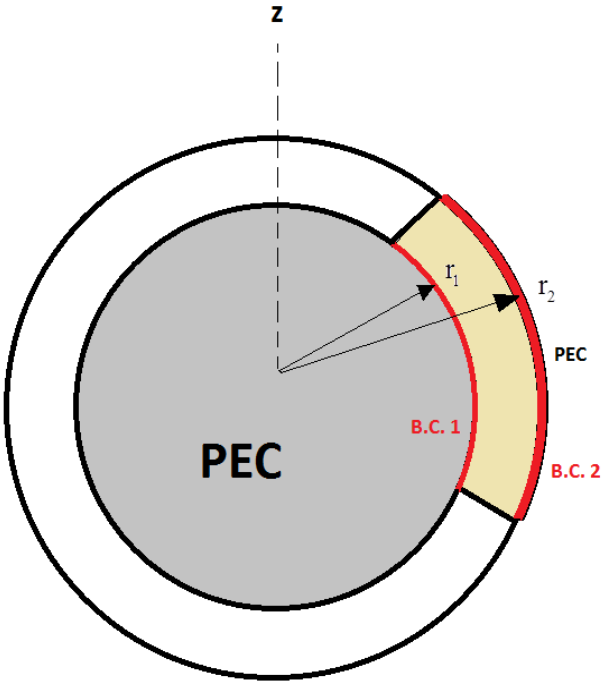

Figure 3.4: Boundary conditions for PEC top and bottom walls at $r = r_1$ and $r = r_2$

The coefficients of Bessel functions are determined by applying boundary conditions on E_ϕ at $r = r_1$ and $r = r_2$ as depicted in Figure 3.4. Next step is to derive the r dependent part of the (3.5).

$$A(r) = a\hat{J}_n(k_d r) + b\hat{Y}_n(k_d r) \tag{3.26}$$

$$E_\phi\Big|_{r=r_1} = k_d\left[a\hat{J}_n'(k_d r_1) + b\hat{Y}_n'(k_d r_1)\right] = 0 \tag{3.27}$$

$$E_\phi\Big|_{r=r_2} = k_d\left[a\hat{J}_n'(k_d r_2) + b\hat{Y}_n'(k_d r_2)\right] = 0 \tag{3.28}$$

The resulting expressions can again be reformed such that a matrix with trivial solution is obtained:

$$\begin{bmatrix} k_d \hat{J}_n{}'(k_d r_1) & k_d \hat{Y}_n{}'(k_d r_1) \\ k_d \hat{J}_n{}'(k_d r_2) & k_d \hat{Y}_n{}'(k_d r_2) \end{bmatrix} \cdot \begin{bmatrix} a \\ b \end{bmatrix} = \begin{bmatrix} 0 \\ 0 \end{bmatrix} \tag{3.29}$$

Then, the solution of the matrix equation (3.29) is dependent on two dummy variables *a* and *b*, therefore, one of these can be chosen arbitrarily and the other one takes its value accordingly. For simplicity, they are chosen as follows:

$$a = k_d \hat{Y}_n{}'(k_d r_1) \tag{3.30}$$

$$b = -k_d \hat{J}_n{}'(k_d r_1) \tag{3.31}$$

Consequently, the *r* dependent part of the magnetic potential expression is explicitly written as:

$$A(r) = k_d \left[\hat{J}_n(k_d r) \hat{Y}_n{}'(k_d r_1) - \hat{J}_n{}'(k_d r_1) \hat{Y}_n(k_d r) \right] \tag{3.32}$$

The other equation that can be extracted from this solution process is obtained if (3.27) and (3.28) are solved simultaneously. The resulting equation is then given as:

$$\hat{J}_n{}'(k_d r_1) \hat{Y}_n{}'(k_d r_2) = \hat{J}_n{}'(k_d r_2) \hat{Y}_n{}'(k_d r_1) \tag{3.33}$$

(3.33) is also implicit in nature like (3.25) and cannot be solved thoroughly without numerical approach. Again, the solution of this equation will be considered in the following sections. Finally, the (3.34) gives the ϕ dependent part of the wave function. In order to obtain total expression, the last orthogonal part must be derived.

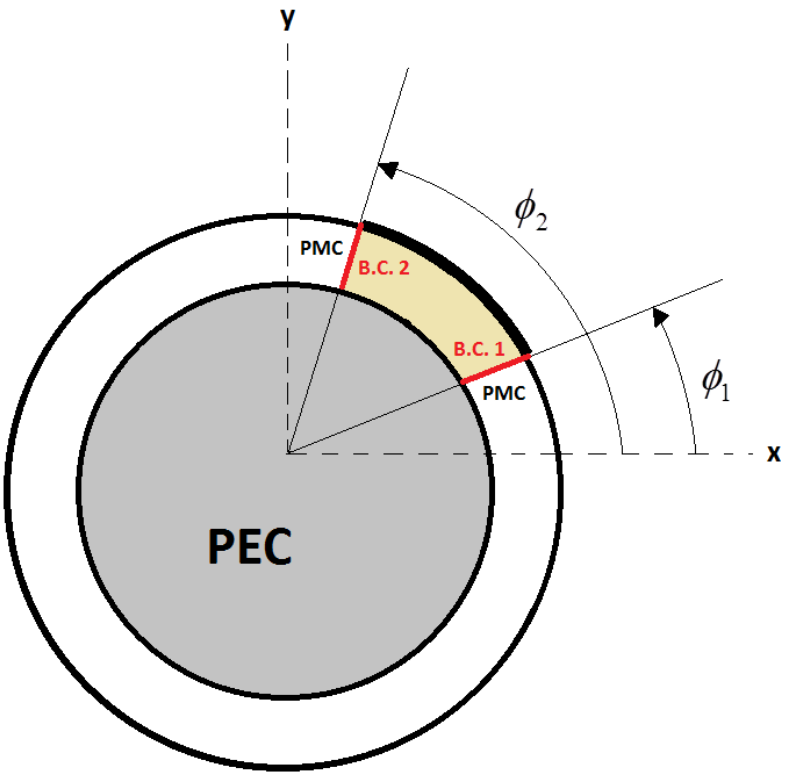

Figure 3.5: Boundary conditions for PMC side walls at $\phi=\phi_1$ and $\phi=\phi_2$

The coefficients of sinusoidal functions of (3.5) are determined by applying boundary conditions on H_θ at $\phi=\phi_1$ and $\phi=\phi_2$ as depicted in Figure 3.5.

$$C(\phi) = e\cos m\phi + f\sin m\phi \tag{3.34}$$

$$H_\theta\big|_{\phi=\phi_1} = -e\,m\sin m\phi_1 + f\,m\sin m\phi_1 = 0 \tag{3.35}$$

$$H_\theta\big|_{\phi=\phi_2} = -e\,m\cos m\phi_2 + f\,m\sin m\phi_2 = 0 \tag{3.36}$$

The resulting expressions can again be reformed such that a matrix with trivial solution is obtained:

$$\begin{bmatrix} -m\sin m\phi_1 & m\cos m\phi_1 \\ -m\sin m\phi_2 & m\cos m\phi_2 \end{bmatrix} \cdot \begin{bmatrix} e \\ f \end{bmatrix} = \begin{bmatrix} 0 \\ 0 \end{bmatrix} \tag{3.37}$$

Then, the solution of the matrix equation (3.37) is dependent on two dummy variables *c* and *d*, therefore, one of these can be chosen arbitrarily and the other one takes its value accordingly. For simplicity, they are chosen as follows:

$$e = m\cos m\phi_1 \tag{3.38}$$

$$f = -m\sin m\phi_1 \tag{3.39}$$

Consequently, the ϕ dependent part of the magnetic potential expression is explicitly written as:

$$C(\phi) = \cos m\phi_1 \cos m\phi - \sin m\phi_1 \sin m\phi \tag{3.40}$$

The other equation that can be extracted from this solution process is obtained if (3.35) and (3.36) are solved simultaneously. The resulting equation is then given as:

$$\sin m\phi_1 \cos m\phi_2 = \sin m\phi_2 \cos m\phi_1 \tag{3.41}$$

By utilizing trigonometric identities, (3.40) and (3.41) are reformed to the equations below:

$$C(\phi) = \cos\left[m(\phi - \phi_1)\right] \tag{3.42}$$

$$\sin\left[m(\phi_2 - \phi_1)\right] = \sin(m\,\Delta\phi) = 0 \tag{3.43}$$

then,

$$m = \frac{p\,\pi}{\Delta\phi} \qquad , \qquad p = 0,1,2,3,..... \tag{3.44}$$

Unlike others, (3.44) is explicit and, therefore it is the starting point of mode finding process. (3.40) gives the ϕ dependent part of the wave function. Finally, as all the unknown coefficients are eliminated, the total expression for the wave function is given in (3.45):

$$\psi_{mn} = -k_d \sin\theta_1 \left[\hat{J}_n(k_d r)\hat{Y}_n'(k_d r_1) - \hat{J}_n'(k_d r_1)\hat{Y}_n(k_d r) \right] \cdot \left[P_n^m(\cos\theta) Q_n^{m\prime}(\cos\theta_1) - P_n^{m\prime}(\cos\theta_1) Q_n^m(\cos\theta) \right] \cos[m(\phi - \phi_1)] \tag{3.45}$$

The parameters in (3.45) such as *m*, *n* and k_d are calculated by solving the transcendental equations that were obtained in the solution process [57]. To summarize the process, the equations to be solved for mode parameters can be listed again as follows:

$$m = \frac{p\,\pi}{\Delta\phi} \qquad , \qquad p = 0,1,2,3,..... \tag{3.46}$$

$$P_n^{m\prime}(\cos\theta_1) Q_n^{m\prime}(\cos\theta_2) = P_n^{m\prime}(\cos\theta_2) Q_n^{m\prime}(\cos\theta_1) \tag{3.47}$$

$$\hat{J}_n'(k_d r_1)\hat{Y}_n'(k_d r_2) = \hat{J}_n'(k_d r_2)\hat{Y}_n'(k_d r_1) \tag{3.48}$$

(3.47) and (3.48) are in closed form and thus it is quite difficult to construct an explicit solution for the parameters. Therefore, the parameters are calculated by a commercial software where a long sequence of values are inserted in the expressions and the precision of the equations are observed at each specific value. First, parameter *m* values are found from (3.46) and inserted to (3.47). Then, the parameter *n* values that satisfy the (3.47) are determined. Although there are infinitely many solutions for these parameters, only a few of them are generally enough to continue the analysis. Because, high order parameters refer to higher order spherical TM modes which have little to no effect on the fundamental mode operation. For each parameter *n* value obtained in (3.47), there are also infinitely many k_d parameters coming from (3.48). These parameters are propagation constant values of each mode existing inside cavity. Extraction of the resonance frequency of each mode from these constants once they are obtained is completely straightforward using (3.2).

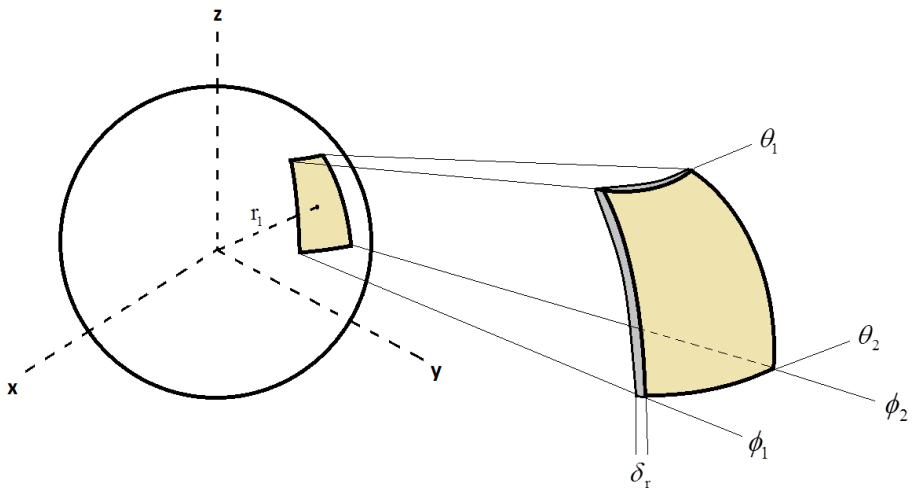

Figure 3.6: The spherical-rectangular patch geometry with parameters: r_1=0.1 m, ϕ_1=-π/12, ϕ_2=π/12, θ_1=2π/12, θ_2=5π/12, δ_r=4.5mm

The mode parameters that belong to an arbitrarily chosen geometry of spherical patch antenna as in Figure 3.6 are listed in Table 3.1. The groups of extracted parameters from equations (3.46) to (3.48) are listed according to the parameter orders. The fundamental frequency occupies the first row of the table along with the parameters belonging to it. As mentioned in the previous chapter, fundamental operation occurs when the half-wavelength of the signal is close to the largest dimension of the antenna; which, in this example, is the θ directed dimension of the patch. The length of the dimension is approximately 78.5 mm and the wavelength of the fundamental frequency (f = 0.92 GHz) is 157 mm according to the cavity analysis as given in Table 3.1. To sum up, the results from the analysis so far are in good agreement with the practical expectations.

Table 3.1: The resonant frequencies of the patch given in Figure 3.6

$p = 0$		
$n = 3.65$	$k_d = 40.34$ $f = 0.92$ GHz	$k_d = 699.2$ $f = 16.1$ GHz
$n = 7.58$	$k_d = 78.92$ $f = 1.81$ GHz	$k_d = 702.5$ $f = 16.2$ GHz
$p = 1$		
$n = 6.55$	$k_d = 68.79$ $f = 1.58$ GHz	$k_d = 701.51$ $f = 16.1$ GHz
$n = 9.12$	$k_d = 94.07$ $f = 2.16$ GHz	$k_d = 704.44$ $f = 16.2$ GHz

Considering the resonant frequencies of modes of the cavity given in Table 3.1, it is notable that their wavelength values are almost directly proportional to the multiples of patch dimensions. Even though, the method applied so far gives correct numerical results for the resonant frequencies of the modes, the excitation of these modes have not yet been considered. A spherical patch antenna of such simple geometry can be excited to radiate at any desired mode frequency if the appropriate excitation is employed. The requirements for an accurate excitation in terms of positioning and alignment were discussed in the previous chapter for planar patch structures. The same necessities apply to the spherical patch antennas as well, thus the excitation methods and their analysis will not be detailed here. For the following analysis of wave function, micro-strip line type feed is assumed unless otherwise specified.

The feed mechanism determines the current and voltage distribution on the patch surface and the fields inside cavity take shape accordingly. As mentioned in the previous chapter, the wave function is affected by these excitation currents. The expression for the final wave function, or magnetic vector potential in other words, is determined by summing the orthogonal magnetic potentials of the cavity modes which can be referred to as modal expansion. Magnetic potentials of each mode have a co-

efficient that can be basically evaluated by taking the inner product of the wave function and the excitation respectively [51].

$$\psi = \sum_{d} M_d \psi_d \tag{3.49}$$

$$M_d = \frac{\mu}{k_d^2 - k^2} \frac{\left\langle J, \psi_d^* \right\rangle}{\left\langle \psi_d, \psi_d^* \right\rangle} \tag{3.50}$$

where

$$\left\langle J, \psi_d^* \right\rangle = \int_s J \, \psi_d^* \, ds \tag{3.51}$$

$$\left\langle \psi_d, \psi_d^* \right\rangle = \int_v \psi_d \, \psi_d^* \, dv \tag{3.52}$$

such that Ψ_d represents the wave functions of modes listed in Table 3.1 and M_d is the coefficients of each mode contributing to the total wave function Ψ.

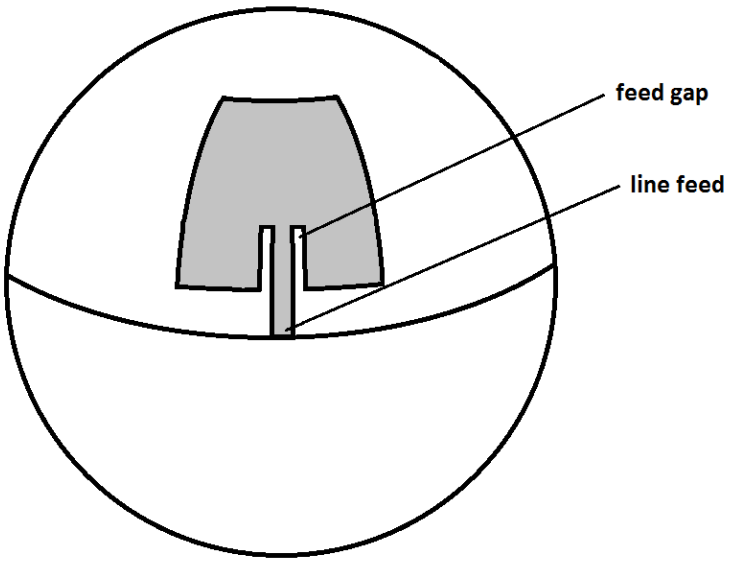

Figure 3.7: A spherical-rectangular patch antenna with a line feed

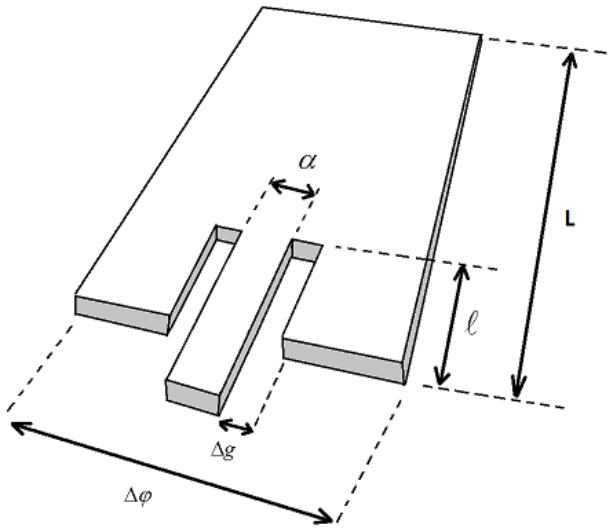

Figure 3.8: Detailed dimension description of a spherical-rectangular patch with a line feed

The orthogonal wave function coefficients are highly dependent on the geometry of the patch and feed structure. This dependence can be observed in (3.51) and (3.52) where volume and surface integration is applied. Figure 3.7 and Figure 3.8 depict a spherical patch antenna excited with a micro-strip line. The integration domains of the mentioned equations are clearly noticeable in the latter figure.

The term k_d^2 - k^2 in the denominator of (3.50) is the main factor in determining the strength of each modal coefficient. The wave number k_d of fundamental mode is evaluated at the fundamental frequency. As the wave number k is dependent on frequency of operation, the coefficient of the fundamental mode rises to infinity for lossless dielectric assumption. Therefore, it can be mistakenly deduced that this analytical solution for finding the contribution of the high order modes is unnecessary and their coefficients will be finite and negligible at the fundamental frequency operation. Nevertheless, it is not enough to solve the homogeneous Helmholtz equation without considering the feed effect since dielectric has its loss mechanism in reality and the loss tangent parameter must be included in the analysis. Therefore, it is necessary to refer to the previous chapter where this analysis step is explained in detail. On the other hand, as the following analytical solution steps will prove, the modal coefficients of magnetic vector potentials of higher modes are less effective on the

normalized radiation pattern compared to the fundamental mode and their calculation may be ignored if very high accuracy is required. Another point is that the modal coefficients are quite significant if the input impedance of the patch antenna is considered. The coefficients are determined at a large frequency interval around the frequency of operation. Therefore, it is possible to have comparable values for the magnetic vector potential coefficients at each sample frequency. Evaluating the fields at these sample frequencies and making the calculations for input impedance can give an accurate insight to the matching status of the feed to the microstrip patch even though it introduces extra effort to the analytical computation. However, it is avoidable if normalized radiation pattern is the purpose of a study. In this study, only the radiation pattern characteristic analysis is conducted for certain spherical rectangular patch antennas.

The total magnetic vector potential expression obtained in (3.49) includes both geometrical properties of the patch antenna and the feed effect. In order to continue to the cavity analysis, electric field confined under the spherical patch must be found by utilizing this magnetic potential.

3.3.1. Electric Fields Inside Cavity:

The radiation of the patch antenna is caused by the equivalent magnetic current vectors at the edges of the patch. These magnetic currents originate from the electric fields present under the patch and fringing fields at the edges as mentioned in the previous chapter. Same rules apply to the spherical patch antennas.

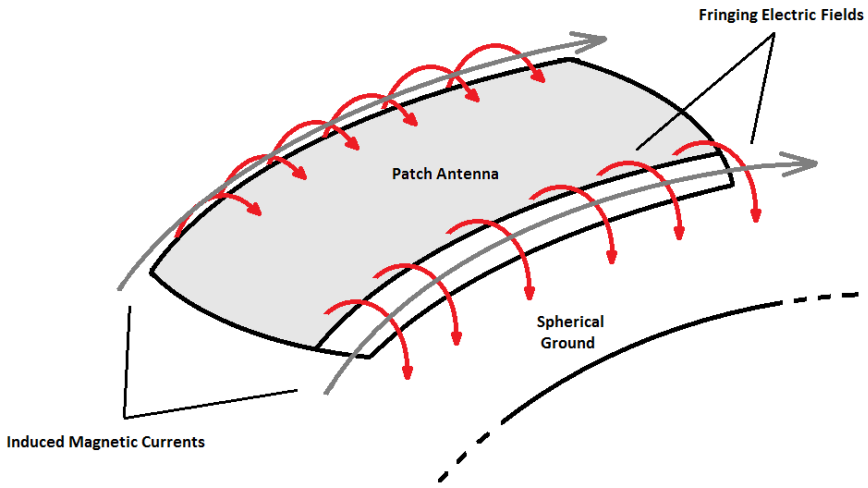

Figure 3.9: Fringing electrical fields and the induced magnetic currents

The Figure 3.9 depicts the trend of the fields close to the edges of patch structure. These fields follow a semicircular path in the air and the dielectric outside the patch and this behavior of the electric fields causes magnetic currents in the center of their locus. As a result, the patch radiation occurs.

Although the fringing fields are the true nature of the radiation concept of the patch antennas, cavity method analysis does not include such behavior in the formulation. Instead, regarding the radially directed fields inside the cavity to evaluate the equivalent magnetic currents is enough to model the behavior of the antenna.

The radially directed electric fields inside the cavity can be determined by using (3.53).

$$E_r = \frac{1}{j\omega\varepsilon}\left(\frac{\partial^2}{\partial r^2} + k^2\right)\psi_A = \frac{1}{j\omega\varepsilon}\frac{\partial^2\psi_A}{\partial r^2} + \frac{1}{j\omega\varepsilon}k^2\,\psi_A \tag{3.53}$$

where

$$\psi_A = -k_d \sin\theta_1\, \hat{A}(r)\, B(\theta) C(\phi) \tag{3.54}$$

The (3.53) requires that the second order radial derivatives ∂^2/∂_r^2 of the Bessel functions $\hat{A}(r)$ in (3.54) are evaluated. Since Bessel functions are highly oscillatory functions, their second order derivatives can introduce error into the results if numerical derivation is preferred. Another way to evaluate the derivatives is making use of an identity of the Schelkunoff type Bessel functions. The expression can be simplified to eliminate derivation using the (3.55) as in [49]:

$$\left[\frac{d^2}{dr^2}+k^2-\frac{n(n+1)}{r^2}\right]\hat{A}_n=0 \tag{3.55}$$

then

$$\left(\frac{\partial^2}{\partial r^2}+k^2\right)\hat{A}_n=\frac{n(n+1)}{r^2}\hat{A}_n \tag{3.56}$$

substituting (3.56) into (3.53) yields

$$E_r=j\eta_d\frac{n(n+1)}{r^2}\sin\theta_1\,\hat{A}(r)B(\theta)C(\phi) \tag{3.57}$$

The electric fields inside cavity are subjected to the boundary conditions at each PMC side walls of the cavity. Application of boundary conditions will give equivalent magnetic currents at the edges of the path which cause radiation.

3.3.2. Equivalent Magnetic Currents:

The dominating radially directed electric fields were derived as (3.57). In order to find the radiated fields, equivalent magnetic currents must be found using the following equation at each PMC side wall of the cavity:

$$\vec{M}_{eq}=\int_{r_1}^{r_2}\hat{n}\times\vec{E}_r\,dr\Big|_{PMC\,walls} \tag{3.58}$$

At this point, it is necessary to note that the magnetic currents determined at each side wall are not necessarily radiating. Because, depending on the mode of operation, the magnetic current distributions are strictly related to electric field distribution inside the cavity. As mentioned in previous chapters, the radiation of fundamental mode occurs if the largest dimension of the patch is half of the wavelength of operation frequency. This is because of the electric field distribution of the fundamental mode.

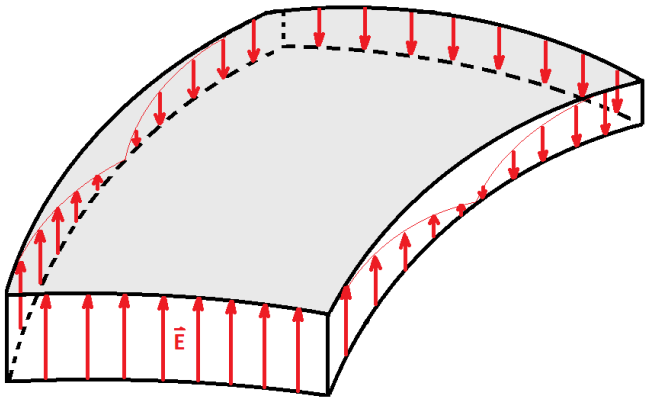

Figure 3.10: E-field distribution of the fundamental mode TM_{01}

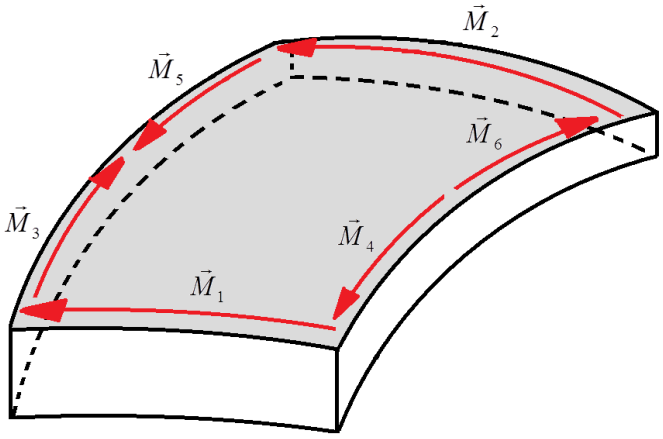

Figure 3.11: Equivalent magnetic current distribution on the patch for the fundamental mode TM_{01}

The electric field distribution of the fundamental mode inside spherical cavity is indicated in Figure 3.10. When this distribution is considered together with the (3.58),

it is not difficult to recognize that the equivalent magnetic current vectors at the side walls can be in different directions. This phenomenon is also observable in Figure 3.11. The currents at the left and right sides of the patch $\vec{M}_3$ to $\vec{M}_6$ are in opposite directions whereas the ones at the top and bottom $\vec{M}_1$ and $\vec{M}_2$ are in same directions. This opposite current case occurs on the sides with larger dimensions. Therefore, their contribution to the radiation of the antenna is almost completely ignorable. The other two sides have parallel magnetic currents and they are the reason for the radiation of the antenna. It is necessary to mark that this phenomenon is valid for basic shaped antennas such as rectangular patch. Patches with complex geometries must be analyzed more thoroughly.

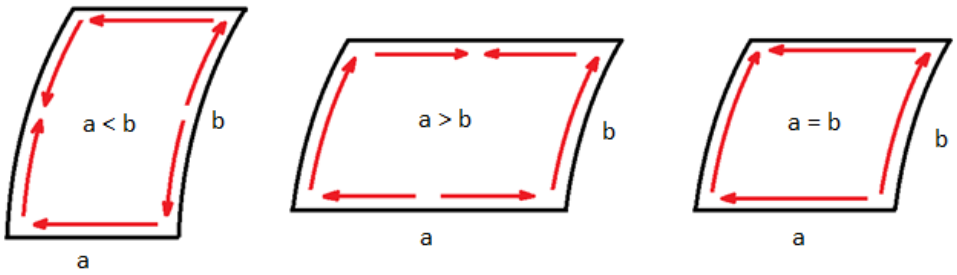

Figure 3.12: Equivalent magnetic current distribution for different patch dimensions

The equivalent magnetic currents on each side of the wall are all effectively radiating if patch has a quasi-square geometry. In this case, the current vectors are in parallel directions with the ones at opposite sides and they do not cancel each other as seen in Figure 3.12. This occurs because two modes are concentric at the same fundamental frequency.

Since the equivalent magnetic currents are derived using the cavity model theory, it is now possible to find the corresponding radiation fields. In planar patch case, the radiating fields are easily evaluated using image theory and unbounded radiation concept. Because, the ground plane can be assumed to be infinitely long which makes the solution relatively simpler. Nevertheless, this procedure cannot be followed due to the finite dimension sphere. Neither the ground is planar nor is it infi-

nitely long. Therefore, magnetic currents found by (3.58) must be utilized using another approach. The spherical Helmholtz equation outside the sphere can be satisfied by the vector potentials which are expressed in terms of spherical harmonics [45]. The summation of these harmonics gives the total vector potentials. Then, the far-fields related to these vector potentials are derived. As a result, the radiation expression of equivalent magnetic currents in the presence of the finite sized conducting sphere can be evaluated analytically.

3.3.3. Spherical Wave Harmonics Approach:

The problem of electromagnetic radiation caused by magnetic current elements close to the surface of a conducting sphere can be solved efficiently by employing spherical harmonics method. The spherical structure is divided into layers and magnetic and electric potentials at each layer are represented by infinitely many spherical harmonics with suitable coefficients. The types of these harmonics are strictly based on the geometry of the sphere and the layers of interest. Because the aim is that the proposed harmonic expressions must be finite and convergent at any point in the space.

In order to find the electric and magnetic potentials, the spherical functions that form the harmonics must be determined. The harmonic expressions consist of ϕ, θ and r dependent spherical functions. The type of these functions is selected depending on the spherical structure. Figure 3.13 indicates the type of spherical structures and their corresponding spherical functions for travelling waves. Since the evaluation of radiated fields will be the next step, the accurate choice of these harmonic types has an essential role in the progress [48].

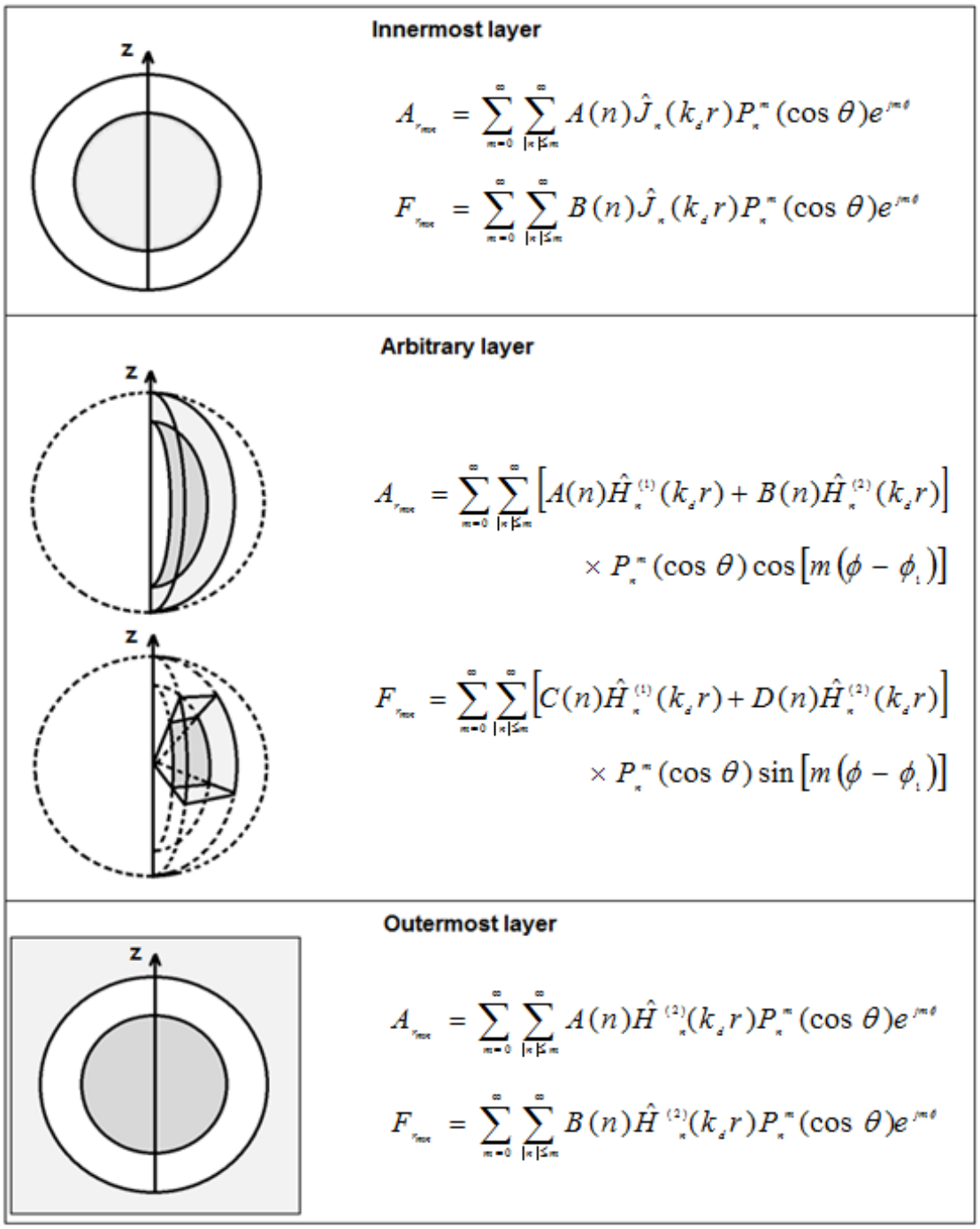

Figure 3.13: Spherical wave harmonic expressions for different layers

Considering the information given in the Figure 3.13, the harmonic expression for the problem discussed in this study, which is the radiation in the existence of a closed conducting sphere, can be written as follows:

$$A_{r_1} = \sum_{n=1}^{\infty} \sum_{m=-n}^{n} \left[A(n) \hat{H}_n^{(1)}(k_0 r) + B(n) \hat{H}_n^{(2)}(k_0 r) \right] P_n^{|m|}(\cos\theta)\, e^{jm\phi} \tag{3.59}$$

$$F_{r_1} = \sum_{n=1}^{\infty} \sum_{m=-n}^{n} \left[C(n) \hat{H}_n^{(1)}(k_0 r) + D(n) \hat{H}_n^{(2)}(k_0 r) \right] P_n^{|m|}(\cos\theta)\, e^{jm\phi} \tag{3.60}$$

These potentials exist at the inner region which is between patch and the sphere. It should be noted that the free-space wavenumbers are inserted into the equations since the contribution of the dielectric was included in the cavity field analysis before. The dielectric is removed at this point of the procedure. In addition, for outer region which is outside the patch, equations can be written as:

$$A_{r_2} = \sum_{n=1}^{\infty} \sum_{m=-n}^{n} E(n) \hat{H}_n^{(2)}(k_0 r) P_n^{|m|}(\cos\theta)\, e^{jm\phi} \tag{3.61}$$

$$F_{r_2} = \sum_{n=1}^{\infty} \sum_{m=-n}^{n} F(n) \hat{H}_n^{(2)}(k_0 r) P_n^{|m|}(\cos\theta)\, e^{jm\phi} \tag{3.62}$$

The equations (3.59) and (3.60) represent the harmonics that exist inside dielectric layer. Legendre and exponential functions are due to the closed nature of the sphere. The Schelkunoff Hankel functions of first and second kinds are required to model the behavior of the waves inside the dielectric layer. Inward and outward travelling waves exist at the same time at this layer because there are reflections at the air-dielectric boundary. Likewise, (3.61) and (3.62) represent the wave harmonics existing outside the sphere in the air. This outermost layer hosts only outward travelling waves, thus the second type of Hankel functions is preferred.

The solution procedure requires that the coefficients of spherical harmonics in the derived magnetic and current potentials to be determined. In order to obtain the coefficients *A(n), B(n), C(n), D(n), E(n), F(n)* in the equations (3.59) to (3.62), the boundary conditions in the structure must be utilized. However, it is necessary to note that the obtained field and current vectors are all in spatial domain. As a result, the boundary condition equations derived from these spatial fields and currents will have to be satisfied in every single point in space. This approach completely fails

even if the boundary conditions are forced on a group of arbitrarily chosen points on boundary surfaces because such an attempt results in large scaled matrices and strongly ill-conditioned solution matrix. Although there are some methods to improve the matrix condition in such cases at the cost of accuracy of the result, the solution remains highly unstable. A small change in the problem parameters produces significant changes in the final result.

A more reliable approach to force the boundary conditions on the fields derived so far is the spectral domain method. The fields and currents can be transferred to the spectral domain and operations can be made here. In this domain, the point matching of boundary conditions over the surfaces of sphere is not necessary in contrast to spatial domain approach. Therefore, it is a more preferable procedure to simplify the analytical complexity and to attain a result with high stability.

3.3.4. Spectral Domain Approach:

Spectral domain approach is a well-known solution procedure widely preferred for electromagnetic problems where spatial domain approach is not practical for application. Even though spatial domain gives more insight on the procedure, it is coordinate-dependent nature increases the complexity of the solution. On the other hand, spectral domain is easier to employ and coordinate independent to some extent. In fact, expressions in spectral domain for spherical coordinate systems have only radial direction dependence along with the frequency making this approach attractive in problems with complex spatial nature.

The application of the spectral domain method is limited by the geometry of the structure of interest. As mentioned before, the spectral expressions in spherical coordinate systems have radial dependence. Therefore, the layers of the spherical structure must be homogeneous in θ and ϕ directions [46] as also depicted in the Figure 3.14c. Otherwise, the spectral expressions of fields and currents in this domain become inaccurate and the solution fails.

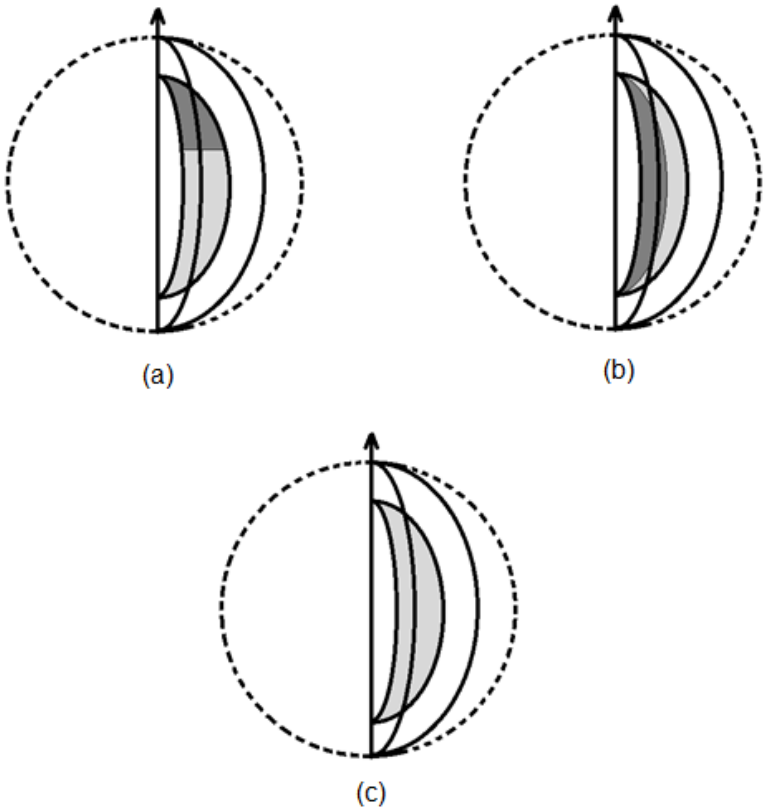

Figure 3.14: Patch antenna structures with different dielectric substrate alignments: a) Discontinuity in θ direction, b) Discontinuity in ϕ direction, c) Continuity in θ and ϕ direction

The problem of interest in this work is the radiation behaviors of patch antennas only on simple closed spherical structure surfaces; therefore, discontinuous-substrate antennas and spheres some of which are indicated in Figure 3.14 are out of scope of this thesis work.

In order to utilize the aforementioned spherical harmonics method, the current elements and fields must be written in spectral domain which can be easily accomplished by using Vector-Legendre transform. This transformation is the essential part in the spectral domain operations and provides significant opportunity to utilize boundary conditions on the fields radiated.

3.3.5. Vector-Legendre Transformation:

The operations in spectral domain in many cases can be implemented more efficiently in the spectral domain. However, all spatial vector elements must be transformed to spectral domain by means of Vector-Legendre transformation [56]. The transformation is applied by taking the Fourier transform of spatial vectors and normalizing them by a particular term depending on their harmonic number which is shown in (3.63):

$$\tilde{X}(r,n)=\begin{bmatrix}\tilde{X}_r\\ \tilde{X}_\theta\\ \tilde{X}_\phi\end{bmatrix}=\frac{1}{2\pi.S(n,m)}\int_0^{2\pi}\int_0^{\pi}\bar{\bar{L}}(n,m,\theta)\,X(r,\theta,\phi)\sin\theta\, e^{-jm\phi}d\theta\,d\phi \tag{3.63}$$

and the inverse transform is:

$$X(r,\theta,\phi)=\sum_{n=1}^{\infty}\sum_{m=-n}^{n}\bar{\bar{L}}(n,m,\theta)\,\tilde{X}(r,n)e^{jm\phi} \tag{3.64}$$

where X is either current vector or field vector. Also,

$$\bar{\bar{L}}(n,m,\theta)=\begin{bmatrix}L_{rr} & 0 & 0\\ 0 & L_{\theta\theta} & L_{\theta\phi}\\ 0 & L_{\phi\theta} & L_{\phi\phi}\end{bmatrix} \tag{3.65}$$

where

$$L_{rr}=P_n^{|m|}(\cos\theta)\sqrt{n(n+1)} \tag{3.66}$$

$$L_{\theta\theta}=\frac{\partial P_n^{|m|}(\cos\theta)}{\partial\theta} \tag{3.67}$$

$$L_{\theta\phi} = \frac{-jmP_n^{|m|}(\cos\theta)}{\sin\theta} \tag{3.68}$$

$$L_{\phi\theta} = \frac{jmP_n^{|m|}(\cos\theta)}{\sin\theta} \tag{3.69}$$

$$L_{\phi\phi} = \frac{\partial P_n^{|m|}(\cos\theta)}{\partial\theta} \tag{3.70}$$

lastly, the normalization factor is given by:

$$S(n,m) = \frac{2n(n+1)(n+|m|)!}{(2n+1)(n-|m|)!} \tag{3.71}$$

The parameters *n* and *m* define the corresponding number of each spherical harmonic. The transformation equations given in (3.63) and (3.64) are applicable to spherical closed structures only. The transformation expressions for spherical sector structures can be found in [47].

As the implied in the equations, the spectral components are dependent on wave number and radial distance from the center of the sphere. The ϕ and θ dependent terms are eliminated; therefore, this allows the problem to become sufficiently simple so that boundary conditions can be applied easily.

3.3.6. Application of Spectral Domain Method:

The radiation characteristics of spherical rectangular antennas can be derived by using spherical harmonics and applying boundary conditions in the spectral domain. The spherical harmonic types differ with respect to the layer of interest. In Figure 3.15, there are two layers which are below and above the infinitely thin microstrip patch antenna. The choice of spherical harmonic expressions was discussed in previ-

ous sections and it was decided that (3.59) and (3.60) are suitable for inner region and (3.61) and (3.62) are appropriate for the outer region.

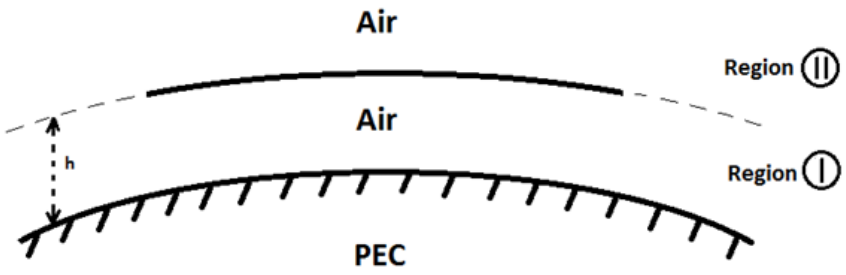

Figure 3.15: The cross section of spherical-rectangular antenna and the regions of interest

The boundary conditions are applied on the electric and magnetic fields, therefore (3.6) to (3.11) must be used to derive the fields from the potential expressions given in (3.59) to (3.62). Then, the field expressions for the inner region are as follows:

$$E_{\theta_1} = e^{jm\phi}\sum_{n=1}^{\infty}\sum_{m=-n}^{n} -\frac{jm}{r\sin\theta}\left(C(n)\hat{H}_n^{(1)}(k_o r)+D(n)\hat{H}_n^{(2)}(k_o r)\right)P_n^m(\cos\theta) + \frac{k_0}{j\omega\varepsilon_0 r}\left(A(n)\hat{H}_n^{(1)'}(k_o r)+B(n)\hat{H}_n^{(2)'}(k_o r)\right)\frac{\partial P_n^m(\cos\theta)}{\partial\theta} \quad (3.72)$$

$$E_{\phi_1} = e^{jm\phi}\sum_{n=1}^{\infty}\sum_{m=-n}^{n} \frac{1}{r}\left(C(n)\hat{H}_n^{(1)}(k_o r)+D(n)\hat{H}_n^{(2)}(k_o r)\right)\frac{\partial P_n^m(\cos\theta)}{\partial\theta} + \frac{mk_0}{\omega\varepsilon_0 r\sin\theta}\left(A(n)\hat{H}_n^{(1)'}(k_o r)+B(n)\hat{H}_n^{(2)'}(k_o r)\right)P_n^m(\cos\theta) \quad (3.73)$$

$$H_{\theta_1} = e^{jm\phi}\sum_{n=1}^{\infty}\sum_{m=-n}^{n} \frac{jm}{r\sin\theta}\left(A(n)\hat{H}_n^{(1)}(k_o r)+B(n)\hat{H}_n^{(2)}(k_o r)\right)P_n^m(\cos\theta) + \frac{k_0}{j\omega\mu_0 r}\left(C(n)\hat{H}_n^{(1)'}(k_o r)+D(n)\hat{H}_n^{(2)'}(k_o r)\right)\frac{\partial P_n^m(\cos\theta)}{\partial\theta} \quad (3.74)$$

$$H_{\theta_1} = e^{jm\phi}\sum_{n=1}^{\infty}\sum_{m=-n}^{n} -\frac{1}{r}\left(A(n)\hat{H}_n^{(1)}(k_o r)+B(n)\hat{H}_n^{(2)}(k_o r)\right)\frac{\partial P_n^m(\cos\theta)}{\partial\theta} + \frac{mk_0}{\omega\mu_0 r\sin\theta}\left(C(n)\hat{H}_n^{(1)'}(k_o r)+D(n)\hat{H}_n^{(2)'}(k_o r)\right)P_n^m(\cos\theta) \quad (3.75)$$

and the fields in the outer layer are:

$$E_{\theta_2} = e^{jm\phi}\sum_{n=1}^{\infty}\sum_{m=-n}^{n} \; -\frac{jm}{r\sin\theta}F(n)\hat{H}_n^{(2)}(k_o r)\,P_n^m(\cos\theta) + \frac{k_0}{j\omega\varepsilon_0 r}E(n)\hat{H}_n^{(2)'}(k_o r)\frac{\partial P_n^m(\cos\theta)}{\partial\theta} \tag{3.76}$$

$$E_{\phi_2} = e^{jm\phi}\sum_{n=1}^{\infty}\sum_{m=-n}^{n} \; \frac{1}{r}F(n)\hat{H}_n^{(2)}(k_o r)\frac{\partial P_n^m(\cos\theta)}{\partial\theta} + \frac{mk_0}{\omega\varepsilon_0 r\sin\theta}E(n)\hat{H}_n^{(2)'}(k_o r)\,P_n^m(\cos\theta) \tag{3.77}$$

$$H_{\theta_2} = e^{jm\phi}\sum_{n=1}^{\infty}\sum_{m=-n}^{n} \; \frac{jm}{r\sin\theta}E(n)\hat{H}_n^{(2)}(k_o r)\,P_n^m(\cos\theta) + \frac{k_0}{j\omega\mu_0 r}F(n)\hat{H}_n^{(2)'}(k_o r)\frac{\partial P_n^m(\cos\theta)}{\partial\theta} \tag{3.78}$$

$$H_{\phi_2} = e^{jm\phi}\sum_{n=1}^{\infty}\sum_{m=-n}^{n} \; -\frac{1}{r}E(n)\hat{H}_n^{(2)}(k_o r)\frac{\partial P_n^m(\cos\theta)}{\partial\theta} + \frac{mk_0}{\omega\mu_0 r\sin\theta}F(n)\hat{H}_n^{(2)'}(k_o r)\,P_n^m(\cos\theta) \tag{3.79}$$

The derived field expressions are all in spatial format and they must be transferred to the spectral domain for smooth progression of the solution. The Vector-Legendre transformation given in (3.63) is employed on the fields for this purpose. The transformation matrix in the equation (3.65) requires that the field expressions must be in 3*x*1 matrix format. However, as the transformation in radial direction is not required for this particular case, the transformation matrix and the field or source matrices will be in the form as follows:

$$\overline{\overline{L}}(n,m,\theta) = \begin{bmatrix} L_{\theta\theta} & L_{\theta\phi} \\ L_{\phi\theta} & L_{\phi\phi} \end{bmatrix} \quad , \quad X(r,\theta,\phi) = \begin{bmatrix} X_\theta(r,\theta,\phi) \\ X_\phi(r,\theta,\phi) \end{bmatrix} \tag{3.80}$$

Applying the (3.63) on the (3.72)-(3.79) yields the spectral domain matrices:

$$\tilde{\tilde{E}}_1(r,n)=\begin{bmatrix}\tilde{\tilde{E}}_{1\theta}(r,n)\\ \tilde{\tilde{E}}_{1\phi}(r,n)\end{bmatrix}=\begin{bmatrix}\dfrac{k_0}{j\omega\varepsilon_0 r}\left[A(n)\hat{H}_n^{(1)'}(k_0r)+B(n)\hat{H}_n^{(2)'}(k_0r)\right]\\ \dfrac{1}{r}\left[C(n)\hat{H}_n^{(1)}(k_0r)+D(n)\hat{H}_n^{(2)}(k_0r)\right]\end{bmatrix} \tag{3.81}$$

$$\tilde{\tilde{H}}_1(r,n)=\begin{bmatrix}\tilde{\tilde{H}}_{1\theta}(r,n)\\ \tilde{\tilde{H}}_{1\phi}(r,n)\end{bmatrix}=\begin{bmatrix}\dfrac{k_0}{j\omega\mu_0 r}\left[C(n)\hat{H}_n^{(1)'}(k_0r)+D(n)\hat{H}_n^{(2)'}(k_0r)\right]\\ -\dfrac{1}{r}\left[A(n)\hat{H}_n^{(1)}(k_0r)+B(n)\hat{H}_n^{(2)}(k_0r)\right]\end{bmatrix} \tag{3.82}$$

for the inner layer; then, the matrices for the outer layer are:

$$\tilde{\tilde{E}}_2(r,n)=\begin{bmatrix}\tilde{\tilde{E}}_{2\theta}(r,n)\\ \tilde{\tilde{E}}_{2\phi}(r,n)\end{bmatrix}=\begin{bmatrix}\dfrac{k_0}{j\omega\varepsilon_0 r}E(n)\hat{H}_n^{(2)'}(k_0r)\\ \dfrac{1}{r}F(n)\hat{H}_n^{(2)}(k_0r)\end{bmatrix} \tag{3.83}$$

$$\tilde{\tilde{H}}_2(r,n)=\begin{bmatrix}\tilde{\tilde{H}}_{2\theta}(r,n)\\ \tilde{\tilde{H}}_{2\phi}(r,n)\end{bmatrix}=\begin{bmatrix}\dfrac{k_0}{j\omega\mu_0 r}F(n)\hat{H}_n^{(2)'}(k_0r)\\ -\dfrac{1}{r}E(n)\hat{H}_n^{(2)}(k_0r)\end{bmatrix} \tag{3.84}$$

The magnetic current densities obtained via cavity model do have θ and ϕ components. However, both of these currents may be dominant and effective on the shape of radiation pattern if dimensions of the patch antenna form a quasi-square structure as in Figure 3.12. Therefore, it is necessary to represent the current equation in a general format as:

$$M(\theta,\phi)=\begin{bmatrix} M_{\theta}(\theta,\phi) \\ M_{\phi}(\theta,\phi) \end{bmatrix}=\begin{bmatrix} M_{\theta_1}(\theta)\delta(\phi-\phi_1)+M_{\theta_2}(\theta)\delta(\phi-\phi_2) \\ M_{\phi_1}(\phi)\delta(\theta-\theta_1)+M_{\phi_2}(\phi)\delta(\theta-\theta_2) \end{bmatrix} \tag{3.85}$$

Consider a particular case in which the equivalent currents are dominant in the θ direction on relevant sides of the patch antenna:

$$M(\theta,\phi)=\begin{bmatrix} M_{\theta}(\theta,\phi) \\ M_{\phi}(\theta,\phi) \end{bmatrix}=\begin{bmatrix} M_{\theta_1}(\theta)\delta(\phi-\phi_1)+M_{\theta_2}(\theta)\delta(\phi-\phi_2) \\ 0 \end{bmatrix} \tag{3.86}$$

In (3.85), the parameters ϕ_1, ϕ_2 and θ_1, θ_2 are the dimensional borders of the patch in spherical coordinates. When (3.63) is applied to the current elements to transform it into the spectral domain, the following equation is obtained:

$$\tilde{M}(n)=\frac{1}{2\pi\, S(n,m)}\begin{bmatrix} \int_{\theta_1}^{\theta_2}\left[M_{\theta_1}(\theta)e^{-jm\phi_1}+M_{\theta_2}(\theta)e^{-jm\phi_2}\right]\dfrac{\partial P_n^m(\cos\theta)}{\partial\theta}\sin\theta\, d\theta \\ \int_{\theta_1}^{\theta_2}\left[M_{\theta_1}(\theta)e^{-jm\phi_1}+M_{\theta_2}(\theta)e^{-jm\phi_2}\right] jm\, P_n^m(\cos\theta)\, d\theta \end{bmatrix} \tag{3.87}$$

It is necessary to note that even though there is no spatial ϕ component of currents as in (3.86), the spectral domain currents include an azimuthal current due to the effect of the transformation matrix. In addition, these azimuthal components have effects on the result comparable to the other component; therefore, ignoring this term ensures the failure of the analysis.

Since all the necessary field and current expressions were transformed to the spectral format, boundary conditions can be forced to proceed. There are three conditions; one on the surface of conducting sphere and two others on the air-air boundary as depicted in Figure 3.16.

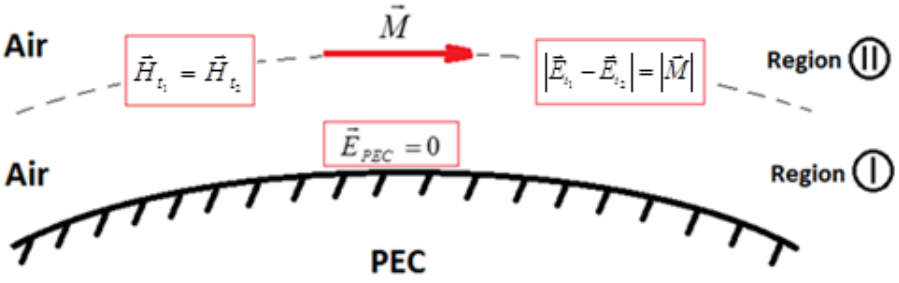

Figure 3.16: Spectral domain boundary conditions

and the boundary condition equations in spectral form are:

$$\hat{a}_r \times \tilde{\tilde{E}}_1 = 0 \qquad \text{(on the surface of conducting sphere, } r = \alpha\text{)} \qquad (3.88)$$

$$\hat{a}_r \times \left(\tilde{\tilde{H}}_2 - \tilde{\tilde{H}}_1\right) = 0 \qquad \text{(at the boundary of regions I and II, } r = b\text{)} \qquad (3.89)$$

$$\hat{a}_r \times \left(\tilde{\tilde{E}}_2 - \tilde{\tilde{E}}_1\right) = \tilde{\tilde{M}} \qquad \text{(at the boundary of regions I and II, } r = b\text{)} \qquad (3.90)$$

where the radius of the conducting sphere and the distance of the patch to center of the sphere are assumed to be α and b respectively. The purpose of applying these conditions is to eliminate the unknown coefficients existing in the spectral domain field expressions. There are six of these coefficients *A(n), B(n), C(n), D(n), E(n), F(n)* and the number of conditions is three where matrix elements are of size 2*x*1, generating six equations in total. Under these circumstances, all coefficients can be evaluated precisely.

The (3.88) determines the behavior of the electric field inside dielectric layer on conducting surfaces. Substituting (3.81) into (3.88) yields:

$$\tilde{\tilde{E}}_1\Big|_{r=a} = \begin{bmatrix} 0 \\ 0 \end{bmatrix} = \begin{bmatrix} \dfrac{k_0}{j\omega\varepsilon_0 r}\left[A(n)\hat{H}_n^{(1)'}(k_0 r) + B(n)\hat{H}_n^{(2)'}(k_0 r)\right] \\ \dfrac{1}{r}\left[C(n)\hat{H}_n^{(1)}(k_0 r) + D(n)\hat{H}_n^{(2)}(k_0 r)\right] \end{bmatrix}_{r=a} \qquad (3.91)$$

The solution of this equation (3.91) gives rise to the following expressions:

$$B(n) = -\frac{\hat{H}_n^{(1)'}(k_0 a)}{\hat{H}_n^{(2)'}(k_0 a)} A(n) \tag{3.92}$$

$$D(n) = -\frac{\hat{H}_n^{(1)}(k_0 a)}{\hat{H}_n^{(2)}(k_0 a)} C(n) \tag{3.93}$$

As indicated in (3.92) and (3.93), the unknowns *B(n)* and *D(n)* are eliminated at this step. The second boundary condition in (3.89) refers to the continuity of the tangential magnetic fields on the dielectric-dielectric boundaries. This condition can be fulfilled by substituting (3.82) and (3.84) into (3.89):

$$\tilde{H}_1\Big|_{r=b} = \tilde{H}_2\Big|_{r=b} \tag{3.94}$$

such that

$$\begin{bmatrix} \frac{k_0}{j\omega\mu_0 r}\left[C(n).\hat{H}_n^{(1)'}(k_0 r) + D(n).\hat{H}_n^{(2)'}(k_0 r)\right] \\ -\frac{1}{r}\left[A(n).\hat{H}_n^{(1)}(k_0 r) + B(n).\hat{H}_n^{(2)}(k_0 r)\right] \end{bmatrix}_{r=b} = \begin{bmatrix} \frac{k_0}{j\omega\mu_0 r} F(n).\hat{H}_n^{(2)'}(k_0 r) \\ -\frac{1}{r} E(n).\hat{H}_n^{(2)}(k_0 r) \end{bmatrix}_{r=b} \tag{3.95}$$

likewise, the solution of this equation results in the following relations:

$$C(n) = \frac{\hat{H}_n^{(2)}(k_0 a)\,\hat{H}_n^{(2)'}(k_0 b)}{\hat{H}_n^{(1)'}(k_0 b)\,\hat{H}_n^{(2)}(k_0 a) - \hat{H}_n^{(1)}(k_0 a)\,\hat{H}_n^{(2)'}(k_0 b)} F(n) \tag{3.96}$$

$$A(n) = \frac{\hat{H}_n^{(2)'}(k_0 a)\,\hat{H}_n^{(2)}(k_0 b)}{\hat{H}_n^{(1)}(k_0 b)\,\hat{H}_n^{(2)'}(k_0 a) - \hat{H}_n^{(1)'}(k_0 a)\,\hat{H}_n^{(2)}(k_0 b)} E(n) \tag{3.97}$$

After the elimination of unknowns *A(n)* and *C(n)*, third boundary condition is considered. The remaining unknowns are derived by making use of spectral current densities at this step. This boundary condition implies that the difference between tangential electric fields on each side of a dielectric-dielectric boundary is compensated by a magnetic current element on the border. It is significant to note that the thickness of the micro-strip patch antenna at this boundary is assumed to have an infinitely small thickness. The interpretation of (3.88) in terms of mathematical equations is as follows as stated in [41]:

$$\tilde{\tilde{M}}(n) = \begin{bmatrix} 0 & -1 \\ 1 & 0 \end{bmatrix} \left[\tilde{\tilde{E}}_2(n) - \tilde{\tilde{E}}_1(n) \right]_{r=b} \tag{3.98}$$

First evaluate the difference $\tilde{\tilde{E}}_2 - \tilde{\tilde{E}}_1$:

$$\tilde{\tilde{E}}_2 - \tilde{\tilde{E}}_1\Big|_{r=b} = \begin{bmatrix} \Delta\tilde{\tilde{E}}_\theta \\ \Delta\tilde{\tilde{E}}_\phi \end{bmatrix} = \begin{bmatrix} E(n)\left[\dfrac{k_0}{j\omega\varepsilon_0 b} \hat{H}_n^{(2)'}(k_0 a) \dfrac{\hat{H}_n^{(1)}(k_0 b)\hat{H}_n^{(2)'}(k_0 b) - \hat{H}_n^{(1)'}(k_0 b)\hat{H}_n^{(2)}(k_0 b)}{\hat{H}_n^{(1)}(k_0 b)\hat{H}_n^{(2)'}(k_0 a) - \hat{H}_n^{(1)'}(k_0 a)\hat{H}_n^{(2)}(k_0 b)} \right] \\ F(n)\left[\dfrac{1}{b} \hat{H}_n^{(2)}(k_0 a) \dfrac{\hat{H}_n^{(1)'}(k_0 b)\hat{H}_n^{(2)}(k_0 b) - \hat{H}_n^{(1)}(k_0 b)\hat{H}_n^{(2)'}(k_0 b)}{\hat{H}_n^{(1)'}(k_0 b)\hat{H}_n^{(2)}(k_0 a) - \hat{H}_n^{(1)}(k_0 a)\hat{H}_n^{(2)'}(k_0 b)} \right] \end{bmatrix} \tag{3.99}$$

Then, the final equations are obtained by substituting (3.99) in the equation below:

$$\tilde{\tilde{M}}(n) = \begin{bmatrix} M_\theta(n) \\ M_\phi(n) \end{bmatrix} = \begin{bmatrix} -\Delta E_\phi(n) \\ \Delta E_\theta(n) \end{bmatrix} \tag{3.100}$$

Since the current terms were founded before, the unknowns *E(n)* and *F(n)* can be determined by utilizing the (3.100). These coefficients are dependent on harmonic number n, therefore there are infinitely many coefficients and each one of these coefficients must be evaluated if the total solution is to be obtained. Nevertheless, the harmonics of higher orders become excessively small and are not effective on the field calculations. To conclude, sufficiently many harmonics are enough to continue with the analysis. At this point, all unknown coefficients were determined and the field expressions can now be clearly expressed.

3.3.7. Far-Field Radiation Pattern:

The expressions for electric and magnetic fields caused by magnetic currents on the spherical surface are given by (3.76) to (3.79) and the required steps to evaluate the unknown coefficients of these equations were discussed in the previous section. However, these field expressions are applicable to general distance problems and the concept of radiation pattern of an antenna is actually logical for fields at very large distances. Therefore, the electric and magnetic potential expressions in (3.61) and (3.62) must be adjusted accordingly.

The radial distance of fields from the antenna is the variable of Schelkunoff Hankel functions. This means that these special spherical functions must be revised and changed so that the true far field behavior of fields is observed. By making use of power series representation of Schelkunoff Bessel functions and taking the term $k_o r$ sufficiently large, the following approximations become accurate:

$$\hat{H}_n^{(2)}(k_0 r)\Big|_{r>>b} \cong j^{n+1}\, e^{-jk_0 r} \tag{3.101}$$

$$\hat{H}_n^{(2)'}(k_0 r)\Big|_{r>>b} \cong j^{n}\, e^{-jk_0 r} \tag{3.102}$$

Then the far-field expressions in (3.76) to (3.79) which are used for the radiation pattern applications become:

$$E_{\theta_2} = \frac{e^{j(m\phi - k_0 r)}}{r} \sum_{n=1}^{\infty} \sum_{m=-n}^{n} -\frac{j^{n+2} m}{\sin\theta} F(n) P_n^m(\cos\theta) + \frac{j^{n-1} k_0}{\omega\varepsilon_0} E(n) \frac{\partial P_n^m(\cos\theta)}{\partial\theta} \tag{3.103}$$

$$E_{\phi_2} = \frac{e^{j(m\phi - k_0 r)}}{r} \sum_{n=1}^{\infty} \sum_{m=-n}^{n} j^{n+1} F(n) \frac{\partial P_n^m(\cos\theta)}{\partial\theta} + \frac{j^{n} m k_0}{\omega\varepsilon_0 \sin\theta} E(n) P_n^m(\cos\theta) \tag{3.104}$$

$$H_{\theta_2} = \frac{e^{j(m\phi - k_0 r)}}{r} \sum_{n=1}^{\infty} \sum_{m=-n}^{n} \frac{j^{n+2} m}{\sin\theta} E(n) P_n^m(\cos\theta) + \frac{j^{n-1} k_0}{\omega\mu_0} F(n) \frac{\partial P_n^m(\cos\theta)}{\partial\theta} \tag{3.105}$$

$$H_{\phi_2} = \frac{e^{j(m\phi - k_0 r)}}{r} \sum_{n=1}^{\infty} \sum_{m=-n}^{n} -j^{n+1} E(n) \frac{\partial P_n^m(\cos\theta)}{\partial \theta} + \frac{j^n m k_0}{\omega \mu_0 \sin\theta} F(n) P_n^m(\cos\theta) \qquad (3.106)$$

The normalized radiation patterns can be observed by evaluating the total fields and normalizing them with respect to their maximum values and visualizing them in the logarithmic scale.

$$E_{tot} = \sqrt{\left|E_\theta\right|^2 + \left|E_\phi\right|^2} \qquad (3.107)$$

$$E_{norm,dB} = 20 \log_{10}\left(E_{tot} / \max\left(E_{tot}\right)\right) \qquad (3.108)$$

The radiation patterns of specific examples will be discussed in following chapters.

3.3.8. Input Impedance Calculation:

The calculation of input impedance for spherical patches is not very different from the planar patch case. The same concept mentioned in the previous chapter can be adapted to the spherical domain and applied accordingly. The radiated power and the dissipated power of the patch antenna are always equal to the power delivered by the feed network. The conservation of power can be summarized by the following equation:

$$\frac{\left|V\right|^2}{Z_{in}} = P_{rad} + P_m + P_e \qquad (3.109)$$

The radiated power is denoted by P_{rad}, dissipated electric and magnetic energies are P_e and P_m respectively. The voltage across the feeding point and the ground is calculated by taking the integral of the radial field inside the cavity:

$$V = \int_a^b E_r\Big|_{at\ feed} dr \qquad (3.110)$$

The input impedance of the antenna at a given frequency is then determined by utilizing (3.109) and (3.110). The resulting impedance value must be close to the impedance of the feeding network for an effective power transmission to the antenna so that the antenna radiation efficiency increases. Otherwise, the power delivered to antenna is stored in the imaginary impedance of the printed patch and radiated real power drops significantly. In this situation, making use of an inset-fed structure like in the planar case as depicted in the Figure 3.17 or changing the end-fed position helps in adjusting and matching the input impedance to the feed impedance.

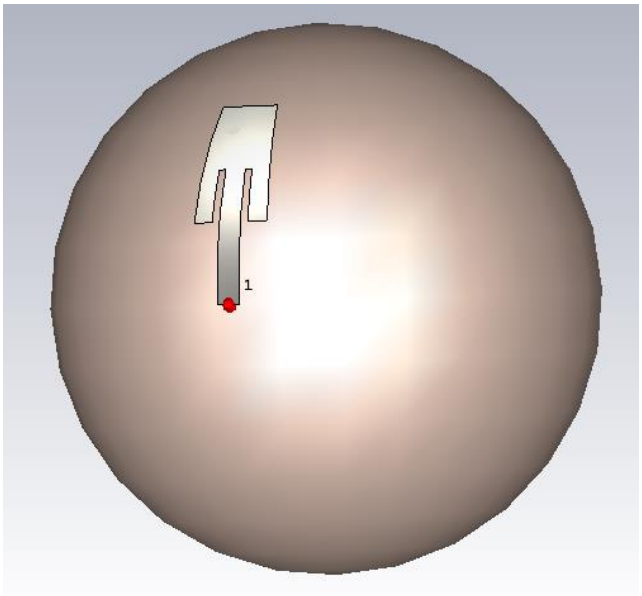

Figure 3.17: CST model of a spherical-rectangular microstrip antenna mounted on a dielectric coated conducting cylinder

3.3.9. Spherical Antennas in Array Formations:

The cavity method provides sufficient information to analyze the behavior of a spherical microstrip antenna in terms of radiation pattern and input impedance as explained in this section so far. Throughout the analysis process of a single spherical antenna, it is possible to stay in the analytical domain which makes this approach preferable compared to numerical ones. When a spherical array is considered, it

could be assumed at first that the analysis becomes more difficult as number of antenna elements increased in the array system. Nevertheless, this is not the case because analytical model allows the superposition principle to be applied on the antenna elements to derive the total effect.

The characteristic of an array depends on three parameters: the type of antennas forming the array, the number and formation of antennas and the feeding configurations of antenna elements. All three aspects of an array must be regarded to obtain the overall response of the system. Cavity method is quite sufficient to take all these parameters into account easily to some extent. Since it is possible to superpose the responses of antennas, adjusting the characteristics of each antenna element is enough to obtain their contributions to the system. For example, phase and magnitude information of the feeds can be inserted to the cavity field expressions derived in this section. Position and shape information of the antennas are also included in the cavity method analysis; therefore, repeating the same analysis for each antenna element is required. The radiated fields generated by all elements are summed at the end to obtain the fields at every point at space which makes it possible to draw the radiation pattern of the array.

Although the cavity method proves to be a useful method in analyzing the spherical antennas in single and array configuration, some drawbacks can be observed for particular situations. It is a method that makes use of certain approximations; therefore, the results for a single antenna are not totally accurate. Superposition of antenna responses for the analysis of arrays may seem a simple and faster method. However, each element has its own error residual and this accumulates as more and more antennas are included in the system. Depending on the residual error level, the number of antennas must be kept as low as possible to prevent the method from leading to inaccurate results. Another factor that may contribute to the error accumulation is the concept of mutual coupling. As the cavity model with superposition method for array problems that is presented in this chapter does not include any information about the interactions of the antennas constructing the array, mutual coupling effects are completely neglected. This effect rises in magnitude as antennas are kept electrically

closer to each other eventually causing resonance frequency shifts due to input impedance variations and distortions in radiation pattern.

The example simulations exhibit that the possible aforementioned drawbacks of cavity method application on antenna arrays can be avoided considerably when the element separations (Δx) depicted in Figure 3.18 are kept large enough.

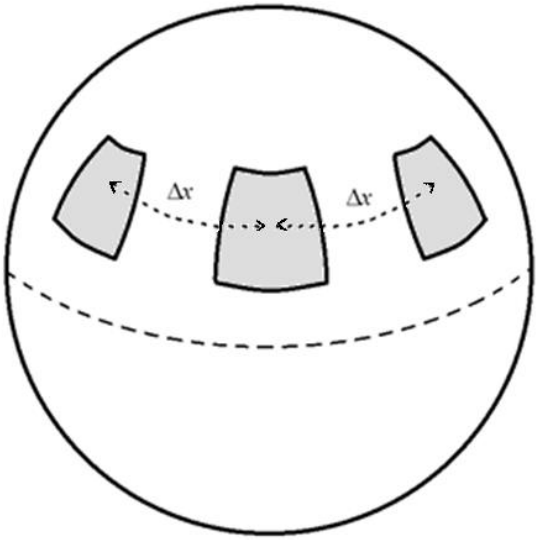

Figure 3.18: Three element rectangular patch array mounted on a conducting sphere

3.3.10. Comments on Direction Finding and Beam Forming Applications:

The smooth analysis and design capability of cavity method when applied on spherical antenna arrays allows the utilization of the approach on various applications such as beam forming and the detection part of direction finding. These applications require a piece or pieces of beam to be aligned in a way that they point to the desired locations or directions in space.

The radiation pattern of an antenna array depends on the type of antenna elements, their position formations and feeding of each element. Furthermore, some applications require the scanning of space which can be handled by mechanical rotation or more preferably by phased array algorithms where phase or magnitude of antenna

elements are adjusted to form an aimed pattern at each sampling instance. Phased array algorithms are carefully constructed because a poorly calculated design may lead to resolution drop, rise of undesired side beams or complete failure of the expected pattern. Therefore, a complicated procedure may be required to understand, analyze and design these antenna applications. However, a spherical antenna array located on a spherical structure proves to be useful in easing the calculation process due to its natural geometry. A uniformly distributed array constructed on a spherical structure as in Figure 3.19 can generate beams that can span the space without resorting to complex phased array algorithms. On/off switching of the array elements with a calculated configuration is sufficient to generate a narrow beam targeting any direction in space at any instance.

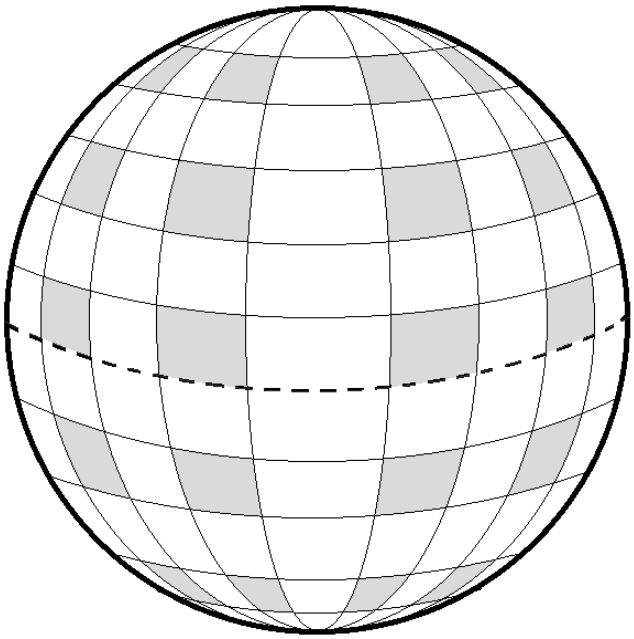

Figure 3.19: A dense array presentation of rectangular patches mounted on a dielectric coated conducting sphere

The advantage of spherical antenna arrays in simple direction finding and beam forming applications may prove to be quite significant. Obviously, the incorporation of phased array algorithms in these antenna systems provides much stronger beam forming abilities. However, it is certain that the space-spanning-geometry of antenna

elements on spherical structures will not only cause an improvement on the characteristic features of the system but it will decrease the calculation complexity as well.

Knowing that the spherical shapes further increase beam forming capabilities and decrease calculation weight, it is necessary to mention here the contribution of cavity method to the analysis simplicity. As the previous section points out, cavity model is a strong model that can quite precisely estimate the radiation patterns of spherical arrays without experiencing complex calculations. It adds up the responses of each element in the antenna array to reach the total response whether there are phase/amplitude differences between antennas or not. Therefore, preferring the cavity method for the analysis and design of such structures may prove to be more advantageous as long as the aforementioned restrictions caused by high element density are carefully avoided.

3.3.11. Improvement of Cavity Method by Coordinate Transformation of Array Elements:

The cavity model provides a smooth analysis approach to spherical-rectangular antenna elements and arrays. Nevertheless, the analysis steps require that all the elements be bounded by the spherical coordinate grids on the surface of the sphere they are mounted on. As a result, elements may have different geometrical structures which can affect the impedance matching and resonance frequencies, if not the radiation patterns. In other words, a rectangular-spherical antenna array may require a design where the feed structure of each element is considered separately and the resonance frequencies diverge as the shape distortion increases. As a result, the additional work load is introduced. The geometrical effect of positioning is demonstrated in Fig. 3.20. As the elements recede from the equator, the grid deformation level also rises. Another point to mention is that the positioning of the elements at the poles of a sphere becomes impossible with the investigated method in this work. To sum up, an additional technique should be introduced to overcome such difficulties and to contribute to the completion of the spherical-rectangular array modeling.

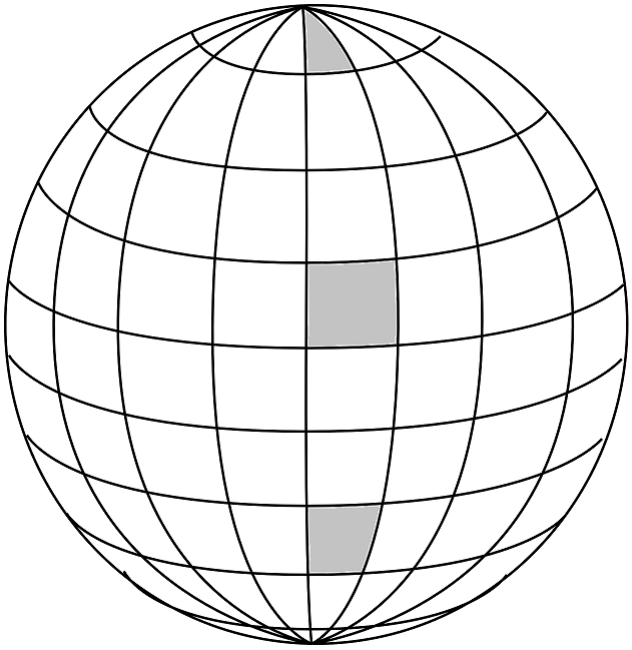

Figure 3.20: An arbitrary spherical-rectangular printed antenna array aligned with respect to the spherical coordinate grids

A spherical-rectangular printed array of equal elements can be realized with the use of consecutive vector transformation techniques. The far-field expressions of each element can be derived and transformed in space according to the position of each element with respect to a reference element. In this study, a rectangular antenna mounted on a specific point at the equator of the sphere ($\theta=\pi/2$, $\phi=\pi/2$) where grid deformation is at minimal levels is considered as the reference element. The transformation effect each array element is exposed to can be applied to the field expression of this particular reference element in order to derive the radiated fields of all antennas. Finally, the fields are superposed to obtain the total effect of the array which consists of equal rectangular elements without grid distortions.

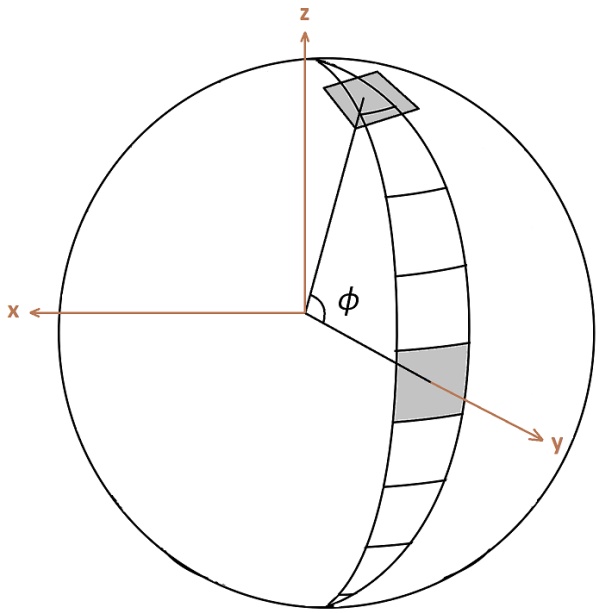

Figure 3.21: The reference and displaced elements forming a spherical-rectangular antenna array centered at ϕ= 90°

The field transformations can be implemented by utilizing the vector rotation matrices given in [58]. These matrix expressions apply a rotation to vectors in Cartesian format around a specified axis where the reference frame stands still. It is necessary to note, however, that the Cartesian vectors rotate with respect to their local origins and the keep their spatial positions. Therefore, application of this rotation matrix is not enough to derive the fields of a relocated antenna with respect to a reference position as the fields need to rotate along with it. Fig. 3.21 depicts the relocation of the reference element in θ direction. This relocation causes the rotation of all radiated fields about x-axis as well. The corresponding rotation matrix is:

$$R(\beta)=\begin{bmatrix}1 & 0 & 0\\ 0 & \cos\beta & -\sin\beta\\ 0 & \sin\beta & \cos\beta\end{bmatrix} \tag{3.111}$$

and the rotated fields can be evaluated by:

$$E_R = R(\beta)\begin{bmatrix} E_x \\ E_y \\ E_z \end{bmatrix} \tag{3.112}$$

where E_R represents the rotated fields in Cartesian form. Another step must be taken in order to introduce the new location of the antenna to the expressions of rotated fields. For this purpose, the position vectors of the field vectors are also rotated using (3.112) and by switching back to spherical coordinate system, a mapping between the new and old locations of rotated fields are obtained. The patterns in desired planes are derived afterwards with careful implementation of this mapping of coordinates. An example of this transformation employed on an array structure of spherical-rectangular printed antennas is also given in chapter 4.

Even though the transformation technique explained in this section is basically independent of the cavity method analysis, it is an essential part to mention for the sake of completeness. Transformation of antennas provides the possibility for an array application of equal elements and for antenna positioning independent of spherical grid format.

CHAPTER 4

NUMERICAL RESULTS AND APPLICATIONS

4.1. Introduction

The utilization of cavity model on spherical-rectangular antennas was explained in the previous chapters. The derivation of field equations in spatial domain and construction of radiation patterns for an array format were presented in detail.

This chapter focuses on the possible applications of the method proposed in this study. The radiation pattern of various types of antennas and phased arrays are analyzed and compared with the computer simulated counterparts. Further comments are included to discuss the strength of the cavity method in providing solutions for direction finding and beam forming applications.

4.2. Radiation Field Characteristics of a Spherical-rectangular Microstrip Antenna Mounted on a Conducting Sphere:

As discussed in chapter 3, cavity model is a powerful method for determining the radiation patterns of microstrip antennas. In this section, a particular spherical-rectangular antenna described in Table 4.1 is considered for the realization of the cavity method.

Table 4.1: The parameters of a particular spherical-rectangular patch antenna

Antenna Parameters			
$\mathbf{r_1}$	0.1 m	$\mathbf{f_{fund}}$	1.46 GHz
$\boldsymbol{\delta_r}$	4.5 mm	$\boldsymbol{\epsilon_r}$	4.3
$\boldsymbol{\theta_1}$	$\pi/4$	$\boldsymbol{\phi_1}$	$4\pi/9$
$\boldsymbol{\Delta\theta}$	$\pi/6$	$\boldsymbol{\Delta\phi}$	$\pi/9$

A simple CST model of the patch antenna on a sphere is given in Figure 4.1 for the sake of comprehensive visualization. The red mark on the patch points the position of the port where the antenna is fed. The resulting radiation pattern of the antenna is depicted in Figure 4.2.

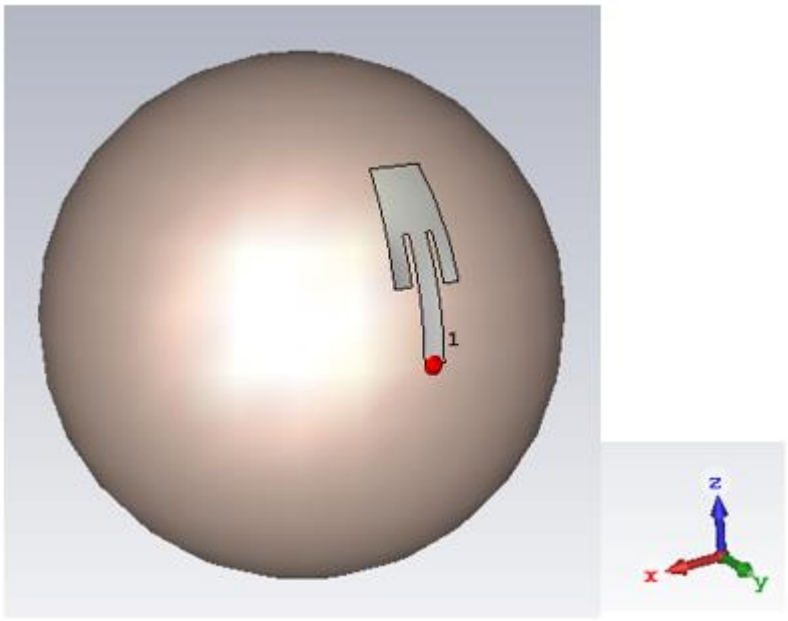

Figure 4.1: The CST model of the antenna with the given parameters in Table 4.1

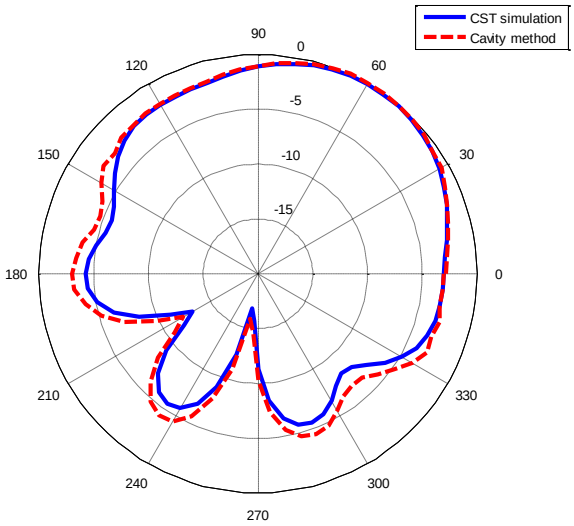

Figure 4.2: yz-plane radiation pattern comparison of calculated and simulated results for spherical-rectangular antennas

As demonstrated in Figure 4.2, the pattern derived by the cavity method is in agreement with the CST simulated results. Especially, the main beam is in complete coincidence with the simulation which is expected because cavity model is stronger in estimating the main lobes rather than the side lobes. Another reason for the discrepancies between two curves may be the numerical calculation errors that arise when the calculation of Legendre functions and their derivatives are made. Furthermore, the feed line of the patch also generates radiation that is included in the simulated result but not in the analytical one. However, despite all these sources of error, the method still provides an accurate result with error factor of 1 dB at most.

4.3. Radiation Field Characteristics of a Spherical-disk Microstrip Antenna Mounted on a Conducting Sphere:

The spherical-disk antennas are in subdomain of spherical-rectangular antennas. The same approach and analysis steps can be applied to obtain the radiation pattern characteristics. Due to matching considerations and simplicity in manufacturing, these

antennas are preferred to be fed by a coaxial line instead of microstrip line. Therefore, the analytical estimations and simulations are carried out for this type of feeding configuration. The physical structure of the antenna is described in Table 4.2 and the CST model is demonstrated in Figure 4.3.

Table 4.2: The parameters of a particular spherical-disk patch antenna

Antenna Parameters			
$\mathbf{r_1}$	0.1 m	$\mathbf{f_{fund}}$	510 MHz
$\boldsymbol{\delta_r}$	4.5 mm	$\boldsymbol{\epsilon_r}$	4.3
$\boldsymbol{\theta_1}$	0	$\boldsymbol{\phi_1}$	0
$\boldsymbol{\Delta\theta}$	$\pi/4$	$\boldsymbol{\Delta\phi}$	2π
$\boldsymbol{\theta_f}$	$\pi/9$		

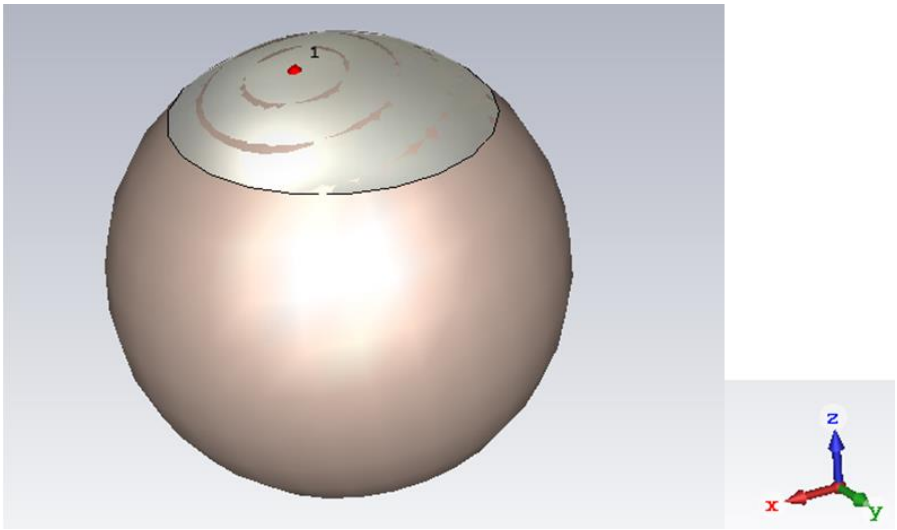

Figure 4.3: The CST model of the antenna with the given parameters in Table 4.2

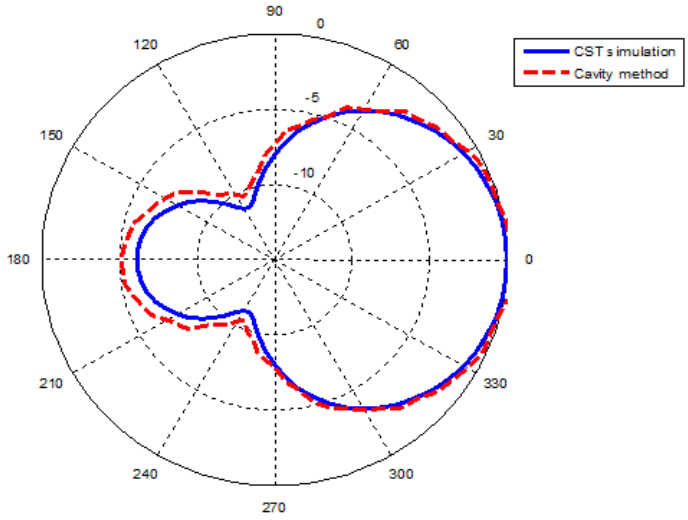

Figure 4.4: yz-plane radiation pattern comparison of calculated and simulated results for spherical-disk antennas

Circular type antennas may seem different from rectangular ones; however, analytical approach is still the same. The cavity fields confined under the patch can be replaced by equivalent magnetic currents in azimuthal direction which are located at the patch edges. In the fundamental mode, these currents radiate in the presence of the conducting sphere in such a way that a large main lobe and a smaller back lobe occurs in the pattern (Figure 4.4). As mentioned in the previous section, cavity model is quite accurate to estimate these radiation characteristics, especially the main lobes.

4.4. Radiation Field Characteristics of a Two-element Array of Spherical-rectangular Microstrip Antennas Mounted on a Conducting Sphere:

It was shown that cavity model provides close estimations in evaluating the radiation patterns. The same can be claimed for the estimation of the patterns of arrays. In order to derive the total fields, two spherical-rectangular antennas described in Table 4.1 are positioned in the opposite sides of the conducting sphere. The field contribution of each antenna are then evaluated and superposed to obtain the final field distribution of the space. Another point to note is that the antennas are fed in three different configurations: in phase, quadrature phase and inverse phase excitations.

Therefore, the results of a phased array operation are also derived. The Figure 4.5 gives an idea of how the antennas are located on the conducting sphere and Table 4.3 describes the excitation methods of each configuration in Figure 4.6.

Table 4.3: The excitation configurations for each case presented in Figure 4.6

Excitation Configurations		
	Antenna I	**Antenna II**
Case a	*Mag*=1 , *Phase*=0°	*Mag*=1 , *Phase*=0°
Case b	*Mag*=1 , *Phase*=0°	*Mag*=1 , *Phase*=90°
Case c	*Mag*=1 , *Phase*=0°	*Mag*=1 , *Phase*=180°

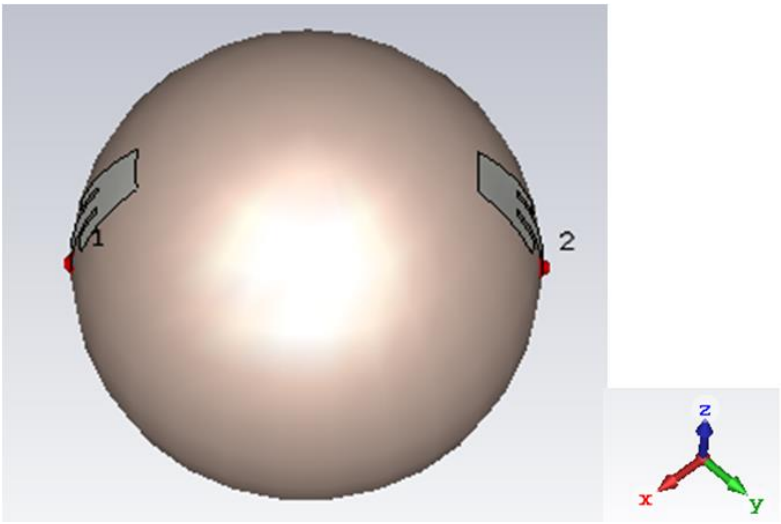

Figure 4.5: The CST model of the two element antenna array with elements placed 180° apart

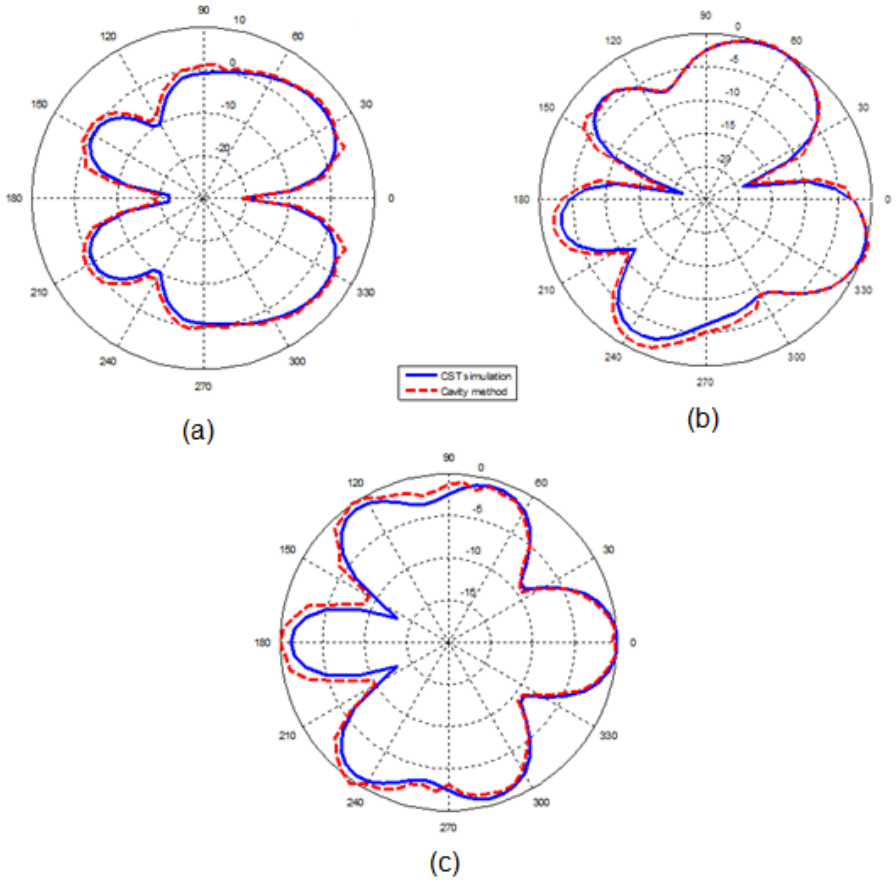

Figure 4.6: yz-plane radiation patterns for excitation configurations of a) in-phase, b) quadrature-phase, c) inverse-phase

It is apparent in Figure 4.6 that the analytical model is in agreement with the CST simulated radiation patterns. Any type of excitation configuration of phased arrays can be analyzed by means of cavity method without abundant error. The excitation choices can be extended by adjusting the magnitude ratios of the feeds, but the results will keep matching.

4.5. Radiation Field Characteristics of a Four-element Array of Spherical-rectangular Microstrip Antennas Mounted on a Conducting Sphere:

In this section, the results of a four-element array are shared to investigate if the number of antennas included in the analysis affects the accuracy of the analytical

evaluation. The antennas are placed with quadrature (90 degree) spacing as depicted in Figure 4.7. The antenna characteristics are as given in Table 4.4. The order of antennas is different from the one in the previous section in such a way that they are located in a different alignment and the feed lines are in azimuthal direction. The element excitations are equal.

Table 4.4: The parameters of another spherical-rectangular patch antenna

Antenna Parameters			
$\mathbf{r_1}$	0.1 m	$\mathbf{f_{fund}}$	1.5 GHz
$\boldsymbol{\delta_r}$	4.5 mm	$\mathbf{\epsilon_r}$	4.3
$\boldsymbol{\theta_1}$	4π/9	$\boldsymbol{\phi_1}$	5π/12
$\boldsymbol{\Delta\theta}$	π/9	$\boldsymbol{\Delta\phi}$	π/6

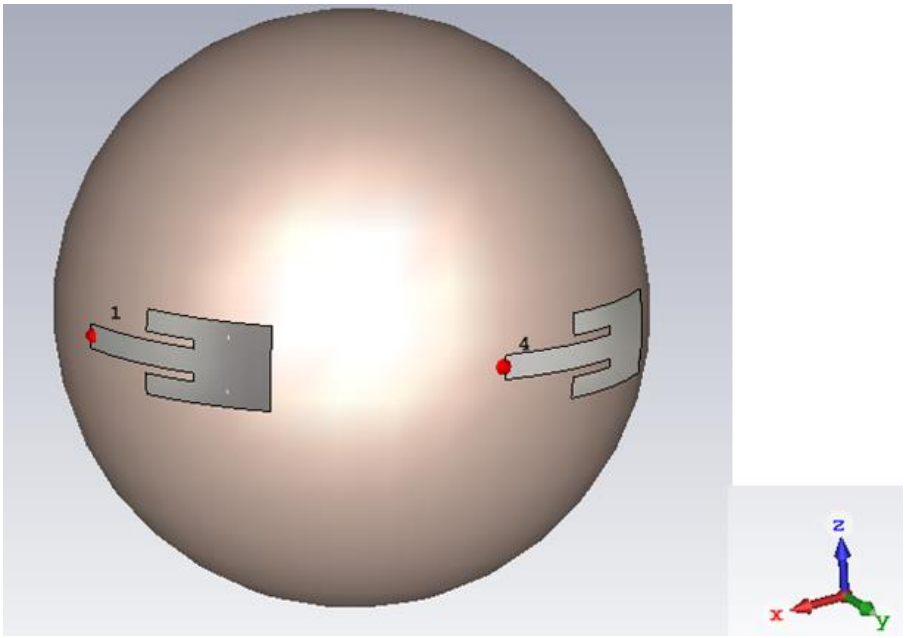

Figure 4.7: The CST model of the four element antenna array with elements placed 90° apart

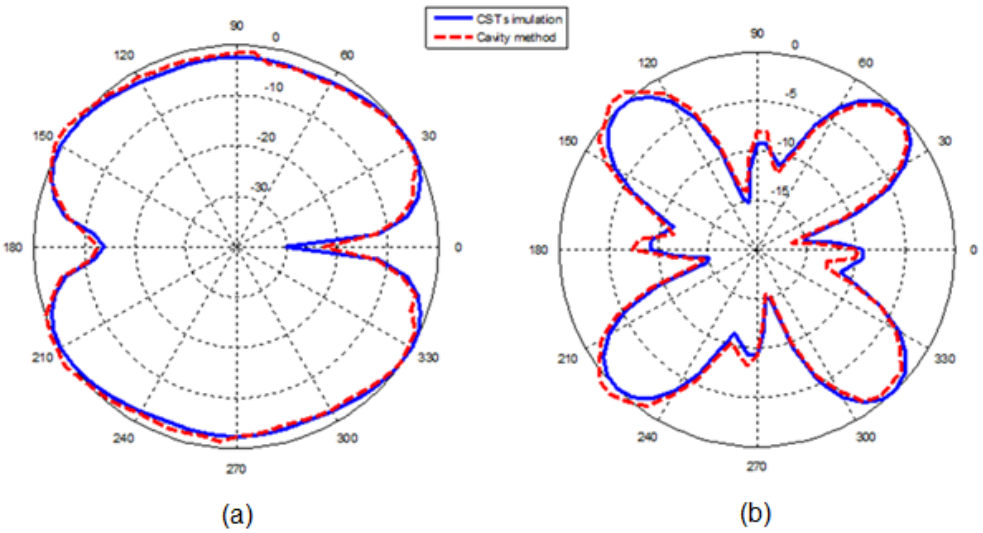

Figure 4.8: yz-plane (a) and xy-plane (a) radiation patterns for equally excited elements

The coincidence of radiation pattern curves of analytical and simulated results in Figure 4.8 is an evidence for the strength of the cavity method in evaluating patterns of antenna arrays of multiple elements. These results encourage the utilization of the method for various array structures, especially for the arrays used in applications such as direction finding and beam forming. Although numerical methods are preferred mostly for these applications, cavity method may still prove to be a useful and fast approach for simple-element-arrays which were discussed in this study.

4.6. Investigation on the Beam Forming Capability of a Twelve-element Array of Spherical-rectangular Microstrip Antennas Mounted on a Conducting Sphere:

In this section, twelve antenna elements with the given properties in Table 4.5 are ordered in azimuthal direction with equal intervals as indicated in Figure 4.9. Instead of activating all the elements, only a few can are excited to observe the resulting ra-

diation patterns. The equal excitation of antennas in particular groups can allow the formation of directive beams.

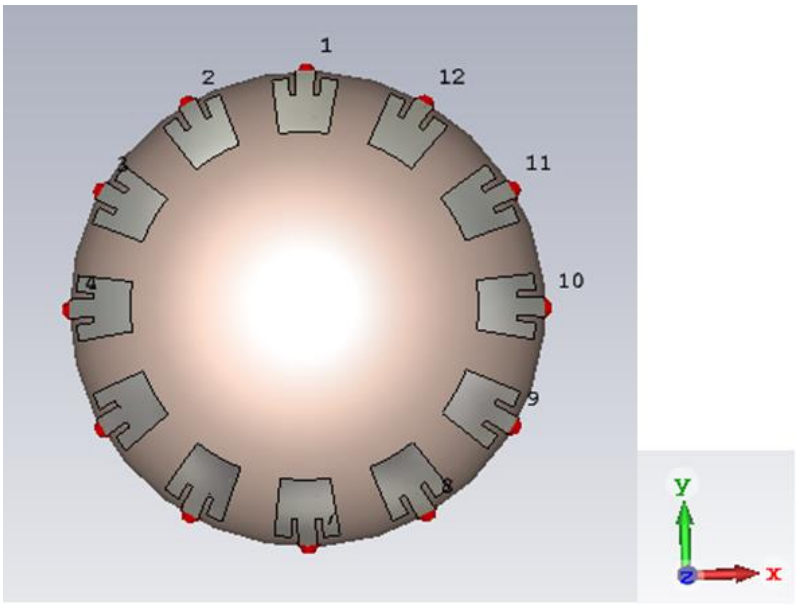

Figure 4.9: The CST model of the twelve element antenna array with equally distributed elements

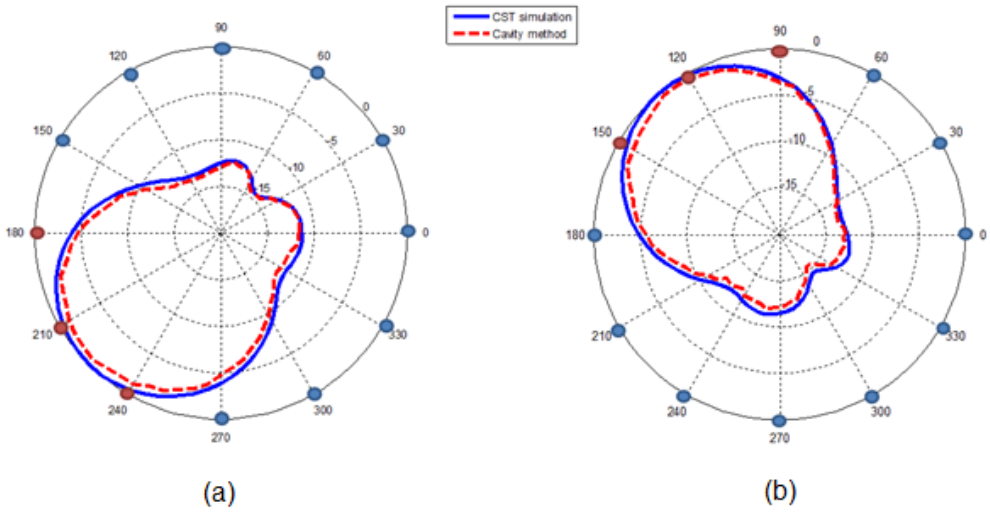

Figure 4.10: xy-plane radiation patterns obtained by activating the antennas located at a) ϕ=180°, ϕ=210°, ϕ=240°, b) ϕ=90°, ϕ=120°, ϕ=150°

Activating the arrays in an on-off manner causes the antennas to concentrate their beam in a specific direction. The Figure 4.10 gives some examples of beam forming capability of azimuthally aligned antennas. All feeds have the same phase and magnitude and activated elements are depicted in red circles. In this example, the main beam is directed to a desired location by exciting only a quarter of the number of antennas. The back lobes are at least 12 dB lower than the main beam. However, the main beam is quite large, thus the directivity of the array can be improved further by introducing the phased array application. Another example is given in Figure 4.11 where more of the elements are activated to form two beams.

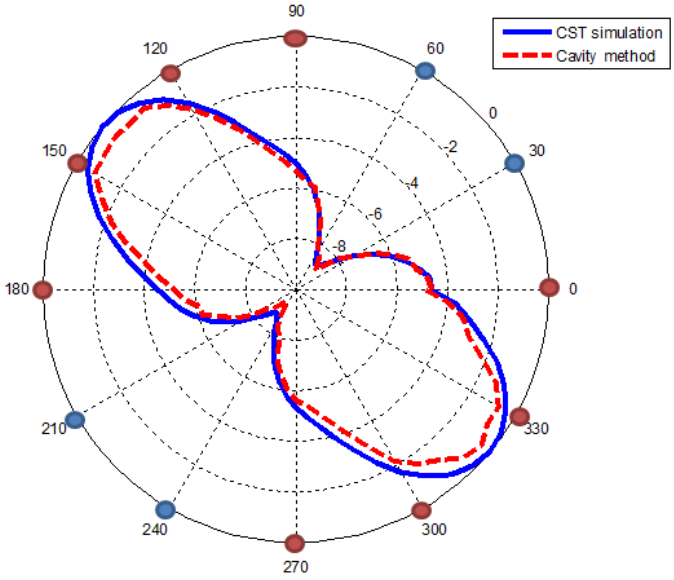

Figure 4.11: xy-plane radiation patterns obtained by activating the antennas located at ϕ=90°, ϕ=120°, ϕ=150°, ϕ=180°, ϕ=270°, ϕ=300°, ϕ=360°

The excitation of eight elements in the order given in Figure 4.11 enables the formation of two equal sized beams. In this configuration, both the front and back of the spherical structure are illuminated by the antenna beams which can be a beneficial attribute regarding the direction finding applications. The ordered switching of these activated antennas can also allow the scanning of space in the azimuthal direction without making use of phased array algorithms.

The advantageous aspect of the spherical structures as shown in this section is that their surface area faces the whole space. Therefore, an antenna array aligned on the surface of a sphere can form beams that span entire space without any mechanical movement or the phased array concept; but only by using on-off algorithm. The extra contribution of phased array systems may improve the capability of the arrays in applications such as beam forming and in the detection part of direction finding applications.

Although the flexibility of spherical antenna arrays is apparent and the capability of cavity model in evaluating the radiation patterns is evident, the dense distribution of array elements may cause certain problems as mentioned in the previous chapter. The cavity model is an approximation itself; therefore, the superposition of the field distribution of each element in the array contributes to the error magnitude. If the number of array elements is abundant, then the accuracy of the overall solution drops. Another source of error is the mutual coupling between the array elements. The antennas in close proximity start to affect each other by introducing an impedance shift for each other and their behavior may differ considerably. Therefore, one must pay attention to the electrical distance between antennas and keep them sufficiently dispersed. It can be said in our case that distances larger than $\lambda/10$ seems enough to avoid such a phenomenon. The Figure 4.12 shows the effects of densely distributed antennas on the radiation pattern of each element. In this configuration, fifteen elements are densely positioned in azimuthal alignment with intervals of $\lambda/15$. The antennas forming the array were described in Table 4.1.

4.7. Investigation on the Beam Forming Capability of a Twelve-element Array of Spherical-rectangular Microstrip Antennas Mounted on a Conducting Sphere:

In this section, twelve antenna elements with the given properties in Table 4.5 are ordered in azimuthal direction with equal intervals as indicated in Figure 4.9. Instead

of activating all the elements, only a few can are excited to observe the resulting radiation

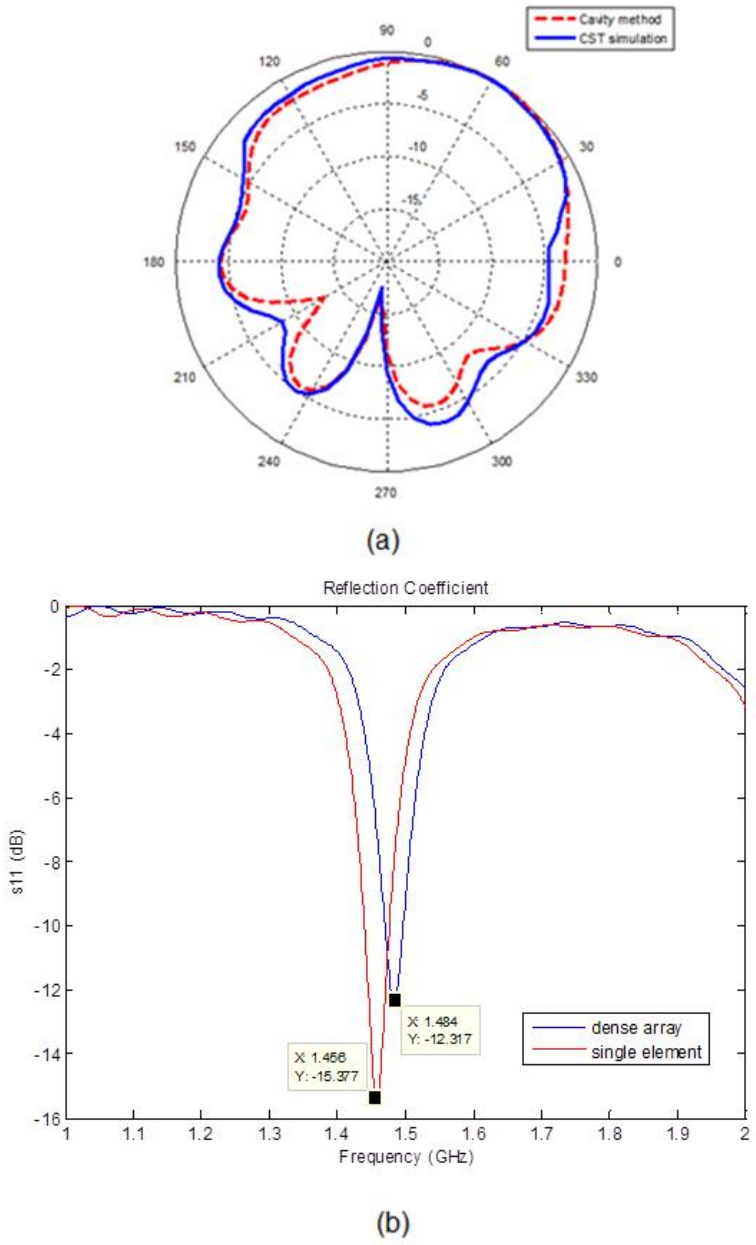

Figure 4.12: a) Radiation pattern comparison of calculated and simulated results for a single antenna in a dense (fifteen element) array, b) Fundamental frequency shift due to the effects of dense array formation

The dashed line in Figure 4.12a shows the result of the cavity model for a single antenna. Obviously, the analytical cavity model does not include effects of mutual cou-

pling. Nevertheless, continuous line which is the CST simulation result demonstrates the effect of mutual coupling with a slightly distorted pattern. The Figure 4.12b was also added to show that the resonance frequency of antennas also shift due to the load impedance introduced by the antennas in close proximity as shown in Table 4.5. The effect of error accumulation due to the high quantity of antennas in the array was not given in these figures, yet it stands as another significant source of error that degrades the accuracy, and thus the attractiveness of the cavity model.

Table 4.5: The effect of antenna separations on the fundamental frequency

Antenna Separations	Fundamental Mode Frequency (GHz)	Shift in Frequency
$\lambda_o/2$	1.4656	0.00 %
$\lambda_o/10$	1.4671	0.10 %
$\lambda_o/15$	1.4760	0.70 %
$\lambda_o/30$	1.5022	2.50 %

4.8. Comparison of Spherical-Rectangular Antenna Arrays Consisting of Elements that are Bounded and Unbounded by the Spherical Grids:

In this section, the effects of spherical grids on both radiation pattern and input impedances of spherical-rectangular antennas are investigated. Fig. 4.13 depicts the elements bounded and unbounded by the spherical grids at the same coordinates. The grid bounded element changes its shape as it approaches to the pole. On the other hand, the transformed element preserves its original rectangularity despite its position.

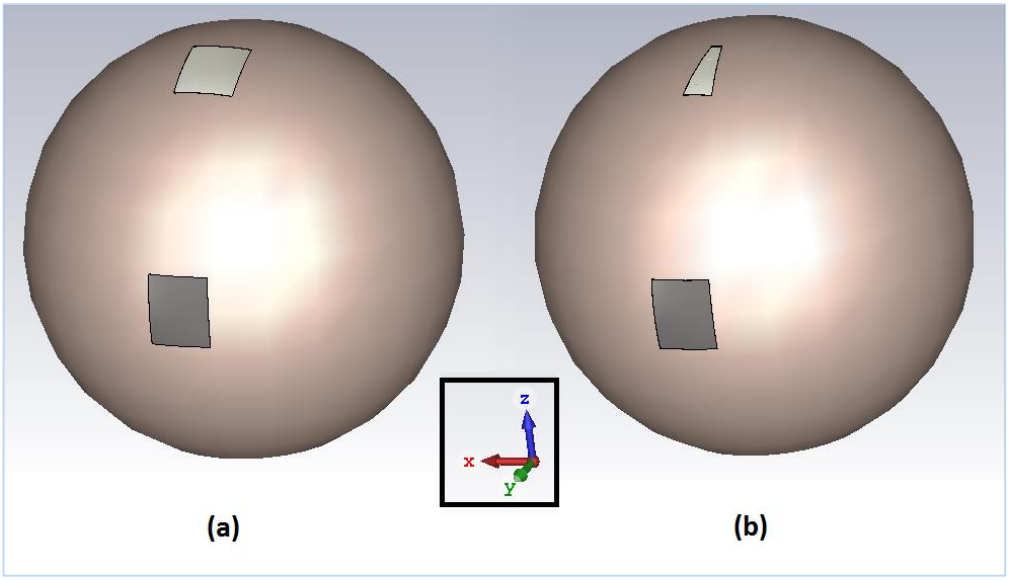

Figure 4.13: Demonstration of the nongrid (a) and grid (b) rectangular antennas along with the reference element centered at φ = 90° with parameters: θ_1=80°, $\Delta\varphi$=16°, $\Delta\theta$=20°, r_1=10cm, δ_r=4.5mm, ϵ_r=4.3

The change in their shapes causes the grid bounded elements to be handled cautiously since they may suffer from poor feeding. Furthermore, the distortion in their shapes gives rise to a shift in their frequency response. The Fig. 4.14 and 4.15 indicates the radiation pattern and s_{11} comparisons between two antenna geometries that have the same angular dimensions $\Delta\theta$ and $\Delta\varphi$.

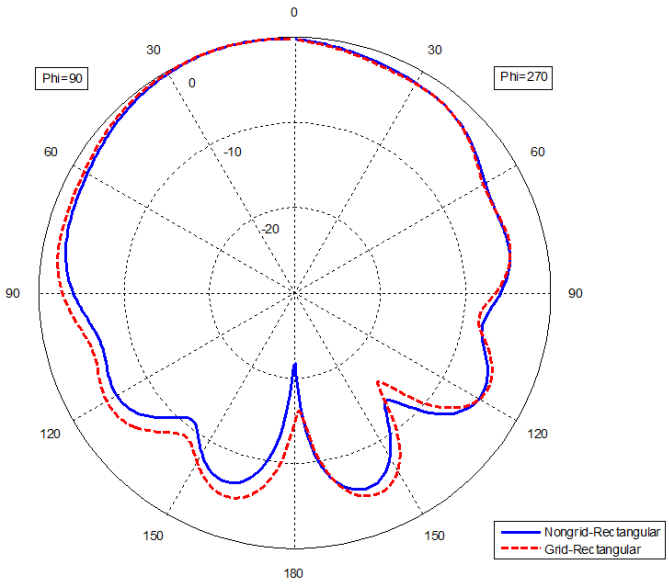

Figure 4.14: Comparison of normalized E-plane radiation patterns of grid-bounded and nongrid rectangular antennas in Fig. 4.13

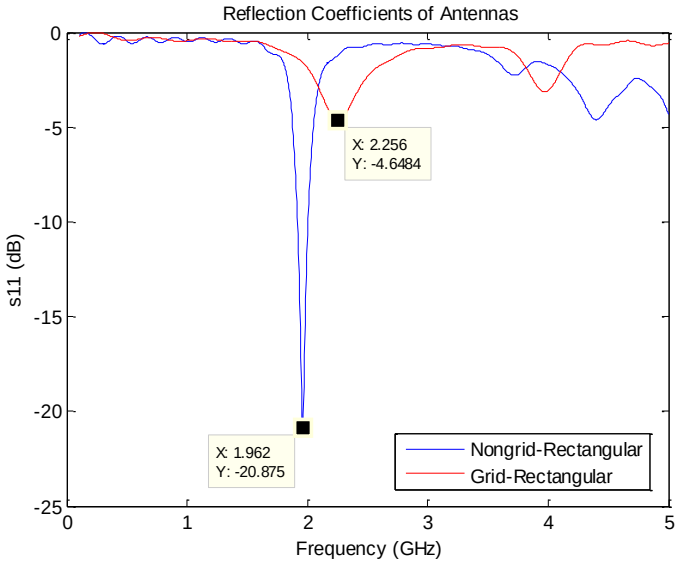

Figure 4.15: Comparison of reflection coefficients of grid-bounded and nongrid rectangular antennas in Fig. 4.13

Fig. 4.14 shows that the normalized radiation patterns do differ negligibly for this particular case. However, their reflection coefficients are completely different which

means that there is a shift in resonance frequency and there is a need for repositioning of the feeding point in order to ensure efficient radiation.

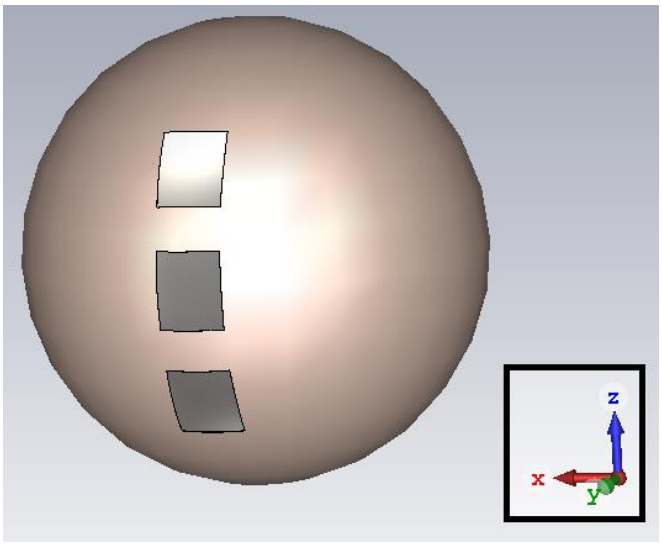

Figure 4.16: Demonstration of a three-element-array formed by the reference element at equator with φ = 90° and its transformed counterparts with displacement angle ϕ=30°

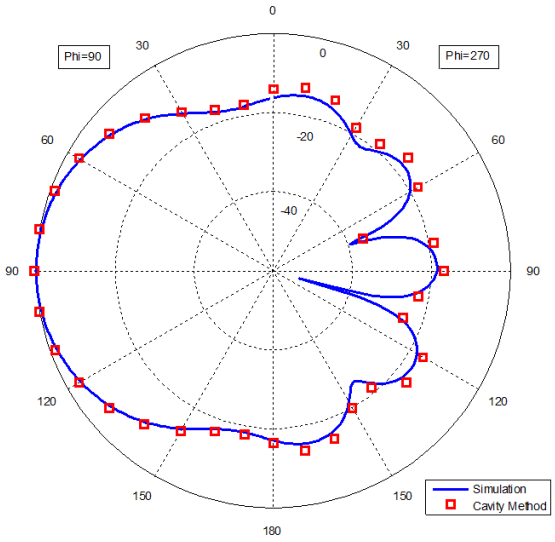

Figure 4.17: Normalized E-plane radiation patterns obtained by the cavity model analysis and CST simulations for the rectangular array in Fig. 4.15

In order to validate the transformation technique explained in Chapter 3, a three-element spherical-rectangular antenna array depicted in Fig. 4.16 is also formed and analyzed. The comparison of the normalized radiation pattern results from analytical model and CST simulations are given in Fig. 4.17 where a strong coincidence between each plot can be observed. Therefore, it is appropriate to conclude that the analytical model can be made capable of handling array elements that do not fit the spherical grid format by means of careful field transformations.

4.9. Investigation of Curvature Effect on Radiation Pattern Characteristics:

In this section, the effect of curvature is observed by changing the radius of curvature of the printed antenna. Fig. 4.18 demonstrates the differences of E-plane radiation patterns on a rectangular patch with a side length of 3.5 cm. As the curvature increases, the far-field pattern starts to create larger side and back lobes even though the main lobe remains almost the same. The case with the largest radial dimension shows similarities to characteristics of planar printed antennas as the back lobes are quite small at this configuration and the main beam becomes the dominant radiation. Consequently, the curvature degree has important effects on the radiation pattern characteristics of printed antennas. Therefore, spherical antennas cannot be examined with analysis methods of planar antennas as the planar approach begins to fail as curvature increases.

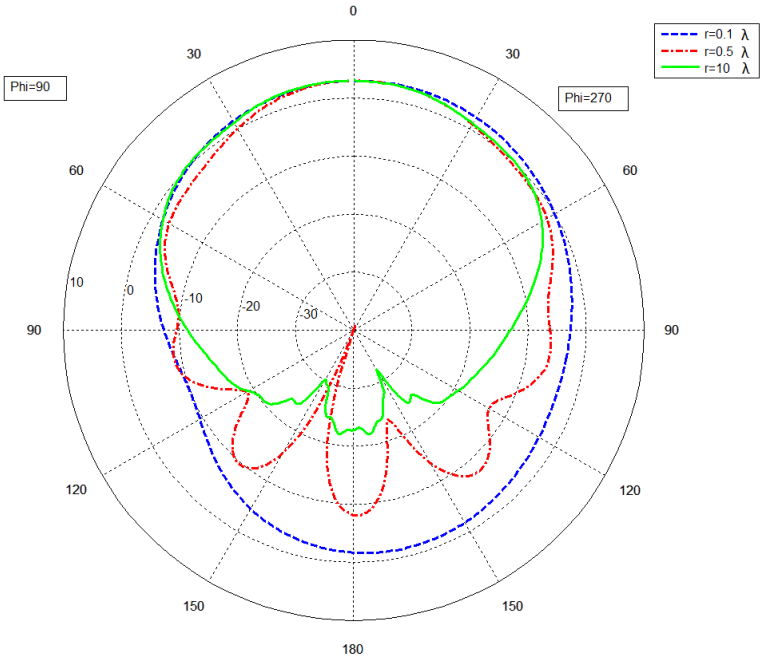

Figure 4.18: E-plane normalized radiation patterns of a particular spherical-rectangular printed antenna (3.5cm x 3.5 cm) with different spherical radii

CHAPTER 5

CONCLUSION

5.1. Summary and Conclusions:

In this thesis, spherical microstrip antenna and antenna arrays were investigated by employing the cavity model as the basic analysis approach. The main idea was determining the magnetic equivalent currents flowing at each side of the patch so that the patch and dielectric structure could be ignored and the problem of interest turned into the radiation of magnetic currents in the presence of a conducting sphere. The radiated fields were modeled by spherical wave harmonic functions. The field expressions were transformed to spectral domain by means of the Vector-Legendre transformation in order that the boundary conditions could be applied on them more efficiently. Finally, the field expressions were configured to obtain far-field characteristics of the antennas and radiation pattern were derived. For antenna array structures, the analytical results of each antenna were superposed to have overall pattern characteristics.

The analysis steps in this study remains in the analytical domain due to the nature of cavity model. The steps that lead to the determination of fields are straightforward and do not require a solution process of any complex numerical equation or any complex calculation. Furthermore, it gives a physical insight since the solution process carried in an explicit manner that does not cause confusion throughout the study due to clear cause-effect relations. Last but not least, the obtained results are reasonable and mostly accurate if requirements of cavity model analysis are met correctly.

The strength of the approach is apparent in the radiation pattern results of various antennas and various antenna array formations.

The reliability of the method was vindicated for different antenna types and arrays. The radiation field characteristics for each case presented in this study were compared with the simulated results in the CST (Computer Simulation Technology) software design environment. The results showed little difference between these pattern plots ensuring the effectiveness of the cavity model. Although this model is not efficiently applicable to microstrip patch types of arbitrary shapes which seems as its disadvantage against full-wave analysis methods, its accuracy and simplicity proves it to be a strong solution model for such antenna problems.

Another outcome of the study can be summarized as the employment possibilities of spherical printed antenna arrays for direction finding and beam forming applications. The radiation pattern results in this study provoke the idea that the physical structure of such antenna arrays can be utilized to have narrow beams in various directions without resorting to complicated phased array algorithms; hence these structures may become an alternative way to solve difficult direction finding problems.

5.2. Future Work

This study can be extended in various directions that still require further examinations:

- The input impedance calculations using cavity model for different feeding networks for spherical microstrip printed antennas and their comparisons with computer simulations
- Cavity model analysis of spherical microstrip printed antennas with multiple dielectric substrate layers

- The cavity model analysis of spherical microstrip printed antenna arrays that includes the mutual coupling effect between elements
- Investigation of the spherical microstrip printed antenna arrays for applications of direction finding and/or beam forming

REFERENCES

[1] J. Q. Howell. Microstrip antennas. *G-AP Int. Symp.*, Williamsburg, VA, Dec. 1972.

[2] Y. Cheong, K. Lee, J. Yook. A novel antenna cover of microstrip patch antenna for ultra-fast aircraft. *IEEE Proc. Asia-Pacific Conference on Communications*, 2006.

[3] D. Gray, H. Tsuji, and M. Suzuki. Beacon microstrip patch antenna for DOA demonstration from prototype stratospheric aircraft. In *Proc. Antennas Propag. Society Int. Symp.*, 2007.

[4] V.S. Kumar, V.V. Srinivasan, and V.K. Lakshmeesha. Sequentially rotated microstrip array antenna at X-band for spacecraft. *IEEE Proc. Applied Electromagnetics Conference*, 2007.

[5] A. Sondas and M.H.B. Ucar. An implantable microstrip antenna design for biomedical telemetry. *IEEE Proc. International Conference on Electronics, Computer and Computation*, 2014.

[6] V. S. Rao, V.W.Paradkar, C.H.Satyanarayana. Study and analysis of microstrip antenna system on square body for telemetry applications. *IEEE Proc. International Conference on Microwave, Optical and Communication Engineering*, 2015.

[7] A. Kiourti, R. Basten, K. Esselle, and J.L. Volakis. UWB Antennas on Conductive Textiles. 2016 IEEE International Symposium on Antennas and Propagation, Fajardo, Puerto Rico, Jun. 26 – Jul. 1, 2016.

[8] Tatsuo Itoh. Spectral domain immitance approach for dispersion characteristics of generalized printed transmission lines. *Microwave Theory and Techniques, IEEE Transactions on*, MTT-28.

[9] B. Ke and A.A. Kishk. Analysis of spherical circular microstrip antennas. In *IEEE Proceedings H (Microwaves, Antennas and Propagation)*, volume 138, pages 542–548. IET, 1991.

[10] A.A. Kishk. Analysis of spherical annular microstrip antennas. *IEEE Trans. Antennas Propag*, 41(3):338–343, 1993.

[11] K. Araki, and ITOH, T. Hankel transform domain analysis of open circular microstrip radiating structures. *IEEE Trans.,* AP-29, pp. 8489, 1981.

[12] D.M. Pozar,. Input impedance and mutual coupling of rectangular microstrip antennas, *IEEE Trans.,* AP-30, pp. 1191-1196, 1982.

[13] Hong-Twu Chen and Kin-Lu Wong. Analysis of probe-fed spherical-circular microstrip antennas using cavity-model theory. *Microwave and Optical Technology Letters*, 7(7):309–312, 1994.

[14] Y. T. Lo, D. Solomon, and W.F. Richards. Theory and experiment on microstrip antennas. *IEEE Trans. Antennas and Propagation,* vol. AP-27, pp.137-145, 1979.

[15] M. Irsadi Aksun, Shun-Lien Chuanga, and Yuen Tze Lo. On slot-coupled microstrip antennas and their applications to CP operation- theory and experiment. *IEEE Trans. Antennas and Propagation*, vol. 38, no. 8, 1990.

[16] D. Colles and D. Arakaki. Multi-technique broadband microstrip patch antenna design. *IEEE Proc. Antennas and Propagation Society International Symposium*, 2014.

[17] M. Haneishi. A Broadband Microstrip Array Composed of single feed type circularly Polarized Microstrip Antennas. *IEEE Symposium Antenna and Propagation*, pp. (160-163), May 1982.

[18] Tomasic, B., Turtle, J., and Liu, S. A geodesic sphere phased array for satellite control and communication. *Int. Union of Radio Science, XXVIIth General Assembly*, Maastricht, The Netherlandss, August 2002.

[19] Niksa Burum and Zvonimir Sipus. Radiation Pattern of Spherical Array of Rectangular Microstrip Patches. In Proceedings IEEE Antennas and Propag., vol. 1, pp. 96-99, 2002.

[20] Zvonimir Sipus, Niksa Burum, and Juraj Bartolic. Moment method analysis of rectangular microstrip antennas on spherical structures. Proc. *IEEE Int. Symp. Soc. Antennas Propag.*, vol 3A, pp. 126-129, 2005.

[21] Z. Sipus, N. Burum, S. Skokic and P.-S. Kildal. Analysis of spherical arrays of microstrip antennas using moment method in spectral domain. *Proc. Inst. Elect. Eng. Microw. Antennas Propag*., vol. 153, pp. 533-543, 2006.

[22] K.-Y. Wu and J. F. Kauffman. Radiation pattern computations for cylindrical-rectangular microstrip antennas. In *Proc. Antennas Propag. Society Int. Symp.*, Houston, TX, USA, vol. 21, pp. 39–42, 1983.

[23] K.-Y. Wu and J. F. Kauffman. Radiation pattern computations for spherical-rectangular microstrip antennas. In *Proc. Antennas Propag. Society Int. Symp.*, Houston, TX, USA, vol. 21, pp. 43–46, 1983.

[24] C. M. Krowne. Cylindrical-rectangular microstrip antenna. *IEEE Trans. Antennas Propagat.*, vol. AP-31, pp. 194-199, 1983.

[25] A. K. Verma Nasimuddin. Multilayer cavity model for microstrip rectangular and circular patch antenna. *Electromagnetics Journal*, vol. 24, no. 3, 2004.

[26] S. Chai, D. Yao, and N. Yuan. Analysis of conical microstrip antennas with uniform substrate. *Aerospace and Electronics Conference, Proceedings of the IEEE 1996 National*, vol. 1, 20-23 May, pp. 259-263, 1996.

[27] V. Rahayu, K. Yokokawa, and Q. Chen. DOA Estimation of Linear Patch Antenna Array Using USV - MUSIC Algorithm. *IEEE Proc. Asia-Pacific Microwave Conference,* 2014.

[28] N. Hescovici and M. Champion. Considerations in the design of parallel plate luneburg beamformers and cylindrical arrays. *IEEE Trans. Antennas anda Propagat.*, 2016.

[29] C.A. Balanis. Antenna Theory: Analysis and Design. 2nd edition, J. Wiley, 1997.

[30] Balanis, C.A. *Advanced Engineering Electromagnetics*. John Wiley & Sons, New York, 1989.

[31] Hammerstad, E.O. Equations for Microstrip Circuit Design. *Proc. Fifth European Microwave Conf.*, pp. 268-272, September 1975.

[32] Kumar, G. and Ray, K.P. *Broadband Microstrip Antennas*. Artech House, Inc, 2003.

[33] James, J.R. and Hall, P.S. *Handbook of Microstrip Antennas*. Vols 1 and 2, Peter Peregrinus, London, UK, 1989.

[34] Bahl, I.J. and Bhartia, P. *Microstrip Antennas, Artech House.* Dedham, MA, 1980.

[35] Newmanm E.H. and Tylyathan, P. Analysis of Microstrip Antennas Using Moment Methods. *IEEE Trans. Antennas Propag*., vol. AP-29, No. 1, pp. 47- 53, January 1981.

[36] Harrington. R.F. *Field Computation by Moment Methods*. Macmillan, New York, 1968.

[37] Kantorovich, L. and Akilov, *G. Functional Analysis in Normed Spaces*. Pergamon, Oxford, pp. 586-587, 1964.

[38] Richards, W.F. *Microstrip Antennas, Chapter 10 in Antenna Handbook: Theory Applications and Design (Y.T. Lo and S.W. Lee, eds.).* Van Nostrand Reinhold Co., New York, 1988.

[39] Stutzman, W.L. and Thiele, G.A. *Antenna Theory and Design*. John Wiley & Sons, Inc, 1998.

[40] J.R. James, Peter S. Hall, and C. Wood. *Microstrip Antenna: Theory and Design*, 1981.

[41] Wai-Yip Tam and Kwai-Man Luk. Resonance in spherical-circular microstrip structures. *IEEE Trans. Microw. Theory Tech.*, 39:700–704, 1991.

[42] W.Y. Tam, A.K.Y. Lai, and K.M. Luk. Input impedance of spherical microstrip antenna. In *Microwaves, Antennas and Propagation, IEE Proceedings*, volume 142, pages 285–288. IET, 1995.

[43] W.-Y. Tam and K.-M. Luk. Far field analysis of spherical-circular microstrip antennas by electric surface current models. *IEE Proceedings-H*, 138:98–102, 1991.

[44] K.-M. Luk and W.-Y. Tam. Patch antennas on a spherical body. *Proc. Inst. Elect. Eng.*, 138:103–108, 1991.

[45] S.A. Schelkunoff. *Electromagnetic Waves*. NJ, Van Nostrand, 1943.

[46] Niksa Burum, Slavko Rupcic, and Zvonimir Sipus. Theoretical and experimental study of spherical arrays. *Proc. IEEE Mediterranean, Melecon 2004*, vol. 2, pp. 503-506, 2004.

[47] T. V. B. Giang, M. Thiel, and A. Dreher. Dyadic Green's function of multilayer spherical sector structures. In *Proc. 3rd Eur. Conformal Antennas Workshop*, Bonn, Germany, pp. 65–68, 2003.

[48] Truong Vu Bang Giang, Michael Thiel, and Achim Dreher. A unified approach to the analysis of radial waveguides, dielectric resonators, and microstrip antennas on spherical multilayer structures. *Microwave Theory and Techniques, IEEE Transactions on*, 53(1):404–409, 2005.

[49] R.F. Harrington. *Time-Harmonic Electromagnetic Fields*. IEEE Press, 2001.

[50] Salam K. Khamas. Moment method analysis of an archimedean spiral printed on a layered dielectric sphere. *IEEE Trans. Antennas and Propagation*, vol. 56, no. 2, 2008.

[51] David L. Rolando, and Gregory H. Huff. A geometrically-appropriate cavity model for a spherical inverted-F antenna (SIFA). *IEEE Trans. Antennas and Propagation*, vol. 61, pp. 2404-2410, 1981.

[52] Constantine A. Balanis. *Advanced Engineering Electromagnetics*. Wiley, 1989.

[53] L. A. Costa, O. M. C. Pereira-Filho, and F. J. S. Moreira. Analysis of spherical-rectangular microstrip antennas. *Proc. SBMO/IEEE MTT-S Int. Conf. Microw. And Optoelectronics*, pp. 279-282, 2005.

[54] Abramowitz and M. and Stegun I.A. *Handbook of Mathematical Functions*. Dover,New York, 1965.

[55] William F. Richards, Yuen T. Lo, and Danel D. Harrison. An improved theory for microstrip antennas and applications. *IEEE Trans. Antennas and Propagation*, vol. 29, no. 1, 1981.

[56] Z. Sipus, P. Kildal, R. Leijon, and M. Johansson. An algorithm for calculating green's functions of planar, circular, cylindrical and spherical multilayer substrates. In *14th International Conference on Applied Electromagnetics and Communications (ICECOM) 1997*, 1997.

[57] Leonardo A. Costa, Odilon M. C. Pereira-Filho, and Fernando J. S.Moreira. Input impedance of rectangular microstrip antennas on spherical bodies using MoM and attachment modes. *IEEE AP-S 2006 Digest*, pp. 3947-50, 2006.

[58] C. J. Taylor, D. J. Kriegman, "Minimization on the Lie Group SO(3) and Related Manifolds," *Technical Report*, No: 9405, Yale University, 1994